Charge Transfer Dynamics in Complexes of Light-Absorbing CdS Nanorods and Redox Catalysts

by

Molly Bea Wilker

B.A. Gustavus Adolphus College, 2009

A thesis submitted to the

Faculty of the Graduate School of the

University of Colorado in partial fulfillment

of the requirement for the degree of

Doctor of Philosophy

Department of Chemistry and Biochemistry

2015

This thesis entitled:

Charge Transfer Dynamics in Complexes of Light-Absorbing CdS Nanorods and Redox Catalysts

written by Molly B. Wilker

has been approved for the Program of Chemistry and Biochemistry

_____

Gordana Dukovic

_____

Niels Damrauer

Date_____

The final copy of this thesis has been examined by the signatories, and we find that both the content and the form meet acceptable presentation standards of scholarly work in the above mentioned discipline.

Wilker, Molly Bea (Ph.D., Chemistry and Biochemistry)

Charge Transfer Dynamics in Complexes of Light-Absorbing CdS Nanorods and Redox Catalysts

Thesis directed by Assistant Professor Gordana Dukovic

The use of photoexcited electrons and holes in semiconductor nanocrystals as reduction and oxidation reagents is an intriguing way of harvesting photon energy to drive chemical reactions. This dissertation describes research efforts to understand the photoexcited charge transfer kinetics in complexes of colloidal CdS nanorods coupled with either a water oxidation or reduction catalyst. The first project focuses on the charge transfer interactions between photoexcited CdS nanorods and a mononuclear water oxidation catalyst derived from the $[Ru(bpy)(tpy)Cl]^+$ parent structure. Upon excitation, hole transfer from CdS oxidizes the catalyst ($Ru^{2+} \rightarrow Ru^{3+}$) on a 100 ps – 1 ns timescale. This is followed by a 10 – 100 ns electron transfer that reduces the Ru^{3+} center. The relatively slow electron transfer dynamics may provide opportunities for accumulation of the multiple holes at the catalyst, which is necessary for water oxidation. The second project details the electron transfer kinetics in complexes of CdS nanorods coupled with [FeFe]-hydrogenase, which catalyzes H^+ reduction. These complexes photochemically produce H_2 with quantum yields of up to 20%. The kinetics of electron transfer from CdS nanorods to hydrogenase play a critical role in the overall photochemical reactivity, as the quantum efficiency of electron transfer defines the upper limit on the quantum yield of H_2 generation. For optimized complexes, the electron transfer rate constant and the electron

relaxation rate constant in CdS nanorods are comparable, with values of $\approx 10^7$ s^{-1}, resulting in a quantum efficiency of electron transfer of 42%. Insights from these time-resolved spectroscopic studies are used to discuss the intricate kinetic pathways involved in photochemical H_2 generation in photocatalytic complexes. Finally, experimental results from photodriven H_2 generation and measurements of nanocrystal excited state lifetimes when the length of the nanocrystal-surface ligand was varied provide a deeper understanding into the mechanism for electron transfer from photoexcited nanorods to hydrogenase.

Acknowledgements

The work in this dissertation would not have been possible without for the assistance and support of many people. I would like to acknowledge the funding sources that have supported this work: the Renewable and Sustainable Energy Institute (RASEI), the National Science Foundation CAREER grant (CHE-1151151), the U.S. Department of Energy Office of Basic Energy Sciences Division of Materials Sciences and Engineering grant (DE-SC0010334), and lab startup funds from the University of Colorado. I would like to thank the people at CU who contributed to and supported this work, especially my graduate advisor, Gordana Dukovic. In addition, a huge thanks to the present and former members of the Dukovic group including: Kyle Schnitzenbaumer, Amanda Grennell, Katherine Shinopoulos, Bryan Tienes, Kim See, Kyureon Lee, Hiroko Nakao, Tais Labrador, Hayden Hamby, James Utterback, Orion Pearce, Chi-Hung Chuang, and Yinggang Lu. And thanks to the undergraduate students who contributed to this work: Sophie Greene, David Garfield, and Russell Perkins. I would also like to thank my collaborators who were instrumental in making this work possible including, from NREL: Paul King, Kate Brown, David Mulder, and Mike Ratzloff, and from CU: Huan-Wei Tseng, Niels Damrauer, Jennifer Ellis, Dan Hickstein, Wei Xiong, Margaret Murnane, Henry Kapteyn, and Joel Eaves.

In my personal life, my thanks go to my family and friends for their love and support that has helped me to get to this place in my life. A special thank you to my parents, Scott and Gloria, my grandmother, Phyllis, and my brother, Sam for always believing in me and encouraging me to strive for greatness. My thanks go to my husband, Brett, for his patience and support. I would

also like to thank my friends who have been incredible confidants over the years, especially Liz, Rebecca, Jen, Kyle, Jamie, Katherine, Carly, Amanda, and Katie. Beyond my family and friends, I would also like to thank those who have helped guide my education and upbringing as a scientist. Thank you to my undergraduate research mentors: Jonathan Smith (Gustavus), Andreas Stein (U of MN), Jeffrey Hartgerink (Rice U), and Steven Miller (Gustavus).

Contents

Tables

Figures

Copyright

Chapter 1 Introduction

1.1 Motivation

1.1.1 Solar Energy Harvesting

Due to rapid growth in global energy consumption, humanity is faced with the challenge to secure sustainable energy sources to meet the demand. Currently, a majority of the energy consumed is from non-renewable, fossil energy sources. Of the various renewable energy sources currently accessible on earth, the sun is the most powerful energy resource. More energy from sunlight strikes the earth in one hour than all the energy consumed on the planet in one year.[1] The scientific community is interested in figuring out how to efficiently harness and use solar energy. Research in photovoltaic devices has made significant advances for efficiently converting solar energy to electricity. While photovoltaic solar cells convert sunlight to electricity under ideal sunlight conditions, these devices do not have the capacity to store electricity; therefore, they cannot provide a constant source of electricity.

An attractive approach for utilizing solar energy is to harvest solar photons to drive chemical reactions that produce fuels.[1] Sunlight can be used as the energy source to convert energy-poor molecules to energy-rich molecules. The chemical energy stored in fuels can be converted to mechanical or electrical power at a later time. In nature, this process occurs during photosynthesis. Using nature as a model for this process, we can build artificial photosynthetic

devices targeting the generation of low-carbon fuels. In particular, water splitting ($H_2O + 2h\nu \rightarrow H_2 + \frac{1}{2}O_2$) remains one of the most desirable ways to store energy by forming energy-dense H_2. A system for solar energy to H_2 fuel conversion has high potential impact on our overall renewable energy portfolio; however, significant advances are needed for this technology to attain this potential. To address this need, we create model systems to study the excited state processes, such as charge separation and charge transfer, which are necessary for photochemical fuel production.

1.2 Background

Processes of particular interest for generating solar fuels use photoexcited electrons and holes to reduce and oxidize, respectively, chemical species. These reactions follow a general scheme that involves absorption of visible photons to produce photoexcited electrons and holes, charge separation, followed by transfer of electrons and holes to co-catalysts where they are utilized. In recent years, there has been growth in research exploring nanocrystal photochemistry.[2] Several important studies have used colloidal CdS nanocrystals as components in fuel-generating photocatalytic systems, particularly for H^+ reduction.[3-14]

1.2.1 Semiconductor Nanocrystals as Photosensitizers

A suitable material for solar energy harvesting should absorb strongly in the visible part of the solar spectrum, have the correct energy level alignment to extract photoexcited electrons, and, in order to maximize energy output, should not lose energy through wasteful processes.[15] Nanoscale semiconductors (nanocrystals), specifically CdS nanorods (NRs), are model materials

for studying light to energy conversion because they exhibit many of these advantageous properties. Several characteristics of colloidal CdS nanocrystals make them particularly interesting photocatalysts. Chalcogenide nanocrystals absorb strongly in the visible region with molar absorptivities ~10^5 – 10^7 $M^{-1}cm^{-1}$, so they are able to harvest a significantly higher portion of the solar spectrum than the UV-absorbing oxides.[16,17] CdS NRs have an especially high molar absorptivity (~10^7 $M^{-1}cm^{-1}$) constant.[12]

When the size of the particle is below the exciton Bohr radius of the bulk semiconductor, the material's optical properties change dramatically. This quantum confinement of the exciton states enables the absorption properties to be synthetically tuned.[18] The band edge positions, redox potentials, and absorption spectra are, therefore, determined by nanocrystal composition, size, and shape, which are readily tunable. By synthesizing novel multi-component nanostructures, it is also possible to control the electronic structure within individual particles.[19] The CdS band edge positions, even without quantum confinement effects, have sufficient potentials to drive both the reduction of H^+ and the oxidation of H_2O.[20]

At the size scale of several nanometers, the small volume and large surface area characteristic of nanocrystals increases the probability of extracting photoexcited charge carriers to the surfaces where they can be utilized, rather than waiting for them to diffuse to the surface slowly in bulk materials. Surface properties are therefore important and significant work has been done to understand chemistry at the semiconductor nanocrystal surfaces.[21] Nanocrystals are synthesized with surface ligands to prevent particle aggregation and promote particle solubility. Nanocrystal surfaces can be capped with a variety of ligands, enabling either aqueous or organic solubility and providing selectivity of functional groups for interaction with molecular species in

solution.[22] Synthetic control of the highly tunable optical, size, and surface properties of semiconductor nanocrystals make them suitable for the light-harvesting components in novel nanocrystal-based photocatalytic systems that generate fuels. The photosensitizing material of focus for the systems discussed in this dissertation is nanocrystalline CdS.

1.2.2 Nanocrystal-Catalyst Heterostructures

To create a heterostructure for photodriven chemical reactions, catalysts are placed on light-absorbing semiconductor nanocrystals, as represented in the scheme in Figure 1.1a. Catalysts are required to overcome the complicated kinetics associated with the multielectron redox reactions. Some examples of the H^+ reduction catalysts employed for nanocrystal-based photocatalytic systems include Pt[5,23-29] and Pd nanoparticles[8], inorganic Ni[13,30-32], Co[33-36], and Mo[10] co-catalysts, and biological[6,9,12,37-41] and bio-inspired[7,14] catalysts. Nanocrystal-catalyst interactions that facilitate efficient charge transfer are critical for the kinetics of the overall photochemical process. Two metrics that are commonly used to quantify the capability of a catalytic system are turnover frequency (TOF) and turnover number (TON). The first denotes the rate of product formation and is indicative of catalytic efficiency upon delivery of electrons to the catalyst. The second quantifies how many turnovers the catalyst achieves before ceasing activity.

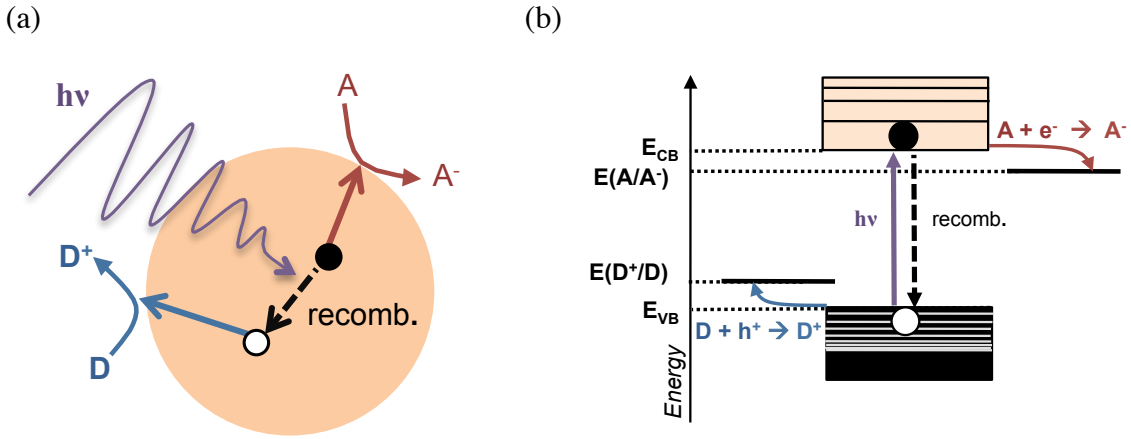

Figure 1.1 (a) Schematic representation of a photocatalytic reaction mediated by a semiconductor nanocrystal. Photoexcited electrons migrate to the surface and reduce an electron acceptor (A), while the holes oxidize an electron donor (D). This process is in competition with electron-hole recombination pathways. (b) Energy level diagram for a photocatalytic reaction indicating energetic requirements for valence and conduction band edges (E_{VB} and E_{CB}) with respect to reduction potentials of the donor and acceptor ($E(D^+/D)$ and $E(A/A^-)$). Adapted with permission from *Isr. J. Chem.*, 2012, **52**, 1002-1015. © Copyright 2012 Wiley-VCH.

1.2.3 Photoexcited Charge Carrier Dynamics

To efficiently extract the photoexcited charges from a photosensitizing material to a catalyst on the surface, the charge transfer processes must be kinetically competitive with intrinsic photoexcited electron-hole recombination processes. The efficiency of the crucial charge transfer processes is also dependent upon favorable thermodynamics (i.e., sufficient driving force for reduction and oxidation) (Figure 1.1b). The quantum yield (QY) of the photocatalytic product is emphasized in order to compare different catalytic systems. This quantity describes the ability of a given system to utilize absorbed photons for photocatalysis. It illustrates the competitiveness of excited state processes that lead to fuel generation with the electron-hole recombination pathways. In order to optimize the design of heterostructures for efficient H_2 generation, it is also important to understand the mechanisms of charge separation

and recombination. Therefore, ultrafast measurements of excited state kinetics are crucial for understanding the capabilities of heterostructures for photochemistry.

To directly observe the excited state electron dynamics of CdS nanocrystals, we use femtosecond pump/probe or transient absorption (TA) spectroscopy. TA spectroscopy employs a single-wavelength pump pulse, which creates an excited state. A low intensity, white-light probe is then sent through the sample at a specific delay time with respect to the pump pulse, which results in a difference absorption spectrum (ΔA). By changing the delay time, a ΔA profile as a function of wavelength and delay time is obtained. This TA spectroscopic data contains information about the dynamic process of the excited state. TA spectroscopy of CdS nanocrystals in this dissertation employs a 400 nm excitation, which creates an exciton (electron-hole pair) with higher energy than the band gap in a fraction of the population of nanocrystals. The photoexcited carriers quickly relax to the band edges (the electron to the bottom of the CB and the hole to the top of the VB) through radiationless transitions.[42] By probing the wavelength associated with the band gap transition of CdS, the population of excited state electrons is measured as a function of time delay.[43]

1.2.4 Biomimetic Nanocrystal-Catalyst Assemblies

Photosynthesis, nature's process for storing solar energy inside chemical bonds, provides an inspiration and some design principles for solar fuel generation.[44-47] In photosynthesis, light absorption and catalysis are performed by light-harvesting proteins and enzymes, respectively, and the two processes are coupled via a finely tuned series of electron transfer steps. While energy conversion efficiencies of natural photosynthesis are relatively low,[44] coupling excellent light-absorbers, such as nanocrystals, to fast enzymatic catalysts that can utilize carriers derived

from photoexciation may teach us how to design more efficient systems. Hydrogenases are metalloenzymes that catalyze the reduction of $2H^+$ to H_2 at high rates, requiring minimum driving force, and with high selectivity.[45,48-61] Hydrogenases have been utilized for hydrogen production by a range of approaches including *in vivo* and artificial hybrid systems.[45] In a number of studies, nanocrystals and hydrogenases or molecular mimics of hydrogenase active sites have been combined for photocatalytic fuel generation.[6,7,9,12,14,37-41,62]

CdTe nanocrystals were coupled to [FeFe]-hydrogenase from *Clostridium acetobutylicum* (CaI) in a bio-mimetic manner.[6,37] CaI is capable of operating at very high TOFs, up to 21,000 H_2 molecules per enzyme per second.[63] *In vivo*, electron delivery to CaI occurs via the redox-shuttle ferredoxin, which docks in a positively charged pocket on the enzyme (Figure 1.2).[64,65] A similar electrostatic interaction between CdTe and CaI was enabled by the use of the 3-mercaptopropionate (MPA) ligand, which attached to the nanocrystals via thiolate groups and presented negatively charged carboxylate groups to the enzyme(Figure 1.2). Upon illumination of these complexes with visible light, electron transfer from CdTe to CaI led to H_2 production, while the holes were scavenged by ascorbate in solution. The apparent QY of H_2 generation was 9% (λ=532nm) under optimized sample conditions.

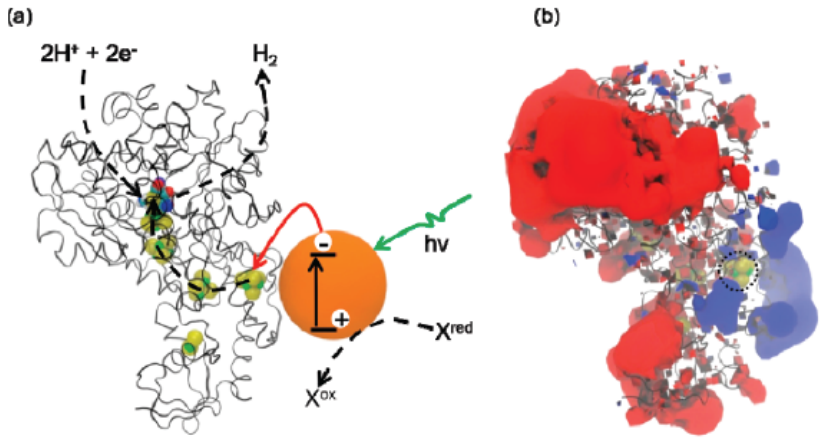

Figure 1.2 (a) The proposed scheme for light-driven H_2 production in a CdTe nanocrystal-hydrogenase hybrid structure. CdTe is shown as an orange sphere, X represents a hole scavenger, and the protein structure is CpI [FeFe]-hydrogenase (PDB entry 3C8Y). (b) Electrostatic surface model of hydrogenase with regions of positive and negative charge are shown in blue and red, respectively. It is proposed that CdTe nanocrystals, functionalized with a negatively charged surface, bind at the positive region of the hydrogenase (blue region). Adapted with permission from *J. Am. Chem. Soc.*, 2010, **132**, 9672-9680. © Copyright 2010 American Chemical Society.

With our collaborators at the National Renewable Energy Laboratory, we have contributed further mechanistic insights into the photochemical H_2 production by nanocrystal-CaI complexes from a study of CdS nanorod-CaI biohybrids.[12] The thermodynamics of self-assembly, and the resulting orientations were investigated using kinetic analysis of CdS binding to CaI in competition with ferredoxin, where CdS acted as an inhibitor of ferredoxin-driven H_2 production by CaI. The effect of CaI coverage in the context of CdS photon absorption and CaI catalytic flux were characterized. The effects of hole-transfer and light intensity were investigated, and it was found that the H_2 production was photon-limited under the experimental conditions (Figure 1.3a). The QY of the photocatalytic H_2 production was found to be ~20% (λ=405 nm) with TOF values of up to 380 (mol H_2)×(mol CaI)$^{-1}$× s^{-1}.[12] The long-term instability

observed for biohybrids under illumination (Figure 1.3b), which was first observed for MPA-CdTe:CaI complexes,[6] was attributed to deactivation of CaI by free ligand molecules that were photooxidatively removed from the CdS surface. These analyses demonstrate how the contributions of individual processes govern photocatalytic activity.

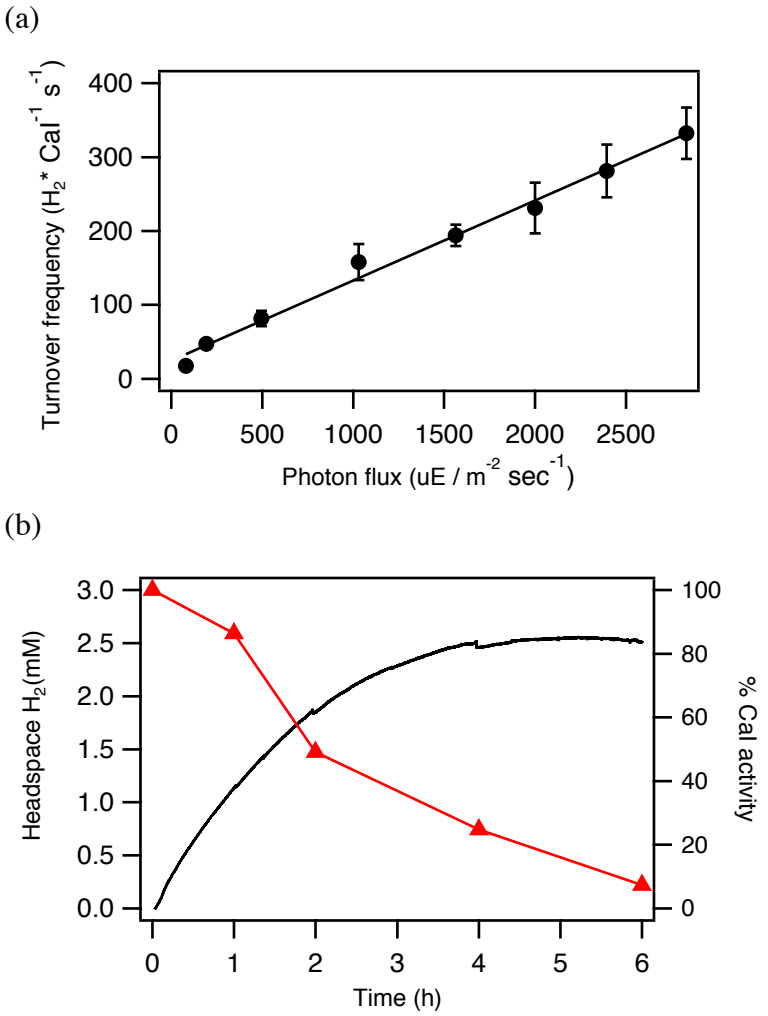

Figure 1.3 (a) H_2 generation rate, expressed as a TOF, has a linear dependence on 405 nm photon flux. (b) Total H_2 generated over time (solid line) and the corresponding relative CaI activity values (triangles). The data illustrates enzyme deactivation during H_2 production. Adapted with permission from *J. Am. Chem. Soc.*, 2012, **134**, 5627-5636. © Copyright 2012 American Chemical Society.

H_2 generation from CdS NR-CaI complexes involves the absorption of light by CdS NRs creating excitons, followed by injection of photoexcited electrons into CaI, where they are utilized for catalysis of $2H^+$ to H_2. The linear dependence of H_2 generation on light intensity indicates that the rate of the H_2 generation process is limited by electron flux (Figure 1.3). The upper limit for the electron injection rate is determined by the rate of photon absorption, but not every photogenerated electron is successfully transferred to the enzyme. Thus, it is crucial to examine the rates and efficiencies of the electron transfer process from CdS NRs to CaI upon the absorption of a photon. Our results demonstrating the biomimetic binding interaction of CaI to CdS NRs suggest that electron injection into CaI would also follow the biological pathway, with electron injection into the distal [4Fe4S] cluster.[66] To probe the pathway for electron transfer, we use catalytically inactive CaI. In Chapters 3 and 4, we describe ultrafast measurements of excited state kinetics to understand the dynamics of charge separation, recombination, and electron transfer in the CdS-CaI heterostructures.

Other studies of nanocrystal-hydrogenase complexes contribute to our understanding of this type of hybrid structure. In an interesting study by Dyer and co-workers, complexes of [NiFe]-hydrogenase from *Thiocapsa roseopersicina* (Tr) electrostatically coupled to MPA-capped CdTe quantum dots were shown to produce H_2 under visible light.[9] Maximum QY of H_2 production was 4% (λ=527nm) with a TON of 92. Some of the reduced efficiency and lower TON, when compared to nanocrystal-CaI systems, can be attributed to the catalytic bias of [NiFe]-hydrogenases in the direction of H_2 oxidation.[57,67] Insights into the utilization of photoexcited electrons by the enzyme were obtained from FTIR study of the catalytic states under H_2 production conditions. Accumulation of redox intermediates associated with slow

turnover was not observed, indicating that ET from CdTe to the enzyme active site is conducive to efficient catalysis. This suggests that the overall yield of H_2 is limited by the availability of electrons and the competitiveness of the ET process with recombination pathways.

1.2.5 Considerations for Photogenerated Holes

In the photocatalytic systems described above, after photoexcited electrons are transferred to the reduction catalyst, the photoexcited holes need to be transferred at an equivalent rate to hole-accepting molecules or oxidation catalysts to replenish the electrons used for reduction and to prevent nanocrystal degradation. Although the oxidation products are not fuels, the presence of an efficient oxidative species is imperative for the stability of photocatalytic H_2 producing systems. The choice in oxidative species can be a determining factor in the H_2 generation QY, TOF, and TON of a photocatalytic system.

Water oxidation is a four-electron oxidation process that is both mechanistically and thermodynamically demanding, which makes water oxidation significantly more difficult than water reduction (i.e. H_2 production). Metal oxide materials (ie: Ru, Pt, Ir, Co, Mn, W, Fe, and Ni oxides), manganese oxide clusters, and molecular complexes containing Ru, Mn, Co, and Ir have been established as viable water oxidation co-catalysts.[68-70] However, these materials have not successfully been coupled to II-VI semiconductor nanocrystals for photodriven water oxidation. Our work towards coupling a Ru-based molecular water oxidation catalyst to nanocrystals is detailed in Chapter 2. Due to the difficulty of water oxidation, the photocatalytic H_2 production heterosystems described above utilize a sacrificial hole scavenging species, rather than balancing the water reduction half reaction with water oxidation. Although there are many examples of molecules that will readily donate electrons to semiconductor nanocrystals including

isopropanol,[5] ascorbate,[6,12,13,37] sodium sulfide/sulfite,[8,24,25] triethanolamine,[10,35,71] hydroxyl anion/radical,[30] and even mercaptocarboxylate ligands,[4,72] the right choice in hole scavenger for a particular nanocrystal-catalyst hybrid system can determining its H_2 production capabilities. Ascorbate is the hole scavenger used for the photodriven H_2 production experiments detailed in Chapters 3 and 4.

1.3 Summary

Nanocrystals can mediate H_2 production under visible irradiation when coupled with inorganic or biological and bio-inspired co-catalysts. Reasonably high quantum yields of H_2 generation indicate that the processes that lead to H^+ reduction can be competitive with electron-hole recombination and other decay pathways. The overall photocatalytic rate is a delicate balance of the rates of excitation, charge transfer, recombination, electron utilization, back-electron transfer, and hole scavenging. Time-resolved spectroscopy may provide a means of deconvolving these various rates.

The primary goal of the research presented in this dissertation is to identify and optimize unique nanoscale phenomena useful for solar fuel generation. Understanding charge carrier processes in nanocrystals and hybrid nanocrystal-catalyst structures will make a considerable impact by lending insights into the fundamental processes of photocatalysis. Chapter 2 is based on a 2013 communication from the *Journal of the American Chemical Society* and describes the interaction between CdS nanorods with a Ru-based molecular water-oxidation catalyst.[73] Chapter 3 is based on an article from the *Journal of the American Chemical Society* from 2014 and

describes a CdS nanorod-hydrogenase heterostructure used for photochemical H_2 generation. This chapter outlines the details of the crucial electron transfer between the inorganic nanocrystalline photosensitizer and the enzymatic catalyst.[41] Chapter 4 builds on the work in Chapter 3 and focuses on the nanocrystal surface ligands and the role they play in electron transfer and ultimately, catalysis. By understanding the properties of these model systems, we hope to make contributions towards the design of efficient solar fuel-generating nano-heterostructures.

Chapter 2 Charge Transfer Dynamics between Photoexcited CdS Nanorods and Mononuclear Ruthenium Water-Oxidation Catalysts†

2.1 Introduction

Using solar photons to drive fuel-generating reactions, such as splitting water into H_2 and O_2, will allow for storage of solar energy necessary for on-demand availability.[1] Inspired by natural photosynthesis, our interest is in exploring artificial systems that feature light absorbers directly coupled to redox catalysts.[2] Colloidal semiconductor nanocrystals are attractive light harvesters because they have tunable absorption spectra and high molar absorptivities (10^5-10^7 $M^{-1}cm^{-1}$). Their coupling with H^+ reduction catalysts has been recently reviewed and was outlined in the Chapter 1.[2,74] The resulting hybrid structures are capable of light-driven H_2 generation with the use of sacrificial electron donors. Water oxidation, the other half reaction of water splitting, is a mechanistically complicated process involving the transfer of multiple electrons and protons and the formation of an O-O bond.[75] Over the last three decades, there has been significant progress in the discovery of ruthenium complexes that catalyze water

---

† Adapted from H. W. Tseng*, M. B. Wilker*, N. H. Damrauer and G. Dukovic, *Journal of the American Chemical Society*, 2013, **135**, 3383-3386. *Authors Contributed Equally (© Copyright 2013 American Chemical Society)

oxidation.[76-82] Consistent with the complexity of this reaction, the molecular catalysts operate at turnover frequencies (TOFs) that are considerably lower than TOFs for H^+ reduction.[2,76] For this reason, successful delivery of photoexcited holes to the catalyst is particularly critical. Understanding the competition between charge transfer and photophysical carrier deactivation pathways, such as electron-hole recombination, is of paramount importance for the design of nanocrystal-based water-splitting systems.

Herein, we describe the charge transfer dynamics between photoexcited CdS nanorods (NRs), shown in Figure 2.1a and a mononuclear water-oxidation catalyst [Ru(deeb)(tpy)Cl](PF_6) (deeb = diethyl 2,2'-bipyridine-4,4'-dicarboxylate, tpy = 2,2':6',2"-terpyridine) in methanol. We refer to the catalyst as complex **1** (Figure 2.1b). The interaction between the two species results in concentration-dependent quenching of CdS NR photoluminescence (PL) and has a marked impact on CdS excited state dynamics, as measured by transient absorption (TA) spectroscopy. We find that there are two distinct charge transfer steps in the hybrid nanocrystal-catalyst system: hole transfer (HT) followed by electron transfer (ET), both from the photoexcited CdS NR to complex **1,** with the overall result being electron-hole recombination at the metal center. The HT occurs on the timescale of 100 ps – 1 ns, while the subsequent ET occurs in 10-100 ns. The relatively slow rate of recombination exposes opportunities for diverting the photoexcited CdS electrons via auxiliary electron transfer processes.

(a) (b)

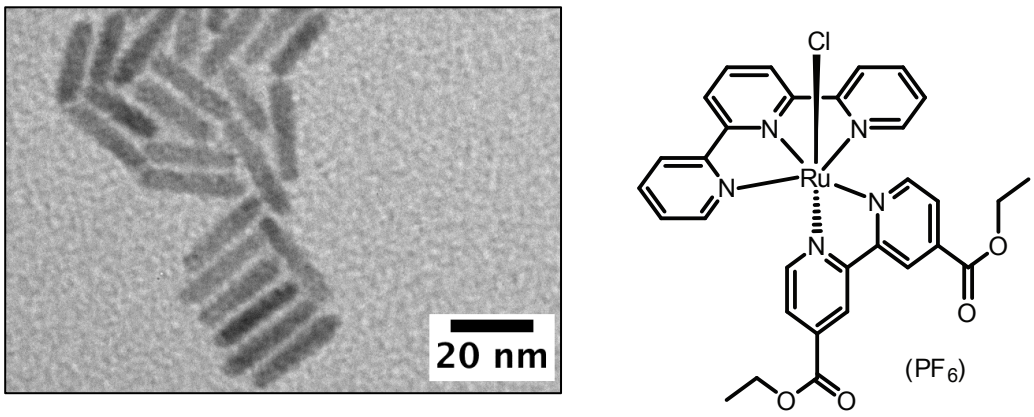

Figure 2.1 (a) TEM image of CdS NRs with 4.0 ± 0.4 nm widths and 13.7 ± 2.3 nm lengths. (b) Chemical structure of the water oxidation catalyst [Ru(deeb)(tpy)Cl](PF_6). Adapted with permission from *J. Am. Chem. Soc*., 2013, **135**, 3383-3386. © Copyright 2013 American Chemical Society.

2.2 Experimental

2.2.1 Synthesis of CdS Nanorods

The CdS nanorods were synthesized using a previously reported procedure.[12,83,84] Synthesis and processing were performed under an inert argon atmosphere at ~620 Torr. 8.54 mmol trioctylphosphine oxide (TOPO; Sigma Aldrich, *ReagentPlus*®, 99%), 3.2 mmol n-octadecylphosphonic acid (ODPA; PCI Synthesis), 1.61 mmol cadmium oxide (CdO; Sigma Aldrich, ≥99.99% trace metals basis) were stirred under vacuum at 120ºC and then heated under Ar to 320ºC for 1hr. The mixture was then cooled to 120ºC, stirred under vacuum for 1h, and then heated again under Ar to 320ºC. 5.40 mmol tri-n-octylphosphine (TOP; Strem Chemicals, min. 97%), and 3.2 mmol trioctylphosphine sulfide (TOP:S) were injected. TOP:S was prepared by mixing TOP and elemental S (Aldrich, 99.998%) in a 1:1 molar ratio in an argon glovebox and stirring at room temperature for 48 hours. After TOP:S injection, nanocrystal growth

proceeded at 315ºC for 45 minutes. The reaction mixture was then cooled to 80ºC, and the nanocrystals were precipitated using a toluene:acetone (1:2 volume ratio) mixture. The CdS nanocrystals were purified under Ar through sequential re-dispersion/precipitation steps using toluene/octylamine/acetone, chloroform/nonanoic acid/isopropanol, and hexane/isopropanol mixtures. Finally, sequential precipitation steps using increasing amounts of isopropanol were used to separate the mixture into fractions with narrower length distribution. The purified nanocrystals were re-dispersed and stored in toluene.

The resulting highly monodispersed nanorods used for all experiments presented in this chapter, with the exception of the longer rods used in section 2.3.7, had an average diameter of 4.0 ± 0.4 nm and an average length of 13.7 ± 2.3 nm, as determined by measurements of over 200 particles in TEM images. The molar absorptivity (ε) of the CdS nanorods was determined by correlating absorption spectra with Cd^{2+} concentrations determined by elemental analysis (ICP-OES) of acid-digested samples. The estimated value of $\varepsilon_{350\ nm}$ was 1710 $M^{-1}cm^{-1}$ per Cd^{2+}. The number of Cd^{2+} per nanorod was estimated from average nanorod dimensions. $\varepsilon_{350\ nm}$ for this batch of nanorods was 6 x 10^6 $M^{-1}cm^{-1}$.

The nanocrystals and catalysts were tailored to enable an interaction with sufficient physical proximity for charge transfer in a polar medium. The hydrophobic surface-capping ligands on the as-synthesized CdS NRs were replaced with 3-mercaptopropionate (3-MPA)[12] which binds to CdS via the thiolate group while the negatively charged carboxylate prevents flocculation in polar solvents.[85] The ligand exchange processes was done under an Ar atmosphere using the following procedure.[12] First, a 70 mM solution of 3-mercaptopropionic acid (3-MPA;Sigma Aldrich ≥99%) in methanol was prepared. The pH of the 3-MPA solution

was raised to pH 11 with tetramethylammonium hydroxide pentahydrate (Sigma ≥97%). Next, a sample of the original, organic-capped, nanocrystals in toluene was precipitated using methanol. The precipitated nanocrystals were then vigorously mixed with the 70 mM 3-MPA solution until no longer cloudy. A large amount of toluene was added to the solution to precipitate the 3-MPA-capped nanocrystals. The resulting particles were collected, dried under vacuum, and then re-dissolved in HPLC-grade MeOH.

2.2.2 Transmission Electron Microscopy (TEM)

TEM samples were prepared by drop casting from solution onto carbon film, 300 mesh, copper grids from Electron Microscopy Sciences. Images were obtained using a 100KV Phillips CM100 TEM equipped with a bottom-mounted 4 megapixal AMT v600 digital camera. Nanorod dimensions were obtained using *ImageJ* software to measure more than 200 nanocrystals.

2.2.3 Synthesis of Ru(II) Complexes

[Ru(dcb)(tpy)Cl]Cl and [Ru(deeb)(tpy)Cl](PF_6) (Complex **1)** were synthesized according to published procedures.[80,82] [Ru(dcb)(tpy)Cl]Cl was dissolved in H_2O and precipitated by adding $HPF_{6(aq)}$ to afford [Ru(dcb)(tpy)Cl](PF_6). ESI(+) MS and ^{1}H-NMR chemical shifts matched the published values.[80,82] ESI(+) MS and ^{1}H-NMR characterization of **1** in MeOH did not reveal evidence of Cl ligand displacement by the solvent.

2.2.4 Coupling of CdS NR to Complex 1

To form the CdS-**1** hybrid system, HPLC grade MeOH (Sigma-Aldrich) solutions of CdS NRs and **1** were mixed, and samples sealed under Ar. Absorption spectra were recorded in 1 cm path length quartz cuvettes at room temperature with an Agilent 8453 spectrophotometer

equipped with tungsten and deuterium lamps. The concentration of **1** in each solution was determined from the absorbance at 520 nm (ε = 16000 $M^{-1} cm^{-1}$ measured in MeOH) where there is no contribution from the NRs. The CdS NR concentration was determined from the absorbance at 350 nm following subtraction of the absorbance from **1**. For samples associated with Figure 2.11, methanol solutions of ascorbate (derived from ascorbic acid (Sigma-Aldrich BioXtra, ≥ 99.0%) using tetramethylammonium hydroxide pentahydrate (Sigma ≥ 97%) to raise the pH) or methylene blue (MB) hydrate (Aldrich) were added. The ascorbate solution was 1.6 x 10^{-4} M and was combined with the nanocrystals in a 1:1700 (CdS NR: ascorbate) ratio. The MB solution was 3.5 mM and was combined in a 1:200 (CdS NR:MB) ratio. We modified the $[Ru(bpy)(tpy)Cl]^+$ parent compound with two potential anchoring groups on the bpy: carboxylic acid moieties, based on an approach for attachment of Ru(II) tris-bipyridyl complexes to the surfaces of CdSe quantum dots in organic solvents,[86,87] and ester functionalities (to yield complex **1**), which have been reported to bind to TiO_2.[88]

2.2.5 Photoluminescence Spectroscopy

Photoluminescence spectra were obtained at room temperature using a Photon Technology International fluorometer with an Ushio UXL-75XE xenon short arc lamp and a PTI-814 Photomultiplier Detection System with a Hamamatsu R928P photomultiplier tube operating at −1000 V, DC. Samples in 1 cm x 1 cm quartz cuvettes were excited at 360 nm and the emission from 425 nm to 700 nm was recorded at 90° relative to the excitation. Emission spectra were corrected for wavelength dependence of the instrument response using a tungsten lamp provided by the manufacturer, which has been calibrated against a NIST tungsten lamp. CdS NR concentration was 0.18 μM.

2.2.6 Ultrafast Transient Absorption (TA) Spectroscopy

The ultrafast (100 fs to 3.3 ns) TA spectrometer used in this study uses an amplified Ti:sapphire laser (Solstice, Spectra-Physics, 800 nm, 1 kHz, 100 fs, 3.5 mJ/pulse), an optical parametric amplifier (TOPAS-C, Light Conversion), and the Helios spectrometer (Ultrafast Systems, LLC). A fraction (1.6 mJ/pulse) of the 800nm Solstice output was directed to the TOPAS-C to produce the desired pump wavelength (400 nm in the data described here) for sample excitation, which was then directed into the Helios. The pump pulse beam waist (~350 μm) and energy (<10 nJ/pulse) were chosen to maintain a nanocrystal excitation probability below 0.3 per laser pulse to avoid excitation of multiple electron-hole pairs within the nanocrystals. The pump pulses were passed through a depolarizer and chopped by a synchronized chopper to 500 Hz before reaching the sample. Another fraction of the 800 nm Solstice output (~0.1 mJ/pulse) was guided directly into the Helios for generation of the probe. Within the spectrometer, a white light continuum of wavelengths including 450 – 800 nm was generated using a sapphire plate. This beam was split into a probe and a reference beam. The probe beam was focused into the sample where it was overlapped with the pump beam. The transmitted probe and reference beams were then focused into optical fibers coupled to multichannel spectrometers with CMOS sensors with 1 kHz detection rates. The reference signal is used to correct the probe signal for pulse-to-pulse fluctuations in the white-light continuum. The time delay between the pump and probe pulses was controlled by a motorized delay stage. For all transient absorption measurements, the sample was sealed under Ar in a 2 mm quartz cuvette equipped with a Kontes valve and constantly stirred. CdS NR concentrations were approximately 0.8 μM. All experiments were conducted at room temperature. The change in

absorbance signal (ΔA) was calculated from the intensities of sequential probe pulses with and without the pump pulse excitation. The data collection (500 pump shots per time point) was carried out three consecutive times to ensure no photo-induced changes occurred. The three traces were then averaged.

2.2.7 Nanosecond-Microsecond Transient Absorption Spectroscopy

The 0.3 ns – 400 μs TA spectrometer used the amplified Ti:sapphire laser and optical parametric amplifier described above coupled with the Eos spectrometer (Ultrafast Systems, LLC). The pump beam (400 nm) was depolarized and the power was controlled with neutral density filters. The pump-probe time delay was controlled by a digital delay generator (CNT-90, Pendulum Instruments). The white light continuum (400 – 900 nm) for the probe and reference beams was generated by an external 2 kHz Nd:YAG laser focused into a photonic crystal fiber. The probe and reference signals were focused into the same detectors as used for the ultrafast TA system. Helios and Eos ΔA kinetic traces were combined using *Surface Xplorer Pro* by Ultrafast Systems, LLC

2.3 Results and Discussion

2.3.1 Design of the CdS NR-Complex 1 System

The main design criteria for our model nanocrystal-catalyst system involved: (i) use of materials with relatively well understood optical and catalytic properties, (ii) the possibility of forming electronically coupled heterostructures, and (iii) relative energy alignments that would permit hole transfer from the photoexcited nanocrystal to the catalyst. CdS, a direct-gap

semiconductor with a band gap of 2.4 eV, has valence and conduction band positions thermodynamically suitable for both water oxidation and reduction.[89] CdS-based nanostructures have been commonly employed in nanocrystal-catalyst hybrids for H^+ reduction.[2,74] In the selection of a water oxidation catalyst, we took advantage of recent findings demonstrating that the multiple redox steps required for water oxidation can be negotiated by mononuclear ruthenium complexes[76,79-82] Species based on the $[Ru(bpy)(tpy)Cl]^+$ (bpy = 2,2'-bipyridine) parent structure have the advantages of relatively straightforward synthesis and redox potential tunability via ligand functionalization.[80]

When the Ru-complexes were mixed with CdS NRs, the ester functionalities allowed for considerably stronger quenching of CdS PL than the acid groups. This suggests a repulsive interaction between deprotonated carboxylic acid groups on 4,4'- dicarboxy-2,2'-bipyridine and the anionic NR surface capped with 3-MPA. In contrast, complex **1**, with an overall positive charge, may be electrostatically attracted to the NR surface. We note that complex **1** is an active water oxidation catalyst with relatively high turnover numbers initiated by the sacrificial oxidant Ce^{4+} whose redox potential (1.7 V vs. NHE) is less positive than the valence band edge of CdS.[80]

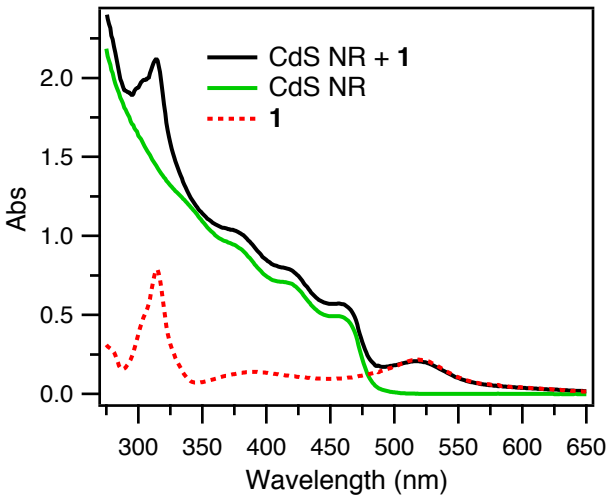

Figure 2.2 UV-Vis absorption spectra of the CdS NRs (1.8×10^{-7} M), complex **1** (1.3×10^{-5} M), and their mixture with a 1:72 NR:**1** molar ratio, all in methanol. Adapted with permission from *J. Am. Chem. Soc.*, 2013, **135**, 3383-3386. © Copyright 2013 American Chemical Society.

Figure 2.2 shows the UV-Vis absorption spectra of the CdS NRs, complex **1**, and their mixture, all in MeOH. The CdS NR spectrum has four distinct absorption bands, the lowest of which corresponds to the band gap transition at 470 nm (2.64 eV). Complex **1** exhibits a prominent feature that is conveniently located further to the red: a broad absorption band centered at 520 nm attributed to metal-to-ligand charge-transfer.[90] The absorption spectrum of a mixture containing CdS NRs and **1** is a superposition of the spectra of the constituents, indicating that upon mixing, **1** was not chemically modified and CdS NRs were not etched. The mixture was stable to precipitation for at least 24 hours. The excitation wavelengths we use for photophysical characterization (360 and 400 nm) primarily excite CdS, with only 4% of absorbed photons exciting **1**.

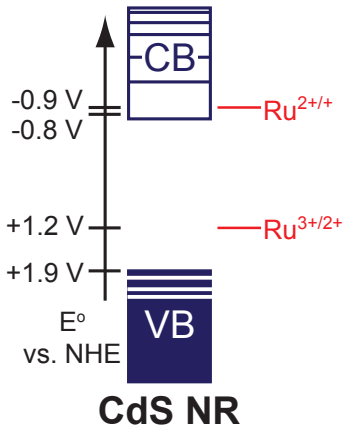

Figure 2.3 Energy level diagram depicting the band edges of CdS NRs and the redox potentials of complex **1**. Adapted with permission from *J. Am. Chem. Soc.*, 2013, **135**, 3383-3386. © Copyright 2013 American Chemical Society.

Figure 2.3 contains an energy level diagram for the CdS-**1** system. The band edges of CdS NRs, which are quantum confined in the radial direction, were approximated using the Brus equation.[18] The bulk band gap energy is 2.5 eV, and the valence band position with respect to vacuum is -6.26 eV.[20] The quantum confined band gap was determined from the steady state band edge absorption edge (2.64 eV), and the valence and conduction band edges were adjusted taking into account the effective masses of the electron (0.2 m_0) and the hole (0.7 m_0).[91] The vacuum scale was then converted to NHE (-4.4 eV (vacuum) ≈ 0 V NHE). The one-electron oxidation and reduction potentials of **1** in MeCN have been previously reported.[80,92] Although the system is studied in MeOH for this paper, no further modifications to the redox potentials are made because solvent-based redox potential changes have been observed to be small for a large and coordinatively-saturated complex such as **1**.[93] The first oxidation potential ($Ru^{3+/2+}$) of **1** is 0.7 V less positive than the NR VB edge, which should then permit hole-transfer to **1** following photoexcitation of the NR. Conversely, the CB edge of the NR is 0.2 V more positive than the

2+/1+ couple of **1,** which should hinder photoinduced electron transfer from the NR to the LUMO of the catalyst. The $Ru^{3+/2+}$ potential is associated with oxidation at the Ru metal center, while the $Ru^{2+/+}$ is associated with ligand reduction.[94] Based on the energy level alignment, we expect hole transfer from photoexcited CdS NRs to the Ru center to be thermodynamically favorable.

The effect of interaction between CdS NRs and **1** on CdS PL is shown in Figure 2.4. CdS NRs exhibit two distinct PL features: band-gap emission (λ_{max} = 475 nm) and trap emission, seen as a broad red-shifted feature.[83,95] The combination of low quantum yield of exciton emission (<1%) and very long excited electron lifetimes (>100 ns, described below) is an indication of efficient hole trapping.[83,95] Thus we assign the low-energy trap emission primarily to recombination of a surface-trapped hole with an electron in the lowest CB level. Immediately upon mixing with **1**, both the band-gap and trap emission were quenched, with the degree of quenching dependent on the CdS NR:**1** ratio (Figure 2.4). PL spectra of the mixture remained unchanged for at least 24 hours. Complex **1** is non-emissive and it remains silent in the PL spectra. In control experiments, PL quenching did not occur upon addition of free tpy or deeb ligands to CdS NRs (Figure 2.5), suggesting the importance of the Ru center in the quenching process.

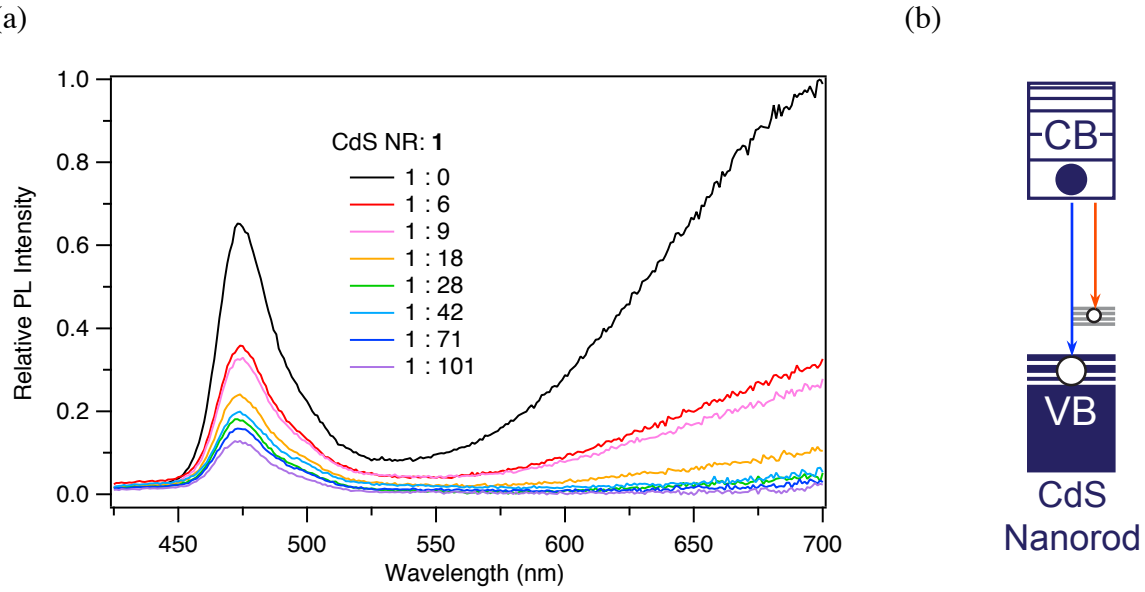

Figure 2.4 (a) PL spectra of CdS NRs with increasing amounts of **1** and constant [NR] (λ_{ex}=360 nm). (b) Energy level diagram schematic of the two processes corresponding to the peaks in the PL spectra. The blue arrow corresponds to band gap emission (PL peak at 475 nm) and the red arrow corresponds to trap emission (PL peak at 700 nm). Adapted with permission from *J. Am. Chem. Soc.*, 2013, **135**, 3383-3386. © Copyright 2013 American Chemical Society.

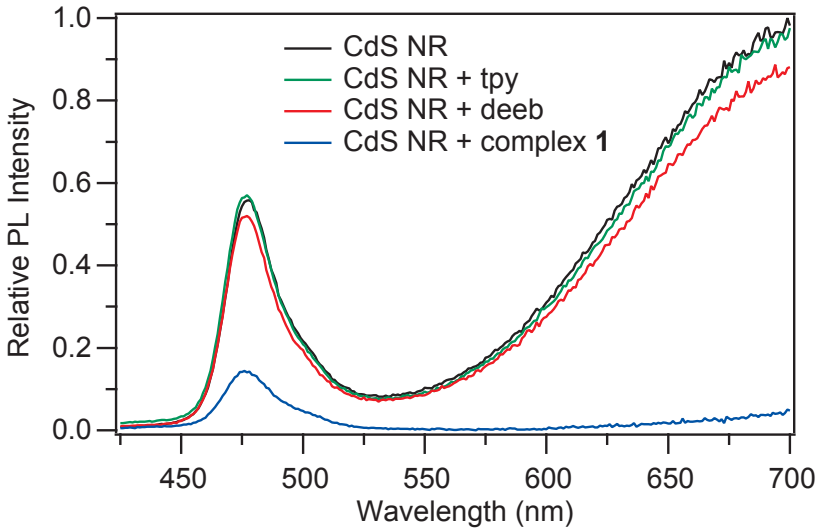

Figure 2.5 PL spectra recorded in MeOH for CdS NR (black trace) and CdS NR with free ligands of tpy (green trace), deeb (red trace), or with complex 1 (blue trace). The ratios of CdS NR to quenchers are all 1:50. The PL of CdS NR is significantly quenched by **1**, but not by tpy or deeb. Adapted with permission from *J. Am. Chem. Soc.*, 2013, **135**, 3383-3386. © Copyright 2013 American Chemical Society.

2.3.2 Analysis of the PL quenching mechanism

To elucidate the interaction between the CdS NRs and complex **1**, we analyzed the quenching of CdS NR PL by **1** (Figure 2.4). Figure 2.6 illustrates the degree of CdS PL quenching for both the band-gap and trap emission as a function of **1**:CdS NR ratio. We considered two models for the interaction of CdS NRs and **1**: collisional dynamic quenching, which can be described with a Stern-Volmer expression, and static quenching due to adsorbed molecules, for which a Langmuir adsorption isotherm is suitable.[87,96] For pure collisional quenching in a homogeneous solution, a plot of I_0/I_Q vs [Q] should follow the linear form of the Stern-Volmer equation:

$$\frac{I_0}{I_Q} = 1 + K_{SV}[Q] \qquad \text{(Equation 2.1)}$$

where I_0 is the PL intensity of CdS NR without quencher, I_Q is the PL intensity of CdS NR with quencher, K_{SV} is the Stern-Volmer constant, and [Q] is the concentration of quencher. The band gap and trap emission quenching (I_0/I_Q) vs [Q] are shown in Figure 2.7a and b. The data for the band gap transition are clearly a poor fit to Eq. 2.1. The quenching of the trap emission fits the Stern-Volmer model better. However, we note that the trap emission was significantly weaker than band gap emission at increased **1**:CdS NR ratios (Figure 2.4a) and thus there is higher uncertainty in the data in Figure 2.7b. Furthermore, because trap states are longer lived than band gap states, they may be more susceptible to collisional quenching. Overall, given the poor fit of the quenching of the band gap transition to the Stern-Volmer model, we conclude that collisions alone cannot account for the concentration-dependent quenching of CdS PL.

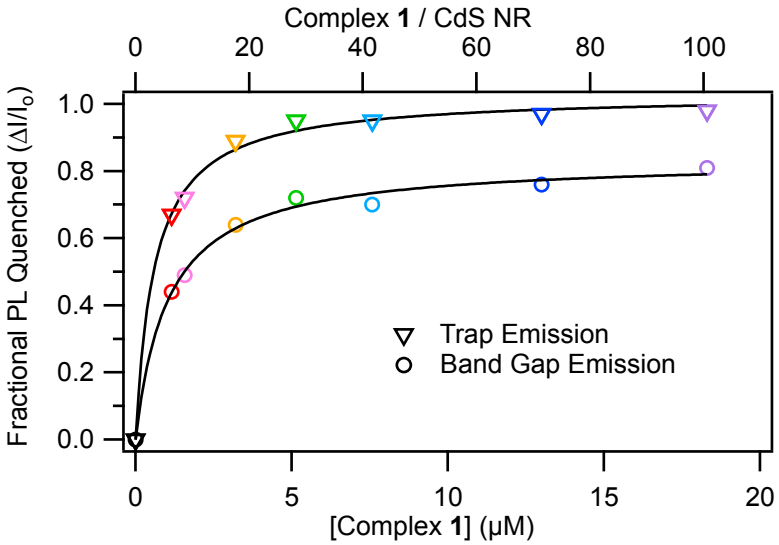

Figure 2.6 Fraction of PL quenched for band-gap (475 nm, circles) and trap (700 nm, triangles) emission as a function of [**1**] (bottom axis) and the 1:CdS ratio (top axis). The lines represent fits to a Langmuir adsorption isotherm, suggesting binding between CdS NRs and **1**. Adapted with permission from *J. Am. Chem. Soc.*, 2013, **135**, 3383-3386. © Copyright 2013 American Chemical Society.

Next, we consider the Langmuir adsorption model for the CdS-**1** interaction. Assuming quenching is caused by adsorption of molecules, we can write the Langmuir adsorption isotherm as:

$$\theta = \frac{K \cdot [Q]}{1 + K \cdot [Q]}$$

(Equation 2.2)

where Q is quencher (the adsorbate), θ is the fraction of surface sites occupied by the quencher, and K is the equilibrium constant for adsorption of **1** on CdS surface. We assume that θ is equal to the fraction of PL quenched ($\Delta I/I_0$). Here, I_0 is the PL intensity of CdS NR with no quencher present, while ΔI ($=I_0-I_Q$) is the amount of PL quenched in the presence of quencher. An additional complication is that, unlike trap emission, band gap emission was not fully quenched

at saturation. We attribute this to a lower quenching efficiency for the band-gap emission caused by its shorter lifetime compared to the trap emission.[97] To account for the incomplete quenching, we introduce the term, $(\Delta I/I_0)_{max}$, which is the maximum fractional quenching observed.[96] Eq. 2.2 then becomes:

$$\frac{\Delta I}{I_0} = \frac{(\Delta I/I_0)_{max} \cdot K \cdot [Q]}{1 + K \cdot [Q]} \quad \text{(Equation 2.3)}$$

For a more direct comparison with the Stern-Volmer model, Eq. 2.3 can be rearranged to give the linear form:

$$\frac{I_0}{\Delta I} = \frac{1}{(\Delta I/I_0)_{max}} \cdot \frac{1}{K[Q]} + \frac{1}{(\Delta I/I_0)_{max}} \quad \text{(Equation 2.4)}$$

As shown in Figure 2.7c and d, the dependence of CdS PL quenching on concentration of **1** fit with Eq. 2.4 (the Langmuir model) is superior, indicating that the quenching behavior is driven at least partially by adsorption. For the band gap transition, we find that $K = 9.5 \times 10^5\ M^{-1}$ and $(\Delta I/I_0)_{max} = 0.83$, whereas for the trap emission the parameters are $K = 1.6 \times 10^6\ M^{-1}$ and $(\Delta I/I_0)_{max} = 1.0$. Like the difference in the values of $(\Delta I/I_0)_{max}$ mentioned above, the difference in the values of K may be attributable to different quenching efficiencies for the two transitions. Given the same number of bound quenchers, more of the trap emission would be quenched, compared to band gap emission, resulting in a higher apparent value of K. Another way to state this is that K is actually a combination of an equilibrium constant and a quenching efficiency. Consequently, the maximum fractional quenching is 1.0 for the former and 0.83 for the latter (Figure 2.6).

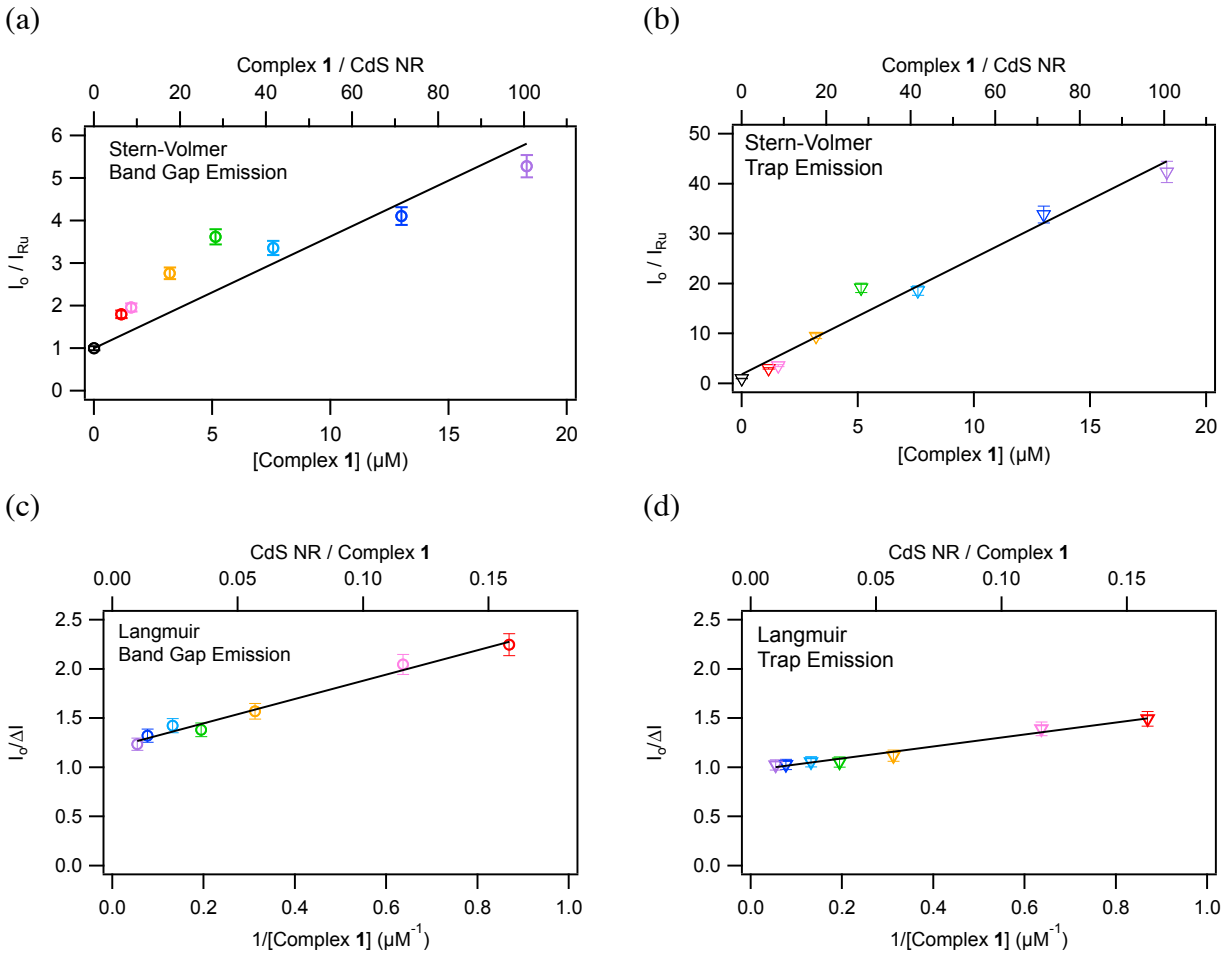

Figure 2.7 Quenching of CdS PL emission as a function of concentration of **1**. In (a) and (b), band gap and trap emission are fit with the Stern-Volmer model for dynamic collisional quenching, whereas in (c) and (d) the same data is fit with a linear form of the Langmuir adsorption isotherm. Error bars were determined by comparing three PL spectra taken over a period of 1 hour for one sample with a CdS:**1** ratio of 1:43 and one CdS-only sample. The error was then propagated in an additive fashion to obtain the total value of ± 5%. This method overestimates the uncertainty in the measurement. Adapted with permission from *J. Am. Chem. Soc.*, 2013, **135**, 3383-3386. © Copyright 2013 American Chemical Society.

2.3.3 Transient Absorption Spectroscopy of CdS NR-Complex 1 system

One explanation for the quenching of CdS PL in the presence of **1** is charge transfer. However, since PL intensity depends on the product of electron and hole populations, quenching

does not indicate which of the carriers is involved.[43,86] To ascertain the nature of the charge transfer interaction and elucidate the dynamics of this process, we turn to TA spectroscopy over a 100 fs - 1 μs timescale range. TA spectra of CdS NRs (Figure 2.8a) acquired after 400 nm excitation exhibit a prominent bleach feature (~ 470 nm) that corresponds to state-filling of the band gap transition. In addition, a rapidly decaying absorption feature is observed at 482 nm, red-shifted from the exciton bleach feature. This has been attributed to the bi-exciton shift due to hot excitons, and its decay corresponds to carrier cooling.[43] A second absorption feature at higher-energy (~440 nm) corresponds to higher energy exciton bands.[43,95] The presence of **1** does not change the position or shape of the CdS spectral features nor are there additional features in the TA associated with **1** (Figure 2.8b). Because the molar absorptivity of **1** is two orders of magnitude smaller than that of CdS NRs, **1** does not contribute a detectable signal to the TA spectra (Figure 2.8b/c). We used low pump pulse energies to avoid excitation of multiple electron-hole pairs per NR. The intensity of the 470 nm bleach feature is proportional to the population of excited electrons in the lowest-lying CB level of CdS NRs.[43] This feature is insensitive to the hole population because of the higher density of energy levels near the VB edge.[43] Thus, single-wavelength kinetics at 470 nm can be used as a signature for electron dynamics.

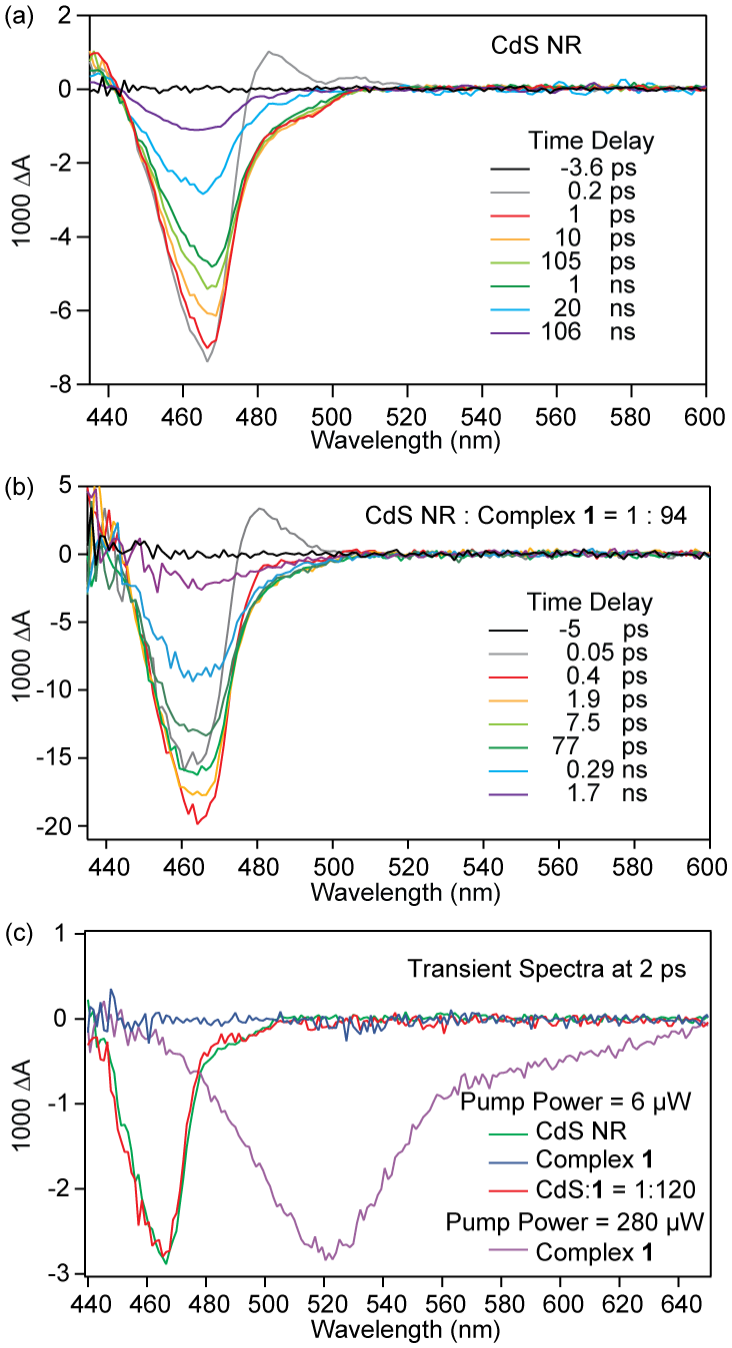

Figure 2.8 Transient absorption spectra of (a) CdS NRs in MeOH and (b) CdS with **1** in a 1 : 94 ratio at different time delays following 400 nm excitation. (c) Transient absorption spectra of CdS NRs, CdS + **1** (1:120 molar mixture), and **1** taken 2 ps after excitation with a 400 nm pump. Under the normal conditions for the TA experiments (pump pulse energy 6 nJ), there is no transient signal observed from **1**. When the pulse energy is increased 47-fold to 280 nJ, a sample containing **1** only exhibits a bleach ~520 nm. Adapted with permission from *J. Am. Chem. Soc.*, 2013, **135**, 3383-3386.

The kinetics of the CdS NR band gap bleach in the presence and absence of **1** are shown in Figure 2.9. To facilitate the visualization of the dynamics over 7 orders of magnitude in time, in Figure 2.9a, we use a linear time axis up to 10 ps, and a logarithmic scale thereafter. Plots using a linear time axis are shown in Figure 2.9b. Following 400 nm excitation, rapid (~ 1 ps) electron cooling to the CB edge is observed as a rise of the bleach signal. The subsequent band-gap bleach decay of CdS NRs displays multi-exponential decay kinetics, consistent with previous reports.[95,98] The bleach kinetics decay to baseline in ~1 μs and exhibit an average lifetime of 160 ns, calculated from a five-exponential fit. The relatively slow overall electron decay dynamics of CdS NRs have been attributed to a contribution from the slow recombination of the delocalized CB electron with the localized, surface-trapped holes.[95] Addition of **1** in the CdS:**1** ratio of 1:12 has an unusual impact on the electron decay kinetics (Figure 2.9a). For the first 250 ps, the kinetics of CdS alone and in the presence of **1** are essentially superimposable. Following this, the traces diverge and the electron lifetime is shortened from 160 ns to 11 ns. This suggests that after a 250 ps delay, additional kinetic pathways become available, enabling ET from CdS to take place.

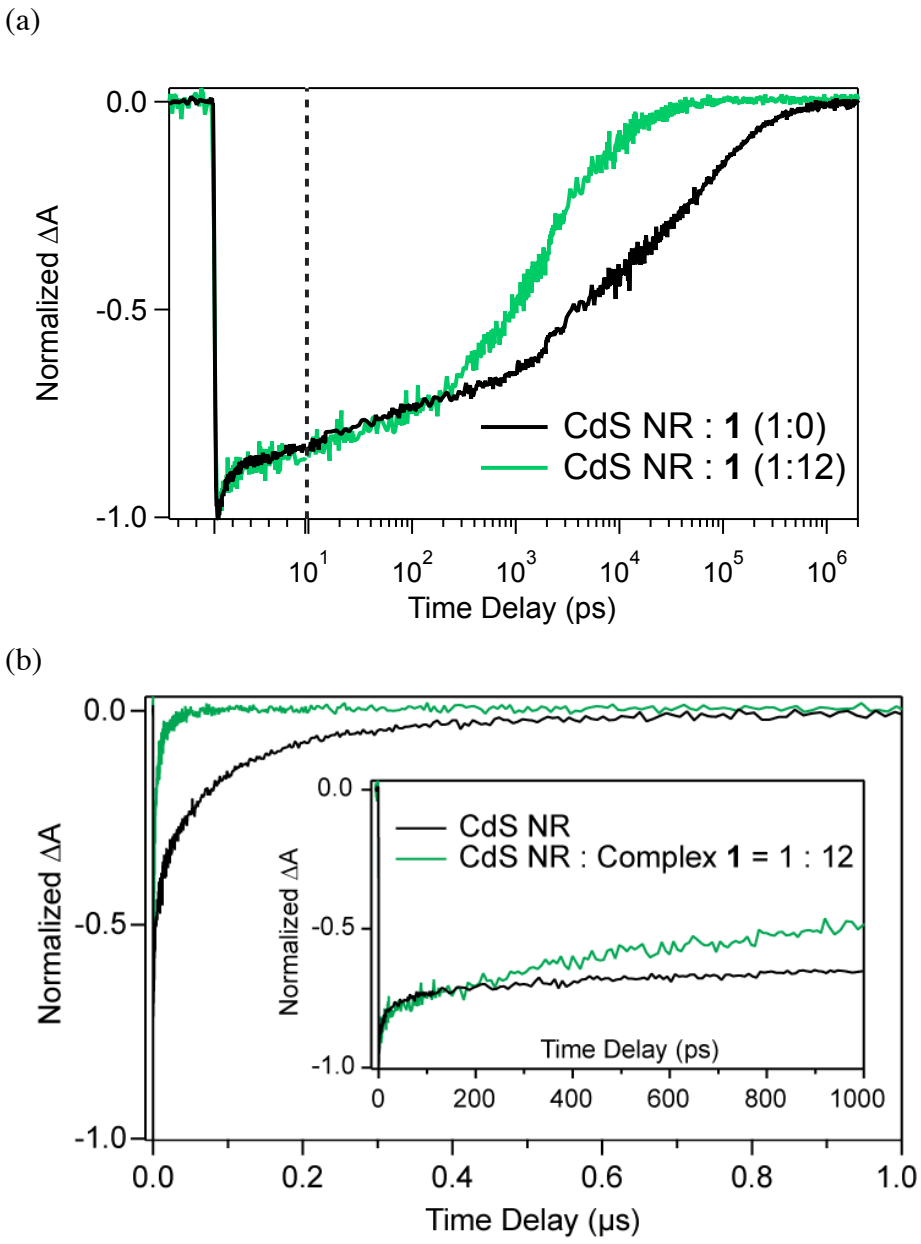

Figure 2.9 TA decay kinetics at 470 nm for CdS NRs in the presence and absence of **1** (λ_{pump} = 400 nm) (a) plotted with a linear time scale until 10 ps and a logarithmic time scale thereafter or (b) plotted with a linear time scale. The inset plot of the first nanosecond of kinetics shows that the two samples have overlapping dynamics for the first 250 ps before diverging due to ET. Adapted with permission from *J. Am. Chem. Soc.*, 2013, **135**, 3383-3386. © Copyright 2013 American Chemical Society.

The 250 ps delay prior to electron lifetime shortening suggests that an electron acceptor state must first be created before ET can take place. Based on the energy level diagram in Figure 2.3, we hypothesize two sequential charge transfer steps between photoexcited CdS NRs and **1**: HT from CdS to **1** either directly to or terminating with the metal-centered HOMO (oxidizing Ru^{2+} to Ru^{3+}), followed by ET out of the CdS CB into the newly created available site in the same orbital (reducing Ru^{3+} back to Ru^{2+}). Holes can transfer to **1** from both the VB and trap states, as evidenced by quenching of emission signals associated with both. ET from photoexcited **1** to the CB of CdS would manifest as an additional rise in the bleach signal, and is not observed. We note that a similar lack of change in the early TA dynamics during HT was reported for the case of CdSe nanocrystals coupled to a Ru(II) tris-bipyridyl complex.[86]

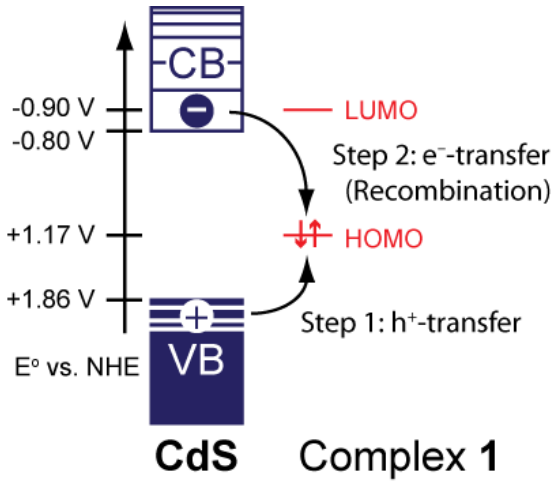

Figure 2.10 Energy level diagram with the proposed charge transfer steps between photoexcited CdS and **1**. Adapted with permission from *J. Am. Chem. Soc.*, 2013, **135**, 3383-3386. © Copyright 2013 American Chemical Society.

2.3.4 Assignment of Charge Transfer Decay Kinetics

To support our hypothesis and the assignment of processes revealed by the TA data, we performed a series of TA experiments using molecular hole and electron acceptors mixed with CdS NRs (Figure 2.11). When ascorbate (Asc), a hole scavenger, is added to CdS NRs, no change in the early kinetics of the band gap bleach is observed (Figure 2.11, orange trace). This is consistent with the assignment of the bleach to electrons in the CB, and lack of HT signature in the TA signal.[86,99] In contrast, when methylene blue (MB), an electron acceptor, is added to CdS NRs the divergence from the CdS-only trace is observed after 3 ps (Figure 2.11, blue trace). This is consistent with a previous report of ET from nanocrystals to MB.[100] This data indicates that the delayed onset of ET in CdS-**1** system is significantly different from a "pure" ET case, and points to another photoexcited process that precedes ET. Finally, we consider that within our model, the presence of the hole scavenger Asc in the CdS-**1** solution would provide a competing destination for the holes, decrease the population of Ru^{3+}, and circumvent the subsequent ET process. This is seen in Figure 2.11 (red trace) as the lack of the ET signature for CdS + **1** + Asc (i.e., the trace is similar to CdS alone and CdS with Asc). The oxidized form of Asc has an absorption peak at 380 nm,[101] and its accumulation was observed following this TA experiment (Figure 2.12), indicating that hole transfer to Asc took place. The observed quenching of electron transfers with the introduction of ascorbate into solution was attributed to hole transfer into the ascorbate interfering with the electron-hole recombination. We believe the ascorbate was not shielding the interaction between CdS and complex **1**. The addition of $NaPF_6$ salt into the a similar solution of CdS:**1** did not quench the electron transfer as $NaPF_6$ does not act as a charge accepting molecule (Figure 2.13).We note that the stepwise charge transfer behavior, along with

the lack of overlap between CdS emission and **1** absorption, allows us to rule out energy transfer as the mechanism of PL quenching seen in Figure 2.4.

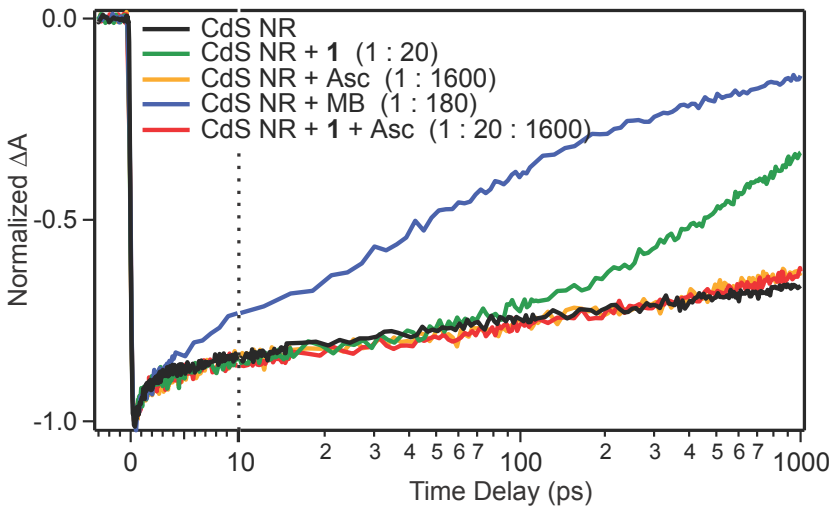

Figure 2.11 TA decay kinetics at 470 nm for CdS NRs alone, and in the presence of: complex **1**, the hole scavenger ascorbate (Asc), the electron acceptor methylene blue (MB), and both **1** and Asc. Adapted with permission from *J. Am. Chem. Soc.*, 2013, **135**, 3383-3386. © Copyright 2013 American Chemical Society.

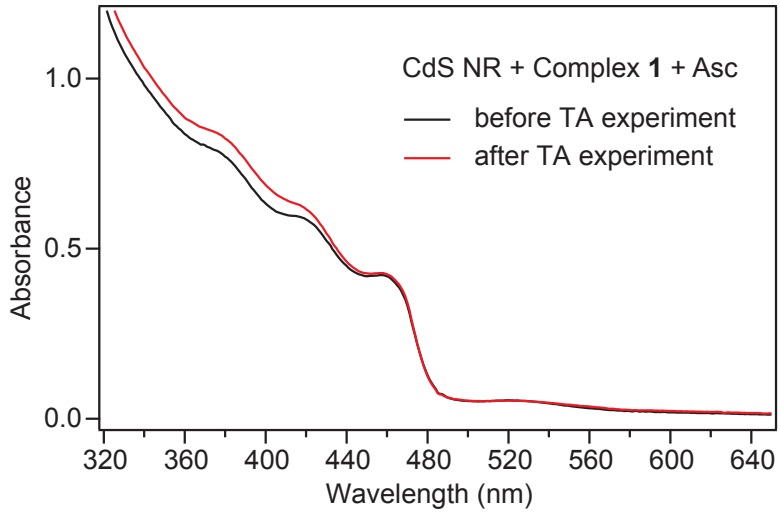

Figure 2.12 Steady-state absorption spectra of a sample containing CdS NRs, complex **1**, and ascorbate (Asc) taken before and after TA data collection. The difference in absorption around 380 nm can be attributed to an increase in the concentration of an oxidized form of ascorbate.[101] Adapted with permission from *J. Am. Chem. Soc.*, 2013, **135**, 3383-3386. © Copyright 2013 American Chemical Society.

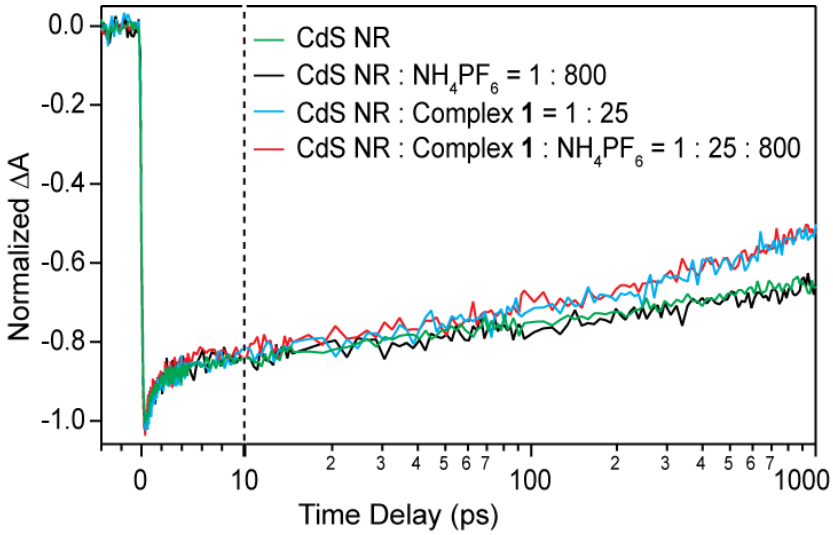

Figure 2.13 TA kinetics of of CdS with the addition of PF_6^- salt for increased ionic strength in solution. The PF_6^- salt does not alter the TA decay kinetics for CdS nanorods of a CdS:**1** solution. Adapted with permission from *J. Am. Chem. Soc.*, 2013, **135**, 3383-3386. © Copyright 2013 American Chemical Society.

2.3.5 Electron Decay Kinetics for Varying CdS NR: Complex 1 Molar Ratios

The dependence of CdS band gap bleach decay kinetics on the CdS:**1** ratio, with CdS NR concentration held constant, is shown in Figure 2.14. Over the ratio range of 1:8 to 1:94, the onset time for ET decreases from 370 ps to 90 ps. At the same time, the average electron lifetime decreases from 44 ns to 1 ns, and the quantum efficiency of ET increases from 72 % to 99 %. As shown in Figure 2.14, the dependence of these values on the concentration of **1** exhibits saturation behavior similar to that shown in Figure 2.4 for PL quenching. We do not have enough information to determine the coverage of CdS NRs with **1** under varying mixing ratios. We can, however, estimate that under low-coverage conditions (on the order 1-10 adsorbed molecules per NR), HT occurs on a 100 ps – 1 ns timescale and subsequent ET occurs with at least a 10 – 100 ns lifetime. The HT timescale falls within the range of observed values for HT from Cd-chalcogenide nanocrystals to molecular hole acceptors (5 ps – 50 ns) with a variety of coupling conditions and relative energy level alignments.[2] The ET, on the other hand, is significantly slower than values previously reported for common electron acceptors, such as viologens, MB, and polyaromatic quinones, which are typically <100 ps.[2] The relatively slow ET may be due to a combination of low wavefunction overlap between the hole localized on Ru^{3+} and the electron delocalized in a CdS NR, significantly different electronic couplings for the HT and the ET pathways, and the very large driving force for ET (~1.9 eV) placing the process in the Marcus inverted regime. Further work is needed to elucidate the factors that determine the HT and ET rates in this system.

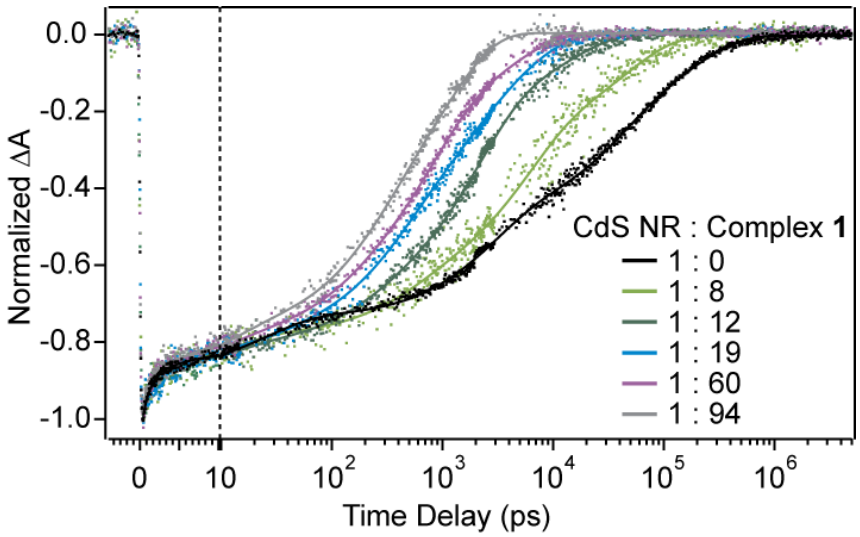

Figure 2.14 TA kinetics of CdS NRs with fixed concentration of CdS NRs and varying CdS NR:**1** ratios. The excited state lifetime shortens with increasing concentration of **1**. Solid lines are five-exponential fits to the data. Adapted with permission from *J. Am. Chem. Soc.*, 2013, **135**, 3383-3386. © Copyright 2013 American Chemical Society.

2.3.6 Model for Analysis of TA Decay Kinetics

The TA kinetics in Figure 2.14 provides information about timescales of both the hole transfer (HT) and electron transfer (ET) events between CdS NRs and **1**. Within our model (Figure 2.10), HT from CdS valence band and hole traps to the HOMO of **1** is followed by ET from the CdS conduction band into the newly available empty state in **1**, resulting in overall electron-hole recombination at the metal center.

The point at which the CdS-**1** kinetics diverge from the CdS kinetics was defined as the onset of ET (HT must occur before an electron acceptor state becomes available). The determination of the point of divergence is somewhat subjective, but we can estimate it by the following method: with a logarithmic x-axis, for each complex **1**: CdS NR sample, the ns-range ET pathway was fit to a line. The intersection of this line with a line parallel to the 1 ps-1 ns

portion of the CdS-only decay was estimated to be the ET onset time. The results are summarized in Table 2.1 and plotted in Figure 2.15a. Note that the ET onset times exhibit a saturation behavior similar to that shown by PL quenching (Figure 2.4).

Information about the dynamics of the ET that follows HT is provided by the kinetics of the bleach decay. Because the CdS band gap decay behavior is multi-exponential, we cannot form a meaningful physical model attributing each component to a specific process without additional information. Instead, we focus on values that are relatively insensitive to the number of fit parameters. The average excited state lifetimes were calculated as,[102]

$$< \tau_{measured} > = \frac{\sum_i a_i \tau_i^2}{\sum_i a_i \tau_i} \qquad \text{Equation 2.5}$$

where a_i and τ_i are the parameters from a multi-exponential fit. For CdS alone, we determined, by inspection of the residual, that the minimum number of exponentials needed for a good fit is five. The time-components obtained were at least one order of magnitude apart in time. For CdS-**1** samples, the fits to both four and five exponentials were suitable and they resulted in essentially identical values of $< \tau_{measured} >$ (Table 2.1).

Table 2.1 Results of analysis of TA dynamics displayed in Figure 2.14.

CdS NR:1 ratio	**Onset of ET (ps)**	**$<\tau_{measured}>$ (5-exp fit) (ns)**	**$<\tau_{measured}>$ (4-exp fit) (ns)**	**QE_{ET} (%)**	**$<\tau_{ET}>$ (ns)**
1:0	N/A	160	Does not fit	N/A	N/A
1:8	370	44	43	72	61
1:12	250	11	11	92	12
1:19	130	4.3	3.9	96	4.5
1:60	115	3.4	3.0	97	3.5
1:94	90	1.0	1.0	99	1.0

Since ΔA is proportional to the electron population, integral of the decay signal is proportional to the total population over the decay time. We can calculate the quantum efficiency of electron transfer (QE_{ET}) from the integrated areas under the kinetic decays or their fitting curves using[102]

$$QE_{ET} = 1 - \frac{\int \Delta A(CdS+\mathbf{1})}{\int \Delta A(CdS)} \qquad \text{Equation 2.6}$$

Then we can estimate the average lifetime of ET ($< \tau_{ET} >$) by adapting the expression used for single-exponential excited state decays, $\tau_{ET} = \frac{\tau_{measured}}{QE_{ET}}$, as

$$< \tau_{ET} > \approx \frac{< \tau_{measured} >}{QE_{ET}} \qquad \text{Equation 2.7}$$

For consistency, we used $<\tau_{measured}>$ values from five-exponential fits, but essentially identical numbers are obtained from four-exponential fits for the CdS-**1** complexes. Eq. 2.7 likely underestimates τ_{ET} because longest-lived components likely have highest efficiencies of ET. Nevertheless, this treatment allows us to determine lower limits for ET lifetimes. The results of this analysis are summarized in Table 2.1and plotted in Figure 2.15b.

(a)

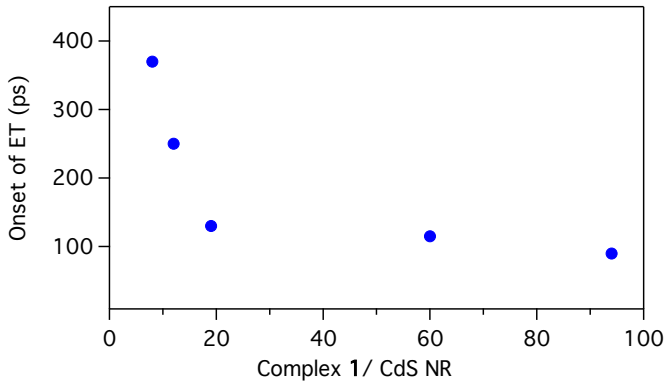

(b)

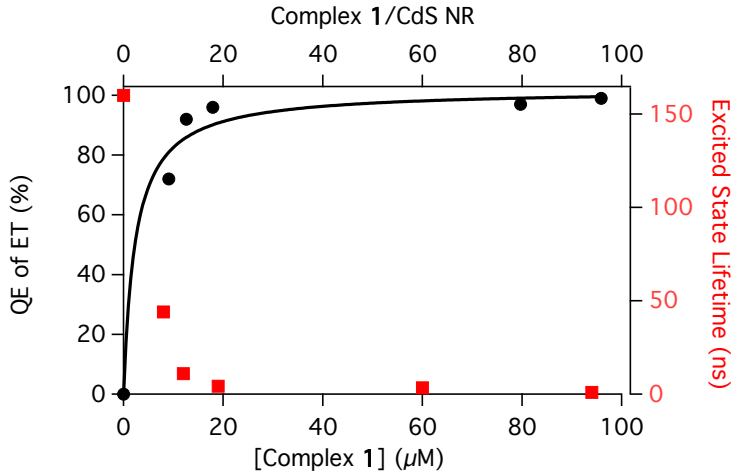

Figure 2.15 (a) The onset of ET as a function of **1**:CdS NR ratio. (b) QE_{ET} and the excited electron lifetimes plotted versus both concentration of **1** and **1**:CdS NR ratio. The three quantities plateau at high ratios. The QE_{ET} was fit with the Langmuir isotherm model (Eq. 2.3) and the resulting parameters were $K=4.2x10^5$ M^{-1} and $(\Delta I/I_0)_{max} = 1.0$. The difference in the values of K seen in the PL and TA can be attributed to the difference in CdS NR concentrations between the two experiments.[96] Adapted with permission from *J. Am. Chem. Soc.*, 2013, **135**, 3383-3386. © Copyright 2013 American Chemical Society.

We expected the HT and ET processes to have similar dependencies on the concentration of **1** because the fraction of photoexcited CdS NRs that undergo ET is governed by the fraction that first undergo HT, which in turn depends on the initial concentration of **1**. This is evident in

the comparison of Figure 2.15a and b, where the HT onset and the excited electron lifetime (and therefore the rate of ET) both exhibit saturation behavior similar to that seen for PL quenching (Figure 2.7). To estimate the HT and ET timescales at low **1** coverage, we consider the pre-saturation linear ranges in Figure 2.15a for HT and Figure 2.15b (red) for ET. We do not have enough information to determine the number of molecules adsorbed per NR for each mixing ratio, but since the **1**:CdS NR ratio is <20 in the linear range, we can estimate that there are 1-10 adsorbed molecules per NR. The onset of ET, and therefore the timescale for HT is between 100 ps and 1 ns (Table 2.1 and Figure 2.15). The range for τ_{ET} is 10-100 ns (Table 2.1).

2.3.7 Charge Transfer Dynamics for Varied CdS NR Sizes

The length tunability of the CdS NRs was utilized to further investigate the nanocrystal-complex **1** interaction as observed by the charge transfer signal. The TA kinetic traces in Figure 2.16 are obtained on CdS NRs with lengths of 13 and 36 nm and their mixtures with similar ratios of **1**. It can be seen that the TA kinetics at 470 nm are identical for CdS NRs with both sizes. However, in the presence of **1**, the bleach of the shorter NRs (13 nm) is quenched faster than the longer NRs (36 nm), which indicates a higher electron-transfer rate. CdS NRs of different lengths have different surface areas per NR. The approximate surface area of the 13nm-long NRs is 197 nm^2 and 499 nm^2 for the 36 nm-long NRs. If **1** has an estimated footprint of 1 nm^2, 20 molecules of **1** on a 13 nm-long NR gives a maximum surface coverage of 10%. The sample of 36 nm-long NRs with 25 molecules of complex **1** per NR has a maximum surface coverage of 5%. When the TA kinetic traces are normalized to -1 at the maximum bleach, the kinetics of each CdS NRs by themselves decay by 19% within 1 ns (Figure 2.16a; black and red traces). The kinetics of the 13 nm-long CdS-**1** (1:20) decay by 52% (Figure 2.16a; grey trace)

and the kinetics of the 36 nm-long CdS-**1** (1:25) decay by 36% (Figure 2.16a; maroon trace) in 1 ns. The 13 nm-long CdS NRs with two times the estimated fractional surface coverage of charge accepting molecules (complex **1**) shows 50% more electron transfer within 1 ns. The observed change in the extent of bleach quenching suggests the charge transfer is related to the fraction surface coverage of complex **1** rather than just the ratio of complex **1** per CdS NR. Further work is necessary to determine the relationship between size, surface coverage, and ET rate.

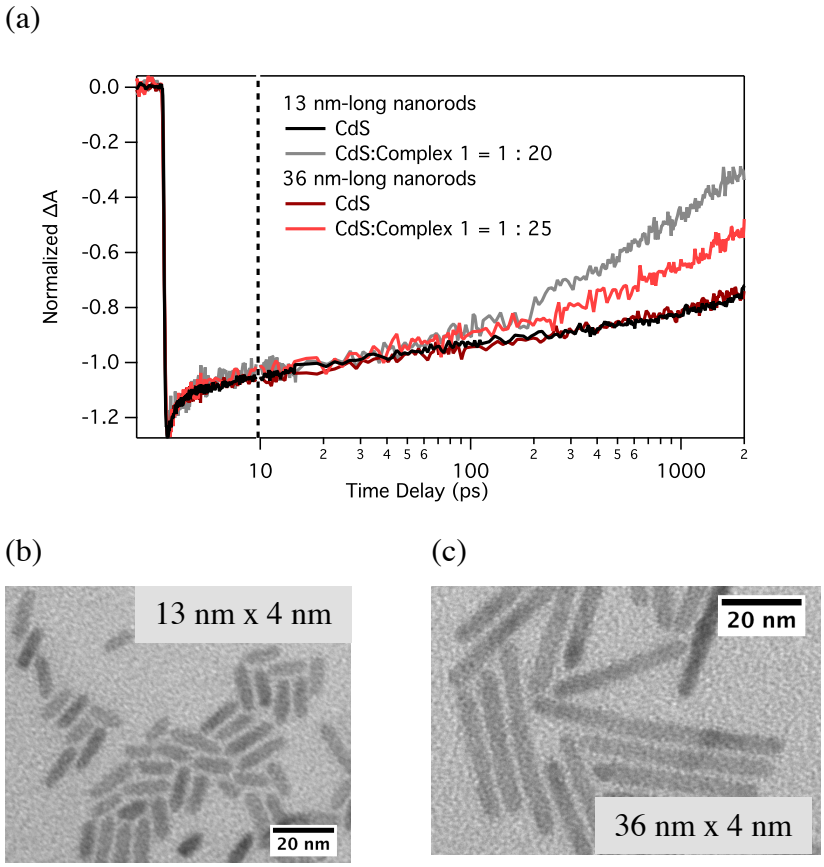

Figure 2.16 (a) TA decay kinetics at 470 nm of two different sizes of CdS NRs alone and in the presence of complex **1**. (b) TEM image of the shorter (13 nm) length CdS NRs. (c) TEM image of the longer (36 nm) length CdS NRs.

2.4 Conclusions

In summary, we have described the charge transfer interactions between photoexcited CdS NRs and the water oxidation catalyst [Ru(deeb)(tpy)Cl](PF_6). We found a step-wise charge transfer mechanism that involves hole transfer from photoexcited CdS to the HOMO of [Ru(deeb)(tpy)Cl](PF_6), occuring on a 100 ps – 1 ns timescale, followed by electron transfer from the conduction band of CdS to the same orbital on [Ru(deeb)(tpy)Cl](PF_6), which is considerably slower at 10 – 100 ns. The second step could be averted through introduction of additional electron harvesting pathways.

These results have significant implications for photochemical water splitting. Under the conditions of our current experiment, the metal center acts as a recombination site where each HT event that oxidizes Ru^{2+} is followed by an ET event that reduces the site. However, the ET timescale is relatively slow. We propose that additional pathways can be designed to funnel away photoexcited electrons and allow for the accumulation of multiple holes on the catalyst, thereby facilitating O-O bond formation. Examples of potential electron destinations include molecular acceptors and catalysts for H^+ reduction.[2] Furthermore, built-in charge separation in the so-called type-II nanoheterostructures could assist in electron removal from the nanocrystal.[2] The nanocrystal-water oxidation catalyst hybrid could serve as a unit in a more complex photochemical water splitting architecture. Additionally, we expect that improved understanding of the binding equilibrium between CdS NRs and catalysts will allow us to negotiate the competition for holes among multiple catalysts on each NR. Finally, we note that efficient delivery of photoexcited holes to the water oxidation catalysts has the added benefit of preventing nanocrystal photo-oxidation.

Chapter 3 Characterization of Electron Transfer Kinetics in CdS Nanorod-[FeFe]-hydrogenase Complexes and Implications for Photochemical H_2 Generation ‡

3.1 Introduction

Colloidal semiconductor nanocrystals are excellent model light harvesting elements for artificial photosynthesis because they are strong light absorbers with tunable particle size, shape, electronic structure, absorption spectra, and surface chemistry.[2,18,22,103-106] In recent years, semiconductor nanocrystals have been coupled with a variety of redox catalysts in solution-phase nanoarchitectures that use visible light to drive reduction of two protons to produce H_2.[2,74] The catalysts include noble metal nanoparticles,[4,5,8,11,24,25,28] transition metal complexes,[13,33] enzymes,[6,9,12,38,39] and molecular mimics of enzyme active sites.[7,14,107,108] This chapter is focused on the coupling of nanocrystals with hydrogenase, a remarkable biological catalyst that can reversibly generate H_2 very close to the thermodynamic potential.[51,56,67,109,110] Hydrogenases utilize redox cofactors composed of earth-abundant elements (Fe, Ni, S) for electron transport and catalysis. [FeFe]-hydrogenases, in particular, exhibit high catalytic activities for H^+ reduction to H_2.[111,112] In nature, H_2 generation catalyzed by [FeFe]-hydrogenases requires injection of low-potential electrons from ferredoxin (Fd) to a distal iron-sulfur cluster (F-cluster) near a

---

‡ Adapted from K. A. Brown, M. B. Wilker, M. Boehm, G. Dukovic and P. W. King, *J. Am. Chem. Soc.*, 2012, **134**, 5627-5636. (© Copyright 2012 American Chemical Society) and M. B. Wilker, K. E. Shinopoulos, K. A. Brown, D. W. Mulder, P. W. King and G. Dukovic, *J. Am. Chem. Soc.*, 2014, **136**, 4316-4324. (© Copyright 2014 American Chemical Society)

positively-charged surface patch of the enzyme.[64,66,113,114] Electron injection is followed by electron transport through accessory iron-sulfur clusters to the active site (H-cluster), where two protons are reversibly reduced to H_2.[58,115,116] It is thought that the active sites of [FeFe]-hydrogenases have metastable 1-electron reduced states that can persist until a second electron arrives and H_2 is generated.[117-119]

As introduced in Chapter 1, we demonstrated that complexes of CdS nanorods (NRs) and [FeFe]-hydrogenase from *Clostridium acetobutylicum* (CaI) generate H_2 under illumination (Figure 3.1b), with quantum yields ($QY(H_2)$) of up to 20% at a CaI:CdS NR molar ratio of ~1:1 (Table 3.1).[12] $QY(H_2)$ is defined as (H_2 molecules produced/photons absorbed)*(2 electrons/H_2 molecule).[12] CaI exhibits high catalytic activity with turnover frequencies (TOFs) up to ~10^4 (H_2 molecules)/(enzyme*s).[63] The CdS-CaI complexes form via a biomimetic interaction in which CdS NRs, capped with negatively-charged surface ligands, bind to CaI as analogs of the electron-donating protein Fd (Figure 3.1a).[6,12] We proposed a model for photochemical H_2 generation that involves light absorption by CdS NRs and injection of photoexcited electrons (i.e., electron transfer (ET)) into CaI, which can then utilize two electrons to reduce two protons and generate one H_2 molecule (Figure 3.2).[12] Holes are removed by the electron donor ascorbate ($AscH^-$).[101] The biomimetic binding interaction suggests that the electrons injected from CdS should follow the biological pathway, with electron injection at a distal F-cluster followed by electron transport to the H-cluster.[6,9,12,39,63] H_2 production efficiency by the CdS-CaI heterostructures was shown to be linear with photon flux. This indicated that the H_2 generation was limited by the availability of electrons (photon flux × efficiency of ET), and not by the turnover capacity of the enzyme. H_2 production rate slowed after 30 minutes and ceased after 4

hours, with the overall TON on the order of 10^6. The cessation was attributed to deactivation of the enzyme by small amounts of free MPA molecules photo-oxidized off the nanocrystal surface. CdS nanorods were not significantly changed during H_2 generation and neither precipitation nor degradation of nanocrystals was observed.

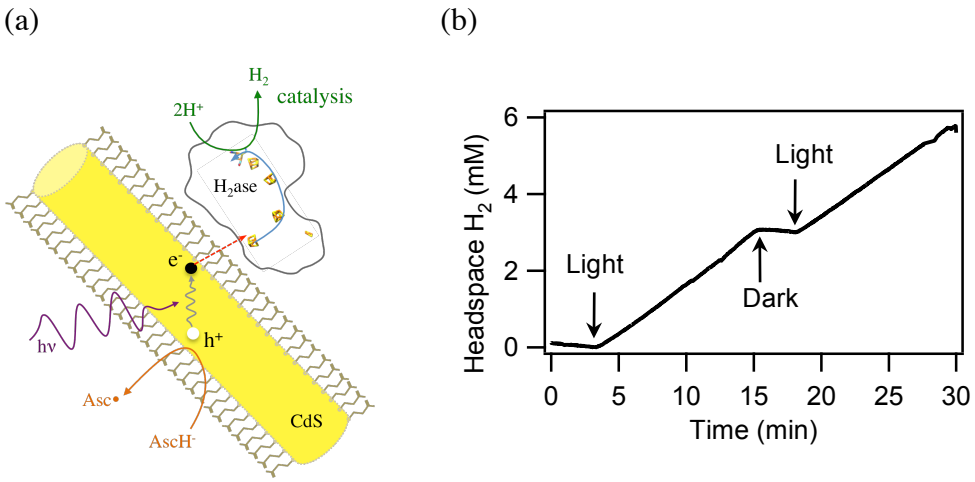

Figure 3.1 (a) The proposed scheme for photocatalytic H_2 production by CdS-CaI complexes. Electron-transfer [FeS] clusters are shown in yellow (S) and orange (Fe). CdS and CaI are drawn to scale, but the ligands are enlarged ~5x. (b) Photocatalytic H_2 production by CdS-CaI complexes in 50 mM Tris-HCl, 275 nM CdS, 360 nM CaI, and 100 mM $AscH^-$ illuminated with white light. Adapted with permission from *J. Am. Chem. Soc.*, 2012, **134**, 5627-5636. © Copyright 2012 American Chemical Society.

Table 3.1 QY measurements for the 1-to-0.67 CdS-to-CaI complex. Samples consisted of 14 nM CdS NR, 9 nM CaI and 100 mM $AscH^-$ and were incubated for 10 minutes before illumination. Incident and absorbed laser powers were measured at 0 and 10 minutes to rule out variations in laser intensity and changes in sample absorbance during the experiment.

Sample	Incident power (mW)	Power absorbed (mW)	Absorbance (t=0, min)	Absorbance (t=10, min)	Photons absorbed (nmol)	H_2 produced (nmol)	QY(%)
1	0.97	0.13	0.13	0.14	262	28.7	21.9
2	1.03	0.14	0.13	0.14	287	28.9	20.2
3	0.97	0.17	0.15	0.16	352	33.6	19.1
4	1.27	0.19	0.15	0.15	383	38.9	20.3
5	1.01	0.20	0.16	0.16	411	41.1	20.0
6	1.02	0.19	0.15	0.16	386	41.5	21.5
7	1.07	0.20	0.15	0.15	403	39.7	19.7

Critical to our understanding of photochemical H_2 generation in CdS-CaI complexes is the fact that electron relaxation pathways in CdS NRs, such as trapping and recombination, are in kinetic competition with ET to CaI (Figure 3.2). The quantum efficiency of ET to CaI (QE_{ET}), defined as (electrons transferred)/(photons absorbed), depends on the ratio of the ET rate constant (k_{ET}) and the rate constant of the internal electron decay processes (k_{CdS}). The value of QE_{ET} defines the upper limit on the value of $QY(H_2)$ because only electrons delivered to CaI can be incorporated into H_2 molecules. The measured value of $QY(H_2)$ will be lower than that of QE_{ET} if there are subsequent rate-limiting processes in H_2 generation. To understand the factors that determine QE_{ET}, its relationship to $QY(H_2)$, and to propose strategies for the improvement of H_2 production efficiency, it is necessary to directly measure the values of k_{ET} and k_{CdS}.

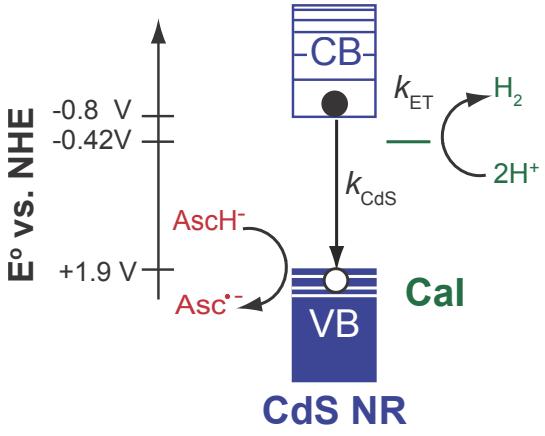

Figure 3.2 Energy level diagram depicting the processes required for photochemical H_2 generation by CdS-CaI complexes. Photoexcitation of CdS is followed by electron transfer from CdS to CaI, denoted with the rate constant k_{ET}. Two electrons are utilized for the reduction of $2H^+$ to H_2. Holes are scavenged by the electron donor ascorbate ($AscH^-$). k_{CdS} represents the rate constant for electron decay pathways in the CdS NRs, including radiative and nonradiative recombination and carrier trapping. These processes compete with ET. Adapted with permission from *J. Am. Chem. Soc.*, 2014, **136**, 4316-4324. © Copyright 2014 American Chemical Society.

In this Chapter, we describe the first measurements of rates and efficiencies of ET between photoexcited CdS and CaI in the CdS-CaI complexes described above using transient absorption (TA) spectroscopy. We found that both electron relaxation in CdS NRs and CdS→CaI ET proceed relatively slowly, with rate constants k_{CdS} and k_{ET} $\approx 10^7$ s^{-1}, resulting in a QE_{ET} of 42% when the molar ratio of CaI and CdS NRs is 1:1. We attribute the relatively low value of k_{ET} to the nature of the CdS-CaI interface, which requires electron tunneling over a considerable distance. We found that the rate of electron removal from CdS NRs increases linearly with increasing numbers of enzyme moieties per NR; however, the $QY(H_2)$ decreases as multiple CaI compete for electrons. To probe the pathway of an electron injected into CaI, we performed TA measurements on CdS-CaI complexes with catalytically inactive CaI, which were

not capable of generating H_2. Such complexes exhibited similar ET behavior to complexes of CdS NRs with catalytically active CaI, confirming that the electron trajectory in CdS-CaI complexes is analogous to the natural pathway that electrons follow in [FeFe]-hydrogenases after injection from Fd. In order to increase the fraction of photoexcited electrons delivered to CaI, we propose that both decreasing k_{CdS} and increasing k_{ET} would be beneficial due to their almost equivalent values. Both goals may be achievable via tuning of the nanocrystal structure. The rate of electron transport through CaI, which occurs after electron injection, defines the upper limit on the value of k_{ET} that would be beneficial to H_2 generation efficiency. We conclude our discussion by contrasting the ET kinetics and H_2 production in CdS-CaI complexes with the behavior of CdS-Pt nanoheterostructures that also photochemically produce H_2. Our study of ET kinetics in CdS-CaI complexes allows us to elucidate how the electron injection step from the nanocrystal to the enzyme governs the overall H_2 production efficiency, and provides a first glimpse into the intricate kinetics of photochemical H_2 generation in nanocrystal-enzyme biohybrids.

3.2 Experimental

3.2.1 Sample Preparation

3.2.1.1 CdS Nanorods

The CdS NRs were synthesized according to the method described in Chapter 2.[12,73,83,84] The resulting NRs had an average diameter of 4.3 ± 0.4 nm and an average length of 21.5 ± 5.2 nm for sample CdS α or an average diameter of 4.4 ± 0.6 nm and an average length of 32.0 ± 5.8

nm for sample CdS β, as determined by measurements of over 200 particles in TEM images (Figure 3.3). The molar absorptivity (ε) of the CdS NRs was determined by correlating absorption spectra with Cd^{2+} concentrations determined by elemental analysis (ICP-OES) of acid-digested samples. The estimated value of ε_{350} was 1710 $M^{-1}cm^{-1}$ per Cd^{2+}. The number of Cd^{2+} per NR was estimated from the average NR dimensions. ε_{350} was 1.1 x 10^7 $M^{-1}cm^{-1}$ for CdS α and 1.7 x 10^7 $M^{-1}cm^{-1}$ for CdS β. The electronic transition at the band gap for CdS α and CdS β was determined to be at 470 nm from the steady-state absorption spectra (Figure 3.4). The hydrophobic surface-capping ligands on the as-synthesized CdS nanorods were replaced with 3-mercaptopropionic acid (3-MPA) following the previously reported procedure in Chapter 2, but the resulting particles were redisspersed in 12.5 mM Tris buffer pH 7.[5,12,73] 3-MPA binds to the NR surface through the deprotonated thiol group, leaving the carboxylate group in solution to enable solubility in water.[85] All the procedures described above were carried out under an Ar atmosphere.

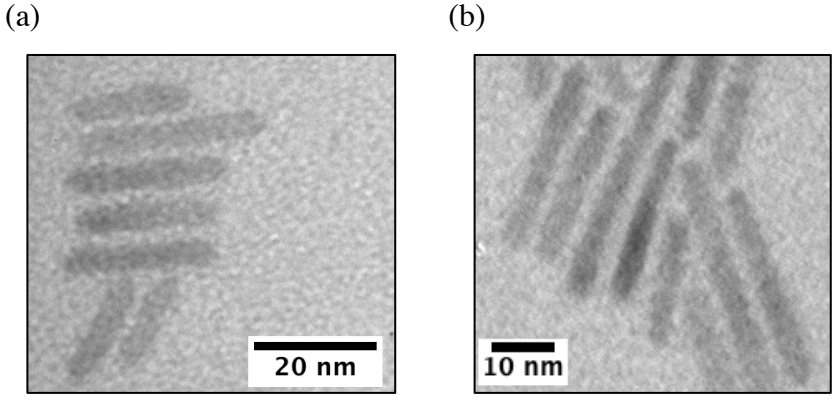

Figure 3.3 (a) TEM image of CdS α NRs. (b) TEM image of CdS β NRs. Adapted with permission from *J. Am. Chem. Soc.*, 2014, **136**, 4316-4324. © Copyright 2014 American Chemical Society.

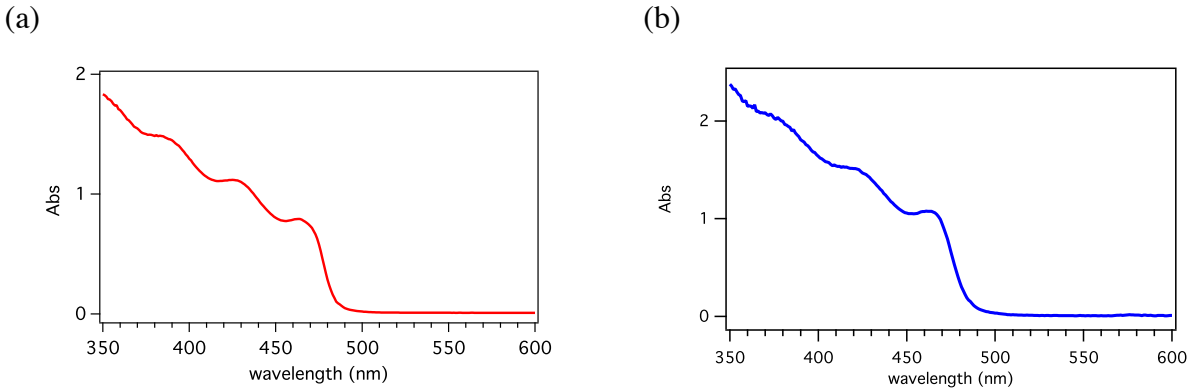

Figure 3.4 (a) Steady-state absorption spectrum of CdS α NRs in buffer. (b) Steady-state absorption spectrum of CdS β NRs in buffer. Adapted with permission from *J. Am. Chem. Soc.*, 2014, **136**, 4316-4324. © Copyright 2014 American Chemical Society.

3.2.1.2 CaI and CaI^{Im} Purification, Characterization, and Coupling to CdS NRs

The StrepII-tagged [FeFe]-hydrogenase from *Clostridium acetobutylicum* (CaI) was expressed and purified from *Escherichia coli* as previously described.[120] Catalytically inactive CaI (CaI^{Im}) was prepared by expression in a genetic background lacking the maturation proteins HydE, HydF, and HydG.[121,122] Cells were harvested in an anaerobic chamber (Coy Labs) under 3% H_2 atmosphere. CaI purification was carried out under strict anaerobic conditions in a glove box (MBRAUN Laboratory Products) under a N_2 atmosphere. In the final Strep-Tactin purification step, CaI was eluted in 50 mM Tris-HCl pH 8.0, 200 mM NaCl, 5% glycerol, and 5 mM sodium dithionite (NaDT). The CaI concentration was determined by Bradford assay (± 10%) using Hemoglobin as the standard[123]. Typical yields were 1-2 mg/L of culture with specific activities between 800-1300 μmol H_2/mg/min. CaI activities were determined by measuring H_2 evolution on a gas chromatograph after addition of 5 mM methyl viologen and 10 mM NaDT. For CaI^{Im}, the Fe content was confirmed on a separate preparation using a colorimetric assay described by Fish.[124]

Mixtures of CdS NRs and CaI were prepared in buffer (50 mM Tris-HCl, 5mM NaCl, 5% glycerol, pH 7) under an anaerobic Ar environment. For CO inactivation, the CdS NRs and CaI were first mixed under Ar in a 2 mm cuvette with an airtight Kontes valve. The headspace was exchanged for CO by flowing CO (99.99%, Airgas) into the cuvette for 30 min while stirring the sample solution. The sample was then sealed with 0.8 atm CO in the cuvette headspace. When the CaI:CdS NR ratio was varied, the concentration and absorbance of the NRs was held constant while the concentration of CaI was varied.

3.2.1.3 Determination of reduction potential of CdS nanorods

Mixtures of 83 nM CdS nanorods and 167 nM methyl viologen (MV, Sigma) were combined under an anaerobic Ar atmosphere in buffers of varying pH (2, 2.5, 3, 3.4, 4 and 4.5).[125,126] Samples were illuminated for 10 min with 405 nm LED light at 800 μE m^{-2} s^{-1} intensity. Absorbance spectra were collected on a Beckman DU800 and the concentration of reduced MV was determined by absorbance at 606 nm. During the illumination time, we assume that MV^+ is a stable radical. Since the redox potential of MV^{2+}/MV^+ is well defined, the potential of the conduction band electrons in photoexcited CdS at standard reaction conditions were determined by extrapolation to pH 7 using the Nernst equation.

3.2.2 Sample Characterization

3.2.2.1 Steady-state Absorption Spectroscopy

UV-visible absorption spectra were recorded in 0.2 cm path length quartz cuvettes at room temperature with an Agilent 8453 spectrophotometer equipped with tungsten and deuterium lamps.

3.2.2.2 Transmission Electron Microscopy (TEM)

TEM samples of CdS NRs were prepared by drop casting from solution onto carbon film, 300 mesh, copper grids from Electron Microscopy Sciences. Images were obtained at room temperature using a Phillips CM100 TEM operating at 80 kV equipped with a bottom-mounted 4 megapixel AMT v600 digital camera. NR dimensions were measured using *ImageJ* software. To prepare CdS-CaI samples for TEM imaging, the grids were first plasma-treated by glow discharge. Then a drop of a dilute (nM) solution of CdS β NRs and CaI was placed onto the grids for 2 min, after which the solvent was wicked away using filter paper. The grids were rinsed with deionized water in the same manner before being stained in H_2O with 2% methylamine vanadate negative stain (NanoVan, Nanoprobes Inc.), which was wicked away in < 10 s. In a negatively stained image, the electron-dense material (CdS) appears dark in contrast to the stained background, while CaI appears light in contrast to the background.

3.2.2.3 Transient Absorption Spectroscopy

The TA experimental setup was previously described in detail in Chapter 2.[73] The samples were prepared and sealed under Ar in 2 mm quartz cuvettes. CdS NR concentration was 600-800 nM. The samples containing both NRs and CaI were mixed in specific molar ratios in

50 mM Tris-HCl buffer without a hole scavenger (i.e., not under turnover conditions). The samples were pumped at 400 nm. The pump beam diameter was ~240 μm and pulse energy was ~10 nJ/pulse. Pump power was chosen by identifying a regime in which the TA decay kinetics were independent of power and did not show signal from Auger recombination,[43] ensuring that the signal originated from NRs excited by absorption of one photon. During data collection, the samples were stirred constantly.

3.2.2.4 Photodriven H_2 Production

Solutions for light-driven H_2 production consisted of 36 nM CdS-CaI complex (1:1 molar ratio) with 200 mM ascorbate (≥99%, Sigma Aldrich) in 50 mM Tris-HCl buffer with 5% glycerol and 5 mM NaCl, pH 7, in 1.5 mL vials sealed with septa. The samples were illuminated with a 405 nm diode laser at 5 mW for 10 min. H_2 was detected in the headspace of the vessel using gas chromatography (Agilent Technologies 7820A, molecular sieve 5A column, Ar carrier gas, TCD detector). Turnover frequencies (TOF) for photochemical H_2 production are expressed in units of mol H_2 mol^{-1} CaI s^{-1}. For the quantum yield calculations, mixtures of CdS nanorods and CaI in molar ratios of 1-to-0.67 CdS-to-CaI molar ratio (14 nM CdS, 9 nM CaI) were prepared in buffer with 100 mM ascorbate. Samples were illuminated in a quartz cuvette with a 3 x 5 mm window with a 1 mW 405 nm laser pointer (Laserglow Technologies) with a spot size of 6 mm^2. Light intensity passing through the sample was measured using a Newport Model 1918-R power meter with an 818-ST-UV UV-enhanced silicon photodetector. The difference between light intensity transmitted through a control cuvette containing 50 mM Tris-HCl buffer (pH 7) and through the sample cuvette corresponded to absorbed intensity. The amount of H_2 produced was measured after 10 min of illumination by GC. The quantum yield was defined as QY = (mol

H_2 produced/mol photons absorbed) * (2 mol photons/mol H_2). Real-time gas analysis of sample headspace was collected by continuous measurement by an Omnistar capillary mass spectrometer.

3.3 Results

3.3.1 Electron decay kinetics in CdS NRs

To directly probe the kinetics of relaxation and ET in CdS NRs, we employed TA spectroscopy over a temporal window of 10^{-13} – 10^{-6} s with time resolution of ~200 fs. Upon excitation with a 400 nm pump pulse, TA spectra of CdS NRs exhibit a transient bleach feature at the 472 nm (Figure 3.5a), corresponding to the band gap transition (Figure 3.4). This feature originates from filling of the $1\sigma_e$ state, and its intensity reflects the photoexcited $1\sigma_e$ electron population.[43] The bleach feature is insensitive to the population of the photoexcited holes.[73,86,99] Thus, the kinetics of the band gap bleach are a signature of electron dynamics. In CdS NRs, $1\sigma_e$ electrons decay by radiative and nonradiative processes, including electron trapping, recombination with valence band holes, and recombination with trapped holes on the surface. Additionally, there is a rapidly decaying (1ps) absorption feature observed at 482 nm. This feature has been previously attributed to the shift of the exciton band in the presence of hot excitons.[43]

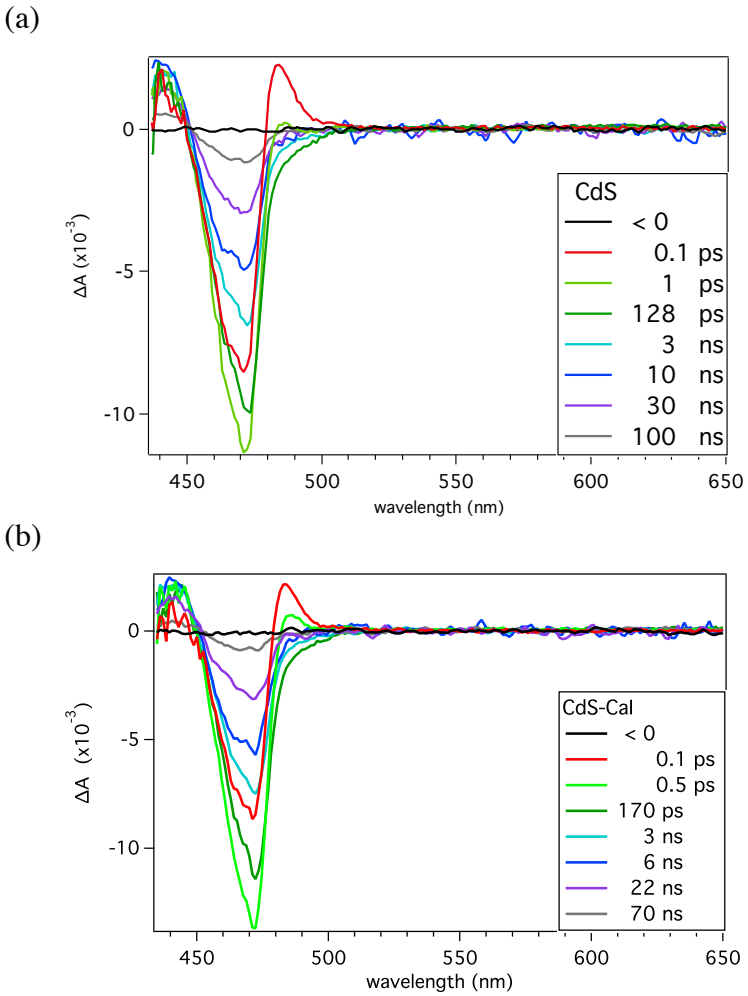

Figure 3.5 Transient absorption spectra of (a) CdS α NRs and (b) CdS α NRs with CaI in a 1:1 molar ratio at different time delays following 400 nm excitation. The CdS NRs exhibit a strong transient bleach feature at the probe wavelength of the band gap (472 nm) transition. The presence of CaI does not change the position or shape of the CdS spectral features. There are no additional transient absorption features associated with CaI. Adapted with permission from *J. Am. Chem. Soc.*, 2014, **136**, 4316-4324. © Copyright 2014 American Chemical Society.

The band gap bleach signal of CdS α NRs is relatively long lived and does not fully decay to baseline until around 1.2 μs (Figure 3.6). The slow electron decay in CdS NRs is accompanied by weak band gap photoluminescence and strong trap-state emission.[73] This behavior has been attributed to slow recombination of the delocalized electron with the localized,

trapped holes.[73,83,95] As evident from the TA signal plotted using a logarithmic time axis (Figure 3.6), the electron decay kinetics in CdS NRs cannot be described with a single exponential function. Such behavior is commonly observed with semiconductor nanocrystals.[98,127-129] The 200 fs time-resolution TA kinetics over 7 orders of magnitude in time were fit to both a single exponential with a stretched exponential fit (Eq 3.1) and a 5 exponential fit (Eq 3.2) (Figure 3.7). For the 300 ps time-resolution TA kinetic data, the kinetic decay was fit with a 3 exponential fit (Eq 3.3). Each fit has a very small y_0 parameter (< 1% of maximum signal) that helps the fit to converge properly. For each fit equation, the number of exponentials needed to fit the data well was defined as the number of exponential components after which the addition of another component did not significantly decrease the value of the sum of squared residuals. The individual fitting parameters were also examined to ensure the τ values were separated by an order of magnitude in time, and the amplitudes of each component were at least 5% of the total amplitude.

$$f(t) = a_0 e^{-(t-t0)/\tau_0} + a_1 e^{-\left((t-t0)/\tau_1\right)^{\beta}} + y_0 \qquad \text{(Equation 3.1)}$$

$$f(t) = a_0 e^{-(t-t0)/\tau_0} + a_1 e^{-(t-t0)/\tau_1} + a_2 e^{-(t-t0)/\tau_2} + a_3 e^{-(t-t0)/\tau_3} + a_4 e^{-(t-t0)/\tau_4} + y_0 \qquad \text{(Equation 3.2)}$$

$$f(t) = a_0 e^{-(t-t0)/\tau_0} + a_1 e^{-(t-t0)/\tau_1} + a_2 e^{-(t-t0)/\tau_2} + y_0 \qquad \text{(Equation 3.3)}$$

The TA kinetics of CdS NRs in Figure 3.6 can be fit with a sum of a single exponential with a 0.85 ps lifetime (10% of the decay) and a stretched exponential with a time constant of 18.2 ns and a stretching factor of 0.49 (90%). Similar behavior was recently reported for CdS NRs with long-chain organic ligands on the surface.[130] The stretched exponential fit suggests a distribution of electron decay rates in CdS NRs, the cause of which is not well understood.[130,131] In the absence of a detailed physical model for the CdS NR electron decay kinetics, we focused on quantities that depend only on signal intensity:[102,132] the average lifetime, defined as

$$\bar{\tau} = \frac{\int_0^\infty t*\Delta A(t)dt}{\int_0^\infty \Delta A(t)dt} \qquad \text{(Equation 3.4)}$$

and the time-averaged decay rate constant, defined as

$$\bar{k} = \frac{1}{\int_0^\infty \Delta A(t)dt} \qquad \text{(Equation 3.5)}$$

where ΔA(t) is normalized so that ΔA(0)= 1. The fit equation, f(t), was used to represent the ΔA intensity of the kinetic data. For the purposes of integration of the ΔA signal, we can use any function that fits the kinetic data well (Figure 3.7). To verify that the results were not strongly dependent on the fitting equation, we compared the single exponential plus stretched exponential fit, described above, to a 5-exponential fit in (Table 3.2). Provided that the fit models the data well, the integration of the ΔA intensity is independent of the fit equation (Table 3.3). The normalized (f(0)=1) fit equation was integrated (without t_0 or y_0) to calculate the average decay time, $\bar{\tau}$, (Eq 3.4) and the time-averaged rate constant, $\bar{k}$, (Eq 3.5) for each kinetic trace. The electron decay kinetics of the CdS NRs shown in Figure 3.6 are characterized by the average lifetime $\bar{\tau}$ of 118 ns and the average decay rate constant $\bar{k}_{CdS}$ of 2.8×10^7 s^{-1}.

(a)

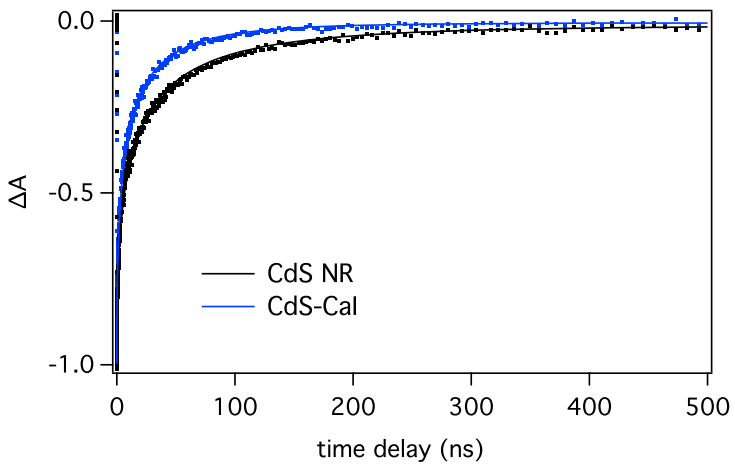

(b)

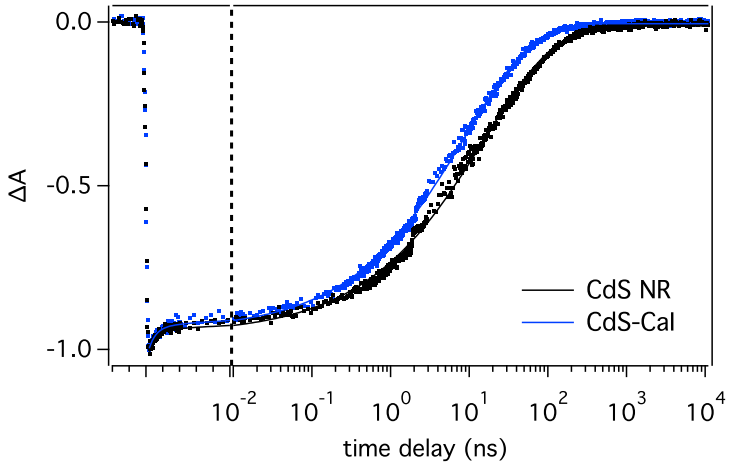

Figure 3.6 TA kinetics of the band gap feature (472 nm) for CdS NRs (black) and CdS-CaI complexes (molar ratio 1:1, blue). The CdS-CaI complexes have a shorter photoexcited electron lifetime due to ET from CdS to CaI. The kinetics are plotted (a) with a linear time axis or (b) with a split time axis that is linear for the first 10 ps and logarithmic thereafter. The solid lines correspond to fit models as described in the text. Adapted with permission from *J. Am. Chem. Soc.*, 2014, **136**, 4316-4324.

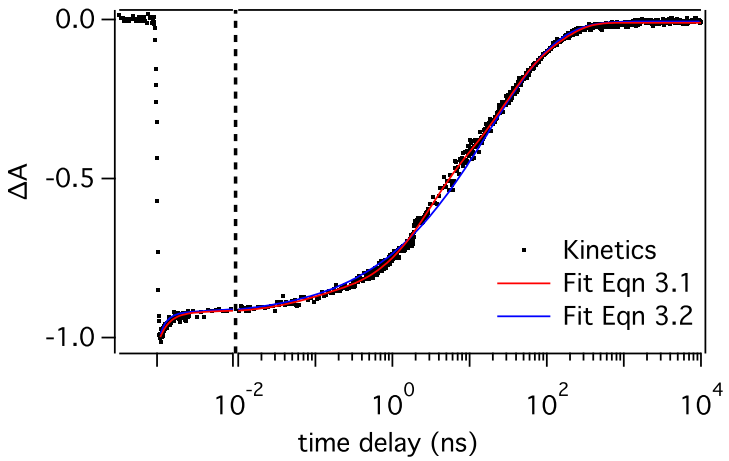

Figure 3.7 CdS α NR band gap TA kinetics (black dots) modeled with Eq 3.1 (blue line) or Eq 3.2 (red line). Adapted with permission from *J. Am. Chem. Soc.*, 2014, **136**, 4316-4324. © Copyright 2014 American Chemical Society.

Table 3.2 Fitting parameters for Figure 3.6 obtained using equations 3.1 and 3.2 to fit the TA kinetics.

Sample		**fit parameters**	
CdS	Eq 3.1	$a_0 = -0.058$ $a_1 = -0.942$	$\tau_0 = 0.85$ ps $\tau_1 = 18.2$ ns $\beta = 0.49$
CaI:CdS (1:1)	Eq 3.1	$a_0 = -0.065$ $a_1 = -0.935$	$\tau_0 = 1.57$ ps $\tau_1 = 11.7$ ns $\beta = 0.51$
CdS	Eq 3.2	$a_0 = -0.076$ $a_1 = -0.050$ $a_2 = -0.339$ $a_3 = -0.334$ $a_4 = -0.201$	$\tau_0 = 1.30$ ps $\tau_1 = 68.7$ ps $\tau_2 = 2.51$ ns $\tau_3 = 23.7$ ns $\tau_4 = 122$ ns
CaI:CdS (1:1)	Eq 3.2	$a_0 = -0.080$ $a_1 = -0.080$ $a_2 = -0.343$ $a_3 = -0.367$ $a_4 = -0.130$	$\tau_0 = 2.33$ ps $\tau_1 = 179$ ps $\tau_2 = 2.28$ ns $\tau_3 = 17.6$ ns $\tau_4 = 84.9$ ns

Table 3.3 The parameter values resulting from the different fit equations that were used for the data in Figure 3.6. The fits of TA data using Eq 3.1 are shown in Figure 3.6.

Sample	fit	$\bar{\tau}$ (ns)	$\bar{k}$ (s^{-1})	QE_{ET}	$\bar{k}_{ET}$ (s^{-1})
CdS	Eq 3.1	118	2.8×10^7	n/a	n/a
CaI:CdS (1:1)	Eq 3.1	62	4.8×10^7	42%	2.0×10^7
CdS	Eq 3.2	96	3.0×10^7	n/a	n/a
CaI:CdS (1:1)	Eq 3.2	58	5.5×10^7	45%	2.5×10^7

3.3.2 ET kinetics in CdS-CaI complexes

As we described previously,[12] the negatively-charged 3-MPA ligands on CdS allow electrostatic binding to a positively-charged surface on CaI. The electrostatic binding likely results in a Poisson distribution of populations.[12] For an average molar ratio of 1:1, 37% of CdS NRs have one CaI moiety attached, 37% have no CaI, and 26% have two or more CaI. TEM images of CdS-CaI complexes obtained using a negative stain (Figure 3.8) allows us to directly visualize the complexes because NRs appear dark and CaI molecules appear bright. The images in Figure 3.8 are consistent with the Poisson distribution model and reflect the heterogeneity of populations, with some CdS NRs having no CaI moieties attached, some having one, and some having multiple.

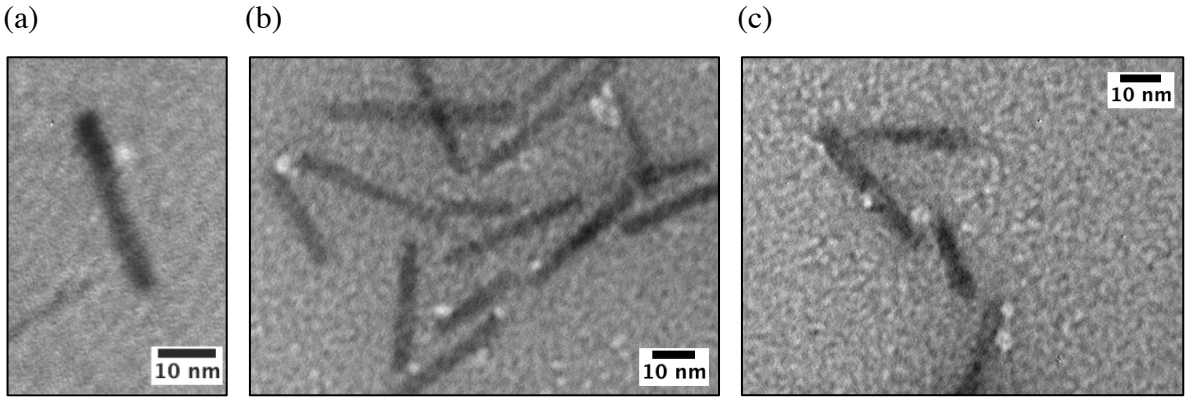

Figure 3.8 TEM images of CdS-CaI complexes stained with NanoVan, a negative stain. The dark contrast areas correspond to NRs while the light contrast areas correspond to the enzyme. Adapted with permission from *J. Am. Chem. Soc.*, 2014, **136**, 4316-4324. © Copyright 2014 American Chemical Society.

When CdS NRs were mixed with CaI in a 1:1 molar ratio, the CdS NR band gap bleach feature decayed to baseline more quickly (Figure 3.6) due to ET to CaI. Because CaI does not have absorptive features with intensities comparable to the strength of the CdS bleach feature,[133] no additional transient features were found in the ΔA spectrum (Figure 3.5b). In the TA experiment, each NR was excited very infrequently because of the low pump pulse repetition rate (500 s^{-1}), low pulse energy, and constant stirring that rapidly moves the sample through the excitation beam. Consequently, the CdS-CaI sample exhibited no changes in absorption intensity or bleach kinetics over a period of several hours in the TA experiment, indicating that there was no sample precipitation or significant electron accumulation on CaI (Figure 3.9). The CdS NRs with and without CaI were stable to precipitation for 24 hours under the air-free conditions in which they were prepared. The samples were stable during the TA experiment as monitored by both steady state absorption spectra (Figure 3.9a) and transient absorption kinetics (Figure 3.9b). The lack of change in steady-state absorption signal allows us to collect reliable TA data for

hours with each sample. Because H_2 production requires two sequential electrons and the experiment was carried out under conditions of low excitation frequency, the sample was not under catalytic turnover conditions, and the TA experiment isolated the one electron transfer step from the CdS NR to CaI.

(a)

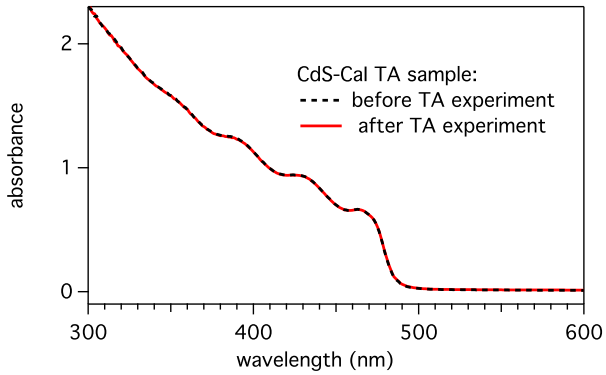

(b)

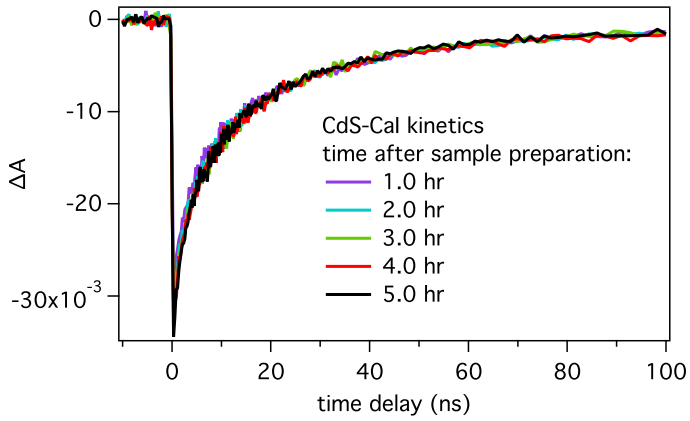

Figure 3.9 (a) Absorption spectra of a TA sample containing CdS-CaI complexes with the average CaI:CdS NR molar ratio of 1:1. Absorption spectra were collected prior to and immediately after the sample was used for TA measurements. No sample precipitation was observed after TA data collection. (b) Unnormalized kinetic data collected over several hours from a single sample containing CdS-CaI. The signal in each of the traces returns to the baseline indicating that the TA samples are completely regenerated to the ground state electron configuration between sequential NR excitations. The TA kinetics do not change over a period of >5hrs. Adapted with permission from *J. Am. Chem. Soc.*, 2014, **136**, 4316-4324.

As shown in Figure 3.6b, the electron decay kinetics of CdS and CdS-CaI virtually overlap in the ps regime, and ET to CaI primarily occurred in the ns time window. The decay kinetics of CdS-CaI can be fit with similar functional forms as CdS electron decay kinetics: a single exponential with a 1.6 ps lifetime (8% of the decay) plus a stretched exponential with a time constant of 11.7 ns and stretching factor of 0.51 (92%), or a 5-exponential decay. The average lifetime of the photoexcited electrons in CdS-CaI, shown in Figure 3.6, is 58 ns. Because of the distribution of decay rates in CdS, it is not obvious whether k_{ET} to CaI is also heterogeneous. An additional complication is the Poisson distribution of CaI:CdS ratios in the sample. Therefore, to characterize ET kinetics, we again used quantities that depend only on signal intensity.[102,132] Specifically, we focused on QE_{ET} and a time-averaged ET rate constant ($\bar{k}_{ET}$):

$$QE_{ET} = \frac{\bar{k}_{ET}}{\bar{k}_{CdS}+\bar{k}_{ET}} = 1 - \frac{\int_0^\infty \Delta A_{CdS-CaI}(t)dt}{\int_0^\infty \Delta A_{CdS}(t)dt} \quad \text{(Equation 3.6)}$$

$$\bar{k}_{ET} = \bar{k}_{CdS-CaI} - \bar{k}_{CdS} = \frac{1}{\int_0^\infty \Delta A_{CdS-CaI}(t)dt} - \frac{1}{\int_0^\infty \Delta A_{CdS}(t)dt} \quad \text{(Equation 3.7)}$$

where $\bar{k}_{CdS-CaI}$ is the time-averaged decay rate constant for the CdS-CaI complexes. As detailed in Table 3.3, we found the value of $\bar{k}_{ET}$ to be 2.0×10^7 s^{-1} with a QE_{ET} value of 42%.

3.3.3 ET kinetics for varying CaI:CdS molar ratios

Figure 3.10 shows how ET kinetics (with 300 ps time resolution) depend on the average number of CaI moieties per CdS NR (CaI:CdS). The CdS NR concentration was held constant and the CaI concentration was varied to obtain the values of CaI:CdS ranging from 0.15:1 to 1.70:1 and 0.9:1 to 5.7:1. For the set of higher ratio experiments, we used longer NRs (CdS β, average length = 32.0 nm) to increase available area for CaI adsorption. With the estimated NR

surface area of 470 nm^2, 6 CaI molecules could adsorb onto the CdS β NR surface without approaching saturation of the available surface area.[12] The NR diameters of CdS β were very similar to those of CdS α, resulting in similar steady-state absorption spectra, a TA bleach peak that is blue-shifted by only 2 nm, and a similar driving force for ET. Figure 3.10 shows the TA decay kinetics at 470 nm and the triple-exponential decay functions that fit the data well. The excited state electron lifetimes ($\bar{\tau}$) decreased with increasing values of CaI:CdS, ranging from 83 ns with 0.15:1 ratio to 40 ns with 5.7:1 ratio. When the average molar ratio of CaI and CdS NRs is not 1:1, $\bar{k}_{ET}$ and $\bar{k}_{CdS-CaI}$ (rate constants) in Eq 3.7 are replaced with average rates of ET and electron decay in CdS-CaI, which are determined by integrating the TA signal according to Eq 3.7. Figure 3.11b shows that the ET rate scales approximately linearly with the value of CaI:CdS in this range of ratios. Following first-order kinetics, we can write that ET rate = $\bar{k}_{ET}$*(CaI:CdS) to obtain a value of $\bar{k}_{ET}$ from a broader data set than the one shown in Figure 3.6. From the linear fit in Figure 3.11b, we obtain a $\bar{k}_{ET}$ value of 1.3 x 10^7 s^{-1}, which is within a factor of 2 of the value for the CdS-CaI (1:1) sample in Figure 3.6.

To account for the varying values of CaI:CdS, QE_{ET} can be written as:

$$QE_{ET} = \frac{\bar{k}_{ET*(CaI:CdS)}}{\bar{k}_{CdS}+\bar{k}_{ET*(CaI:CdS)}} \quad . \qquad \text{(Equation 3.8)}$$

As shown in Figure 3.11a, QE_{ET} increases with increasing CaI:CdS, but above a ratio of 1:1, the dependence of QE_{ET} on CaI:CdS is relatively weak because $\bar{k}_{CdS}$ is within the same order of magnitude as $\bar{k}_{ET}$. QE_{ET} reaches a value of 77% at the ratio of 5.7:1. To obtain the ratio $\bar{k}_{CdS}$ /$\bar{k}_{ET}$, Eq 3.8 can be rearranged to

$$\frac{1}{QE_{ET}} = (\frac{\bar{k}_{CdS}}{\bar{k}_{ET}})(\frac{1}{CaI:CdS}) + 1 \; . \qquad \text{(Equation 3.9)}$$

The plot of $1/QE_{ET}$ vs. 1/(CaI:CdS) yields the $\bar{k}_{CdS}/\bar{k}_{ET}$ value of 1.2 (Figure 3.11c), which is consistent with our findings in Figure 3.6, where the value of $\bar{k}_{CdS}/\bar{k}_{ET}$ was 1.4.

(a)

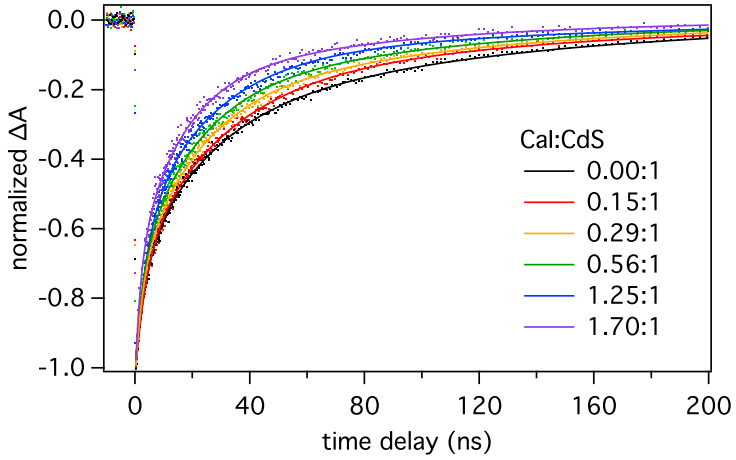

(b)

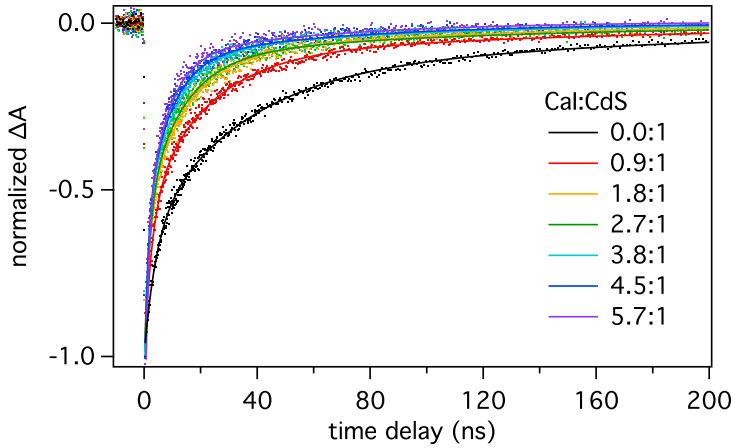

Figure 3.10 Band gap TA kinetics of (a) CdS α and (b) CdS β with varied amounts of CaI. TA kinetic decays (at 470 nm) of CdS-CaI samples with varying values of CaI:CdS (average number of CaI moieties per CdS NR) and constant CdS concentration. The kinetics show that with increasing CaI:CdS, the CdS electron decay occurs more quickly, corresponding to increasing ET signal. Adapted with permission from *J. Am. Chem. Soc.*, 2014, **136**, 4316-4324. © Copyright 2014 American Chemical Society.

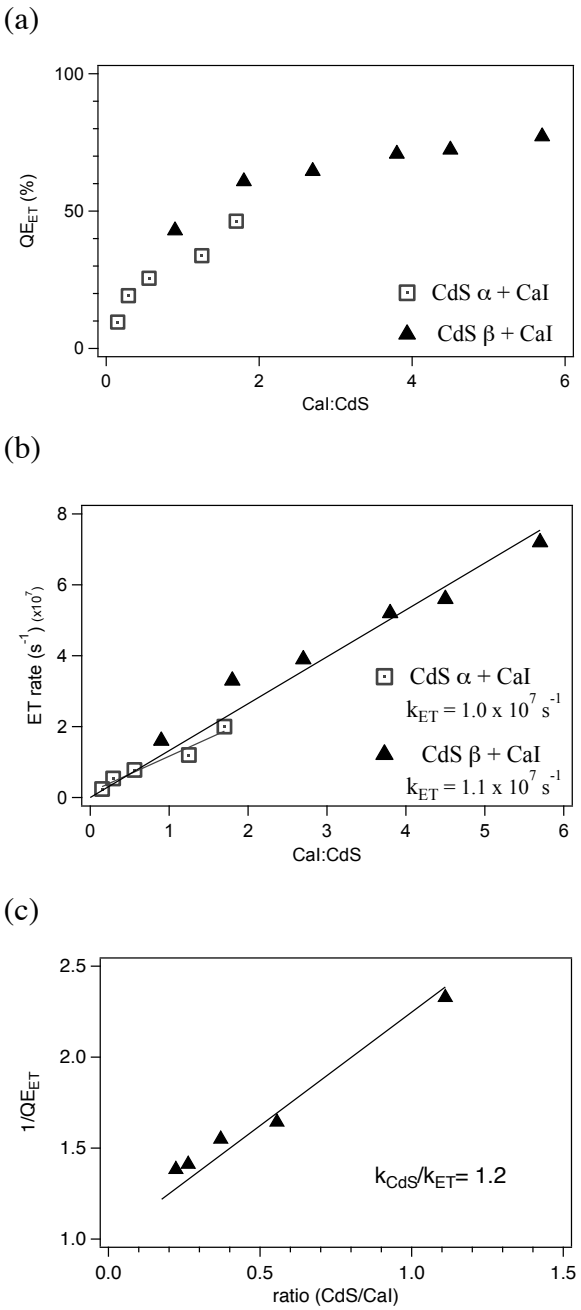

Figure 3.11 A comparison of the TA kinetics for samples with varied CaI:CdS ratios. (a) A comparison of QE_{ET} vs. the CaI:CdS molar ratio for CdS NR samples α and β. (b) The ET rate vs. the CaI:CdS molar ratio; the points are fit to a line with the slope equal to $\bar{k}_{ET}$ (ET rate = $\bar{k}_{ET}$ * (CaI:CdS)), revealing the value of $\bar{k}_{ET}$, as described in the text. (c) The inverse of the QE_{ET} vs. the inverse of CaI:CdS. A linear fit to Eq. 3.9 reveals the value of $\bar{k}_{CdS}$ /$\bar{k}_{ET}$. Adapted with permission from *J. Am. Chem. Soc*., 2014, **136**, 4316-4324. © Copyright 2014 American Chemical Society.

Table 3.4 Results of analysis of the TA kinetics of complexes of CdS α with CaI. Results are displayed in Figure 3.10a. Each kinetic trace was fit with Eq 3.5.

Sample	ratio	$\bar{\tau}$ (ns)	$\bar{k}$ (s^{-1})	QE_{ET}	$rate_{ET}$ (s^{-1})
CdS α	n/a	84	2.3×10^7	n/a	n/a
CaI:CdS	0.15:1	83	2.5×10^7	9.6%	2.4×10^6
CaI:CdS	0.29:1	72	2.8×10^7	19%	5.4×10^6
CaI:CdS	0.56:1	68	3.1×10^7	26%	7.8×10^6
CaI:CdS	1.25:1	70	3.5×10^7	34%	1.2×10^7
CaI:CdS	1.70:1	54	4.2×10^7	46%	2.0×10^7

Table 3.5 Results of analysis of the TA kinetics of complexes of CdS β with CaI. Results are displayed in Figure 3.10b. Each kinetic trace was fit with Eq 3.5.

Sample	ratio	$\bar{\tau}$ (ns)	$\bar{k}$ (s^{-1})	QE_{ET}	$rate_{ET}$ (s^{-1})
CdS β	n/a	123	2.1×10^7	n/a	n/a
CaI:CdS	0.9:1	93	3.8×10^7	43%	1.6×10^7
CaI:CdS	1.8:1	63	5.5×10^7	61%	3.3×10^7
CaI:CdS	2.7:1	61	6.0×10^7	65%	3.9×10^7
CaI:CdS	3.8:1	53	7.3×10^7	71%	5.2×10^7
CaI:CdS	4.5:1	47	7.7×10^7	72%	5.6×10^7
CaI:CdS	5.7:1	40	9.4×10^7	77%	7.2×10^7

3.3.4 TA kinetics in CdS NR complexes with inactivated CaI

To examine the relationship between the H-cluster properties and the CdS→CaI ET behavior, we measured the ET kinetics between CdS NRs and CaI variants that were not catalytically active due to modifications at the H-cluster. The first variant was an immature form

of CaI (CaI^{Im}), which by analogy to an immature form of HydA1 from *Chlamydomonas reinhardtii* prepared from similar expression conditions[121,122] is thought to lack the $2Fe_H$ subsite of the H-cluster. The second variant was the active CaI treated with carbon monoxide (CaI^{CO}). CO treatment has been shown to reversibly inhibit hydrogenase activity.[134,135] For both variants, the accessory F-clusters remain intact. For CaI^{Im}, H-cluster biosynthesis is impeded by the absence of maturase factors, but synthesis of the accessory F-clusters is not believed to be affected since they are targets of the basic FeS cluster biosynthetic machinery.[61] The presence of the F-clusters was confirmed by Fe analysis of Ca^{Im}. For CaI^{CO}, CO binding has been demonstrated to occur at the $2Fe_H$ subsite of the H-cluster,[136,137] and further studies on [NiFe]-hydrogenases demonstrated that CO binding does not perturb the redox potential of the F-clusters.[138] Both CaI^{Im} and CaI^{CO} therefore are excellent candidates to examine the role of the H-cluster in ET kinetics.

In Figure 3.12, we compare the TA band gap signal decay kinetics for CdS NRs (sample α), CdS-CaI, and CdS-CaI^{Im} complexes (both mixed in a 1:1 molar ratio). The average electron lifetime $\bar{\tau}$ of CdS-CaI^{Im} (82 ns) is longer than that of CdS-CaI (63 ns), but still clearly shorter than that of CdS NRs without any form of CaI ($\bar{\tau}$ = 96 ns). The resulting $\bar{k}_{ET}$ in CdS-CaI^{Im} is 8.6×10^6 s^{-1} with a QE_{ET} of 29% (Table 3.6). This data demonstrates that CaI^{Im} is capable of accepting electrons from CdS NRs.

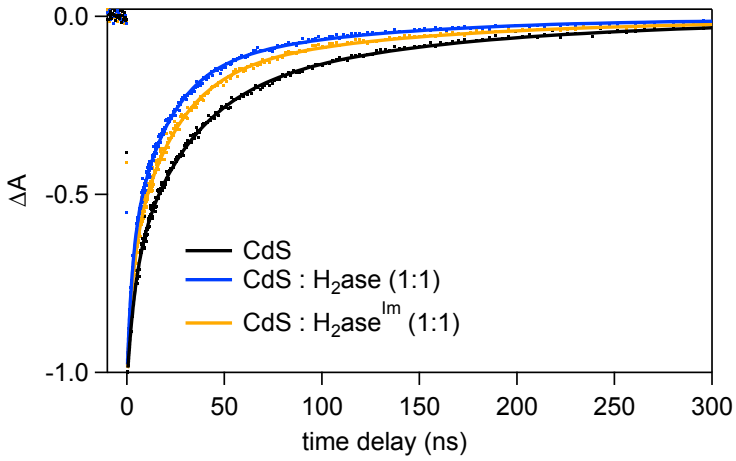

Figure 3.12 CdS band gap bleach decay kinetics for CdS NRs (black), CdS-CaI (blue), and CdS-CaI^{Im} complexes (orange). Even though it lacks the $2Fe_H$ subsite of the H-cluster, CaI^{Im} can accept electrons from CdS. Adapted with permission from *J. Am. Chem. Soc.*, 2014, **136**, 4316-4324. © Copyright 2014 American Chemical Society.

There may be subtle structural differences between CaI with a fully-assembled H-cluster and CaI^{Im} that result in slightly different ET rates and efficiencies. To minimize the number of variables in the comparison between active and inactive CaI, we performed TA experiments on the inhibited CdS-CaI^{CO} (Figure 3.13). We verified that CO incubation inactivated CaI by carrying out photochemical H_2 production experiments on CO-incubated and Ar-incubated CdS-CaI complexes. Unlike the CdS-CaI complexes under Ar, CdS-CaI^{CO} did not produce a detectable amount of H_2. The results of TA experiments on CdS NRs, CdS-CaI incubated under Ar (active), and CdS-CaI^{CO} (inactive) are shown in Figure 3.13. CO incubation has no effect on the TA signal of CdS NRs alone (Figure 3.14). Remarkably, the decay trace of CdS-CaI^{CO} is also almost identical to that of CdS-CaI. In Figure 4b, for CdS-CaI^{CO}, $\bar{k}_{ET}$is 1.7×10^7 s^{-1} and QE_{ET} is 44% (for CdS-CaI, $\bar{k}_{ET}$ is 1.8×10^7 s^{-1} and QE_{ET} is 44%).

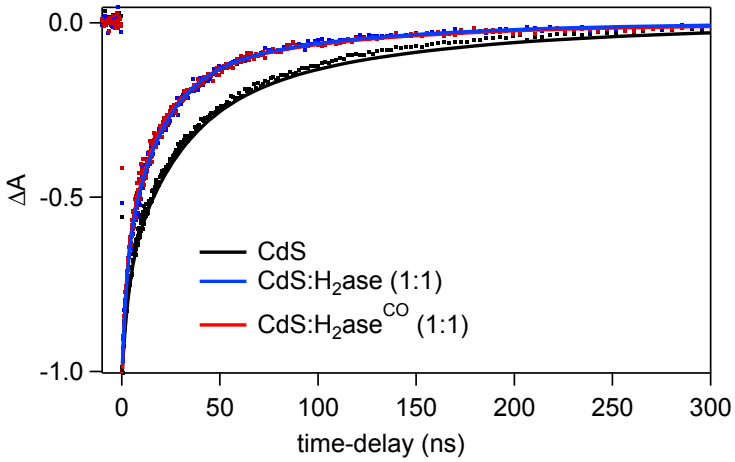

Figure 3.13 CdS band gap bleach decay kinetics for CdS NRs (black), CdS-CaI in an Ar atmosphere (blue), and CdS-CaI^{CO} complexes prepared in a CO atmosphere that inactivates the H-cluster (red). CO deactivation does not change the kinetics of ET. Adapted with permission from *J. Am. Chem. Soc.*, 2014, **136**, 4316-4324. © Copyright 2014 American Chemical Society.

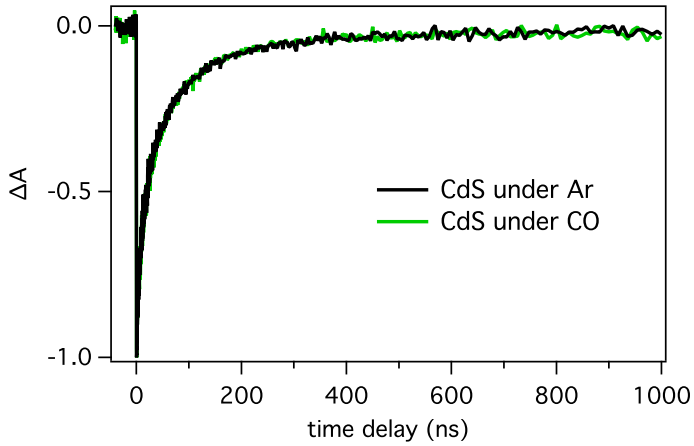

Figure 3.14 TA band gap kinetics of CdS α NRs under atmospheres of 100% argon and 100% carbon monoxide. Adapted with permission from *J. Am. Chem. Soc.*, 2014, **136**, 4316-4324. © Copyright 2014 American Chemical Society.

Table 3.6 Fitting parameters and resulting kinetic parameters for data shown in Figure 3.12 and Figure 3.13. Each kinetic trace was fit to Eq 3.5.

Sample	fit parameters		$\bar{\tau}$ (ns)	$\bar{k}$ (s^{-1})	QE_{ET}	$\bar{k}_{ET}$ (s^{-1})
CdS	$a_0 = -0.26$ $a_1 = -0.49$ $a_2 = -0.25$	$\tau_0 = 4.09$ ns $\tau_1 = 28.6$ ns $\tau_2 = 129$ ns	96	2.1×10^7	n/a	n/a
CaI:CdS (1:1)	$a_0 = -0.31$ $a_1 = -0.52$ $a_2 = -0.17$	$\tau_0 = 2.45$ ns $\tau_1 = 18.2$ ns $\tau_2 = 93.3$ ns	63	3.8×10^7	44%	1.7×10^7
CaI^{Im}:CdS (1:1)	$a_0 = -0.29$ $a_1 = -0.54$ $a_2 = -0.17$	$\tau_0 = 2.82$ ns $\tau_1 = 22.1$ ns $\tau_2 = 119$ ns	82	3.0×10^7	29%	8.6×10^6
CdS	$a_0 = -0.26$ $a_1 = -0.48$ $a_2 = -0.26$	$\tau_0 = 3.37$ ns $\tau_1 = 26.7$ ns $\tau_2 = 119$ ns	91	2.2×10^7	n/a	n/a
CaI:CdS (1:1)	$a_0 = -0.27$ $a_1 = -0.52$ $a_2 = -0.21$	$\tau_0 = 2.05$ ns $\tau_1 = 16.1$ ns $\tau_2 = 78.1$ ns	56	4.0×10^7	44%	1.8×10^7
CaI^{CO} CdS (1:1)	$a_0 = -0.30$ $a_1 = -0.52$ $a_2 = -0.18$	$\tau_0 = 2.12$ ns $\tau_1 = 17.2$ ns $\tau_2 = 89.4$ ns	61	4.0×10^7	44%	1.7×10^7

3.4 Discussion

3.4.1 Competition between ET and electron relaxation in CdS-CaI complexes

Our measurements of electron decay kinetics in CdS NRs and CdS-CaI complexes reveal that the electron relaxation in CdS by radiative and nonradiative recombination and ET from CdS to CaI occur with very similar rates, with both $\bar{k}_{CdS}$ and $\bar{k}_{ET} \approx 10^7$ s^{-1}. Thus the two processes are in direct kinetic competition and occur with similar probabilities. This results in a QE_{ET} of 42%, meaning that only 42% of photoexcited electrons are available for H_2 generation. According to Eq 3.6, to increase QE_{ET}, it would be necessary to either increase $\bar{k}_{ET}$ or decrease $\bar{k}_{CdS}$. When we account for a Poisson distribution of CaI adsorbed onto CdS NRs, when mixed at a 1:1 molar

ratio, we assume 63% of the CdS NRs in solution have at least one CaI moiety adsorbed to the surface. Therefore the upper limit for QE_{ET} for a 1:1: CdS NR:CaI sample is 63%. A 10-fold increase in $\bar{k}_{ET}/\bar{k}_{CdS}$ would be sufficient to increase the QE_{ET} from 42% to near the maximum QE_{ET} value of 63%. Given the remarkable tunability of the electronic and surface structure of semiconductor nanocrystals, it is entirely feasible that the value of $\bar{k}_{ET}/\bar{k}_{CdS}$ could be changed dramatically through rational structural modifications. For example, in nanocrystal-based electron transfer systems where ET occurred through molecular linkers/surface-capping ligands, gains in ET rate were achieved by decreasing the length of surface-capping ligands.[139,140] Alternatively, using nanocrystals with longer excited state lifetimes could lead to a higher value of $\bar{k}_{ET}/\bar{k}_{CdS}$. It has been shown that band engineering can be used to achieve long-lived excited states in nanocrystals by formation of charge-separating type-II interfaces.[22,141,142]

We found that the rate of ET and the value of QE_{ET} from CdS NRs to CaI moieties increased when the value of molar ratio of CaI and CdS NRs increased from <1:1 up to several CaI molecules per NR (Figure 3.10). The linear increase of ET rate with increasing CaI:CdS ratio and a good fit to Eq 6 (Figure 3.11b) demonstrate that the CaI moieties act as independent electron acceptors in this low surface coverage regime. The increase in ET rate is a result of the single, delocalized photoexcited electron localizing in a CaI moiety more quickly when there are multiple electron acceptors available. Because the values of $\bar{k}_{CdS}$ and $\bar{k}_{ET}$ are similar, the gains in QE_{ET} with increasing CaI:CdS ratio are, relatively speaking, not very significant. For example, to double QE_{ET} from 42% to 84%, the CaI:CdS molar ratio would need to increase from 1:1 to 6.3:1. In this scenario, twice as many electrons removed from CdS would be divided among 6 times as many CaI moieties, effectively reducing the value of QE_{ET} per CaI from 42%

(1:1) to 13% (6.3:1). Increasing CaI:CdS should therefore have a detrimental effect on the quantum yield of H_2 ($QY(H_2)$). Even though a higher fraction of electrons are harvested from the photoexcited CdS NRs, the probability of transferring two electrons to the same CaI moiety would decrease. This effect is particularly important if photoexcitation rates are relatively low, allowing the first electron required to produce H_2, bound at the H-cluster, to decay before the second electron arrives. Indeed, the amount of H_2 produced by CdS-CaI complexes decreased with increasing CaI:CdS molar ratios above 1:1 and that the amount of H_2 produced scaled linearly with the population of 1:1 complexes in the sample (Figure 3.15 and Figure 3.16).[12] Our measurements of ET kinetics demonstrate that the detrimental effect of increasing the value of CaI:CdS is ultimately a consequence of the similarity of the $\bar{k}_{\mathrm{CdS}}$ and $\bar{k}_{\mathrm{ET}}$ values. Examination of Equations 5 and 6 reveals that an increase in the number of CaI moieties per CdS NR would be beneficial for H_2 production if ET were significantly slower than electron decay in the nanocrystal. For example, if the value of $\bar{k}_{\mathrm{ET}}/\bar{k}_{\mathrm{CdS}}$ were 0.1, QE_{ET} would be 9% at a molar ratio of 1:1, and 18% at a molar ratio of 2:1. This would result in no change in the number of electrons transferred per CaI moiety, and doubling the CaI:CdS ratio would be beneficial to $QY(H_2)$. For similar reasons, we predict that the optimal value of $QY(H_2)$ would be reached at low CaI:CdS ratios if ET were much faster than electron decay in the NRs.

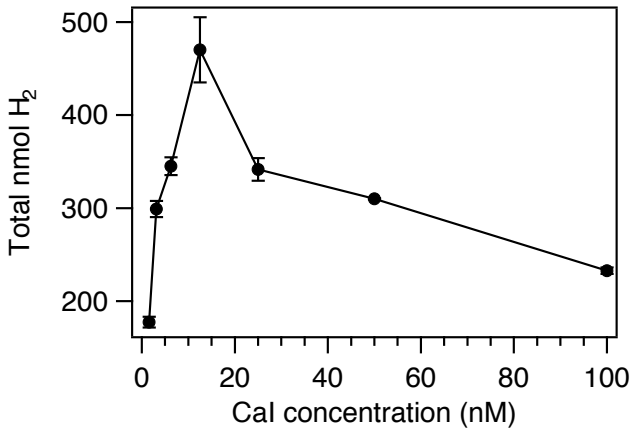

Figure 3.15 Effect of complex molar ratio of photocatalytic H_2 production by CdS:CaI. Mixtures prepared with a fixed CdS concentration of 19 nM and CaI concentrations between 1.58 to 100 nM to give molar ratios of 1:5, 1:2.5, 1:1.33, 1:0.67, 1:0.33, 1:0.167, and 1:0.083 CdS:CaI solutions. Samples were illuminated for 10 min with a 405 nm LED at 800 μE m^{-2} s^{-1}. Adapted with permission from *J. Am. Chem. Soc.*, 2012, **134**, 5627-5636. © Copyright 2012 American Chemical Society.

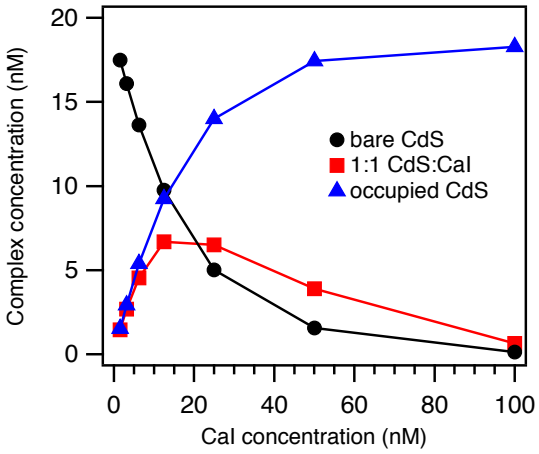

Figure 3.16 Statistical analysis of photocatalytic H_2 production by CdS:CaI complexes. Concentrations of specific molecular complexes within each solution of CdS:CaI. Concentrations are calculated using the Poisson distribution to determine the fraction of 19 nM CdS with a specific CaI coverage for the molar ratios of 1:5 (100 nM CaI), 1:2.5 (50 nM CaI), 1:1.33 (25 nM CaI), 1:0.67 (12.5 nM CaI), 1:0.33 (6.25 nM CaI), 1:0.167(3.13 nM CaI), and 1:0.083 CdS:CaI (1.56 nM CaI). Bare CdS (black circles) has no CaI adsorbed, 1:1 CdS:CaI (red squares) has one CaI adsorbed per CdS NR, and total occupied CdS (blue triangles) is the sum of all CdS with ≤1 CaI adsorbed per CdS. Adapted with permission from *J. Am. Chem. Soc.*, 2012, **134**, 5627-5636. © Copyright 2012 American Chemical Society.

3.4.2 Electron pathways in H_2 production

Our measurements of ET dynamics in complexes of CdS NRs with catalytically inactive CaI allow us to assemble a more detailed picture of the pathway that electrons transferred from CdS NRs undergo to eventually form the H-H bond. We have previously shown that CdS-CaI complexes form via a biomimetic interaction between the negatively-charged surface of CdS NRs capped with 3-MPA and the positively-charged surface on the CaI moiety.[12] The closest iron-sulfur cluster to that surface is the distal [4Fe-4S] cluster.[115,143] Thus, we hypothesized that the photochemical H_2 production in CdS-CaI complexes occurs via electron injection at the distal F-cluster and electron transport to the H-cluster, in analogy to *in vivo* Fd-mediated H_2 production.[12] Within this model, provided that inactivation of the H-cluster does not change the secondary structure of CaI or the locations and electronic properties of the accessory iron-sulfur clusters, the value of k_{ET} should be governed by the structure and electronic properties in the vicinity of the distal F-cluster, and not depend strongly on the properties of the H-cluster. The TA kinetic data showed that interfacial ET between CdS and CaI was unaffected by CO binding, even though CO binding causes a ~50 mV increase in the midpoint potential of the H-cluster (Figure 3.13).[144] Furthermore, ET proceeds in the absence of the $2Fe_H$ subsite of the H-cluster (Figure 3.12), demonstrating that an intact H-cluster is not necessary for interfacial ET. These experiments provide strong evidence for our hypothesis that photochemical H_2 production involves transport through biomimetic pathways in CdS-CaI complexes. Since the ET does not occur preferentially to catalytically active CaI, but occurs with equal probability to any CaI, our data implies that the overall QY(H_2) includes losses due to ET to inactive CaI that may be present in the sample.[63] We note that TA measurements are uniquely suited to detect the

nanosecond electron injection from CdS to CaI in both catalytically active and inactive complexes. Despite the similar midpoint potentials of the F- and H-clusters (–420 and –400 mV, respectively),[144] TA experiments allow us to decouple the observation of electron injection from catalysis.

Figure 3.17 illustrates the complicated pathways that electrons photoexcited in CdS take to H_2. In previous H_2 production experiments with CdS-CaI complexes, the amount of H_2 generated increased linearly with photon flux, indicating that the reaction was photon-limited and the inherent catalytic turnover rate (k_{cat}) was not reached.[12] Under photon-limited conditions, the efficiency with which photoexcited electrons can be transferred from CdS to CaI (QE_{ET}) is a critical parameter in determining k_{cat}. QE_{ET} in turn depends on k_{ET}/k_{CdS}, as described above. Once an electron has been injected into CaI, it is transported to the active site with the rate constant $k_{transport}$. If all the electrons transferred from CdS to CaI were utilized in catalysis, the values of QE_{ET} and $QY(H_2)$ would be equal. The definition of $QY(H_2)$ takes into account that two electrons are required for each H_2 molecule. In CdS-CaI complexes, $QY(H_2)$ is 2 times lower than QE_{ET}, suggesting that there are additional factors that limit the H_2 production rate. One possible cause is the distribution of the number of CaI moieties per CdS NR,[12] including the presence of complexes with ratios greater than 1:1, in which competition for electrons between CaI moieties on the same NR decreases H_2 production efficiency. Another possibility is ET to catalytically inactive CaI that may be present in the sample,[63] as evidenced by the ability of inactive variants of CaI to accept electrons from CdS NRs. Additional candidates for rate-limiting processes include: back-ET, which is the predominant pathway for some [FeFe]-hydrogenases at higher pH

values;[145,146] electron and proton transport steps within CaI;[146-148] covalent bond formation;[110,149] and efficiency of the hole scavenging.[71,150]

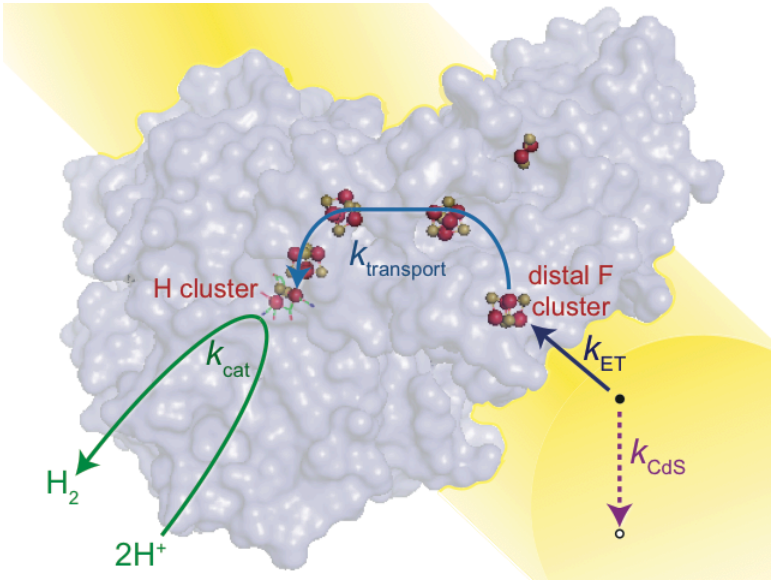

Figure 3.17 Schematic of the electron pathway resulting in H_2 generation by photoexcited CdS-CaI complexes. The enzyme surface is shown in blue with the Fe and S atoms in the [FeS] clusters shown as red and yellow spheres, respectively. Enzyme coordinates are from CpI (PDB ID: 3C8Y), which has high primary sequence homology and high similarity with CaI. The CdS NR surface is shown in yellow. The rate of internal electron decay in CdS is denoted by k_{CdS}, the rate of electron injection from CdS to CaI by k_{ET}, the rate of electron transport through CaI to the H-cluster by $k_{transport}$, and the rate of H_2 production by k_{cat}. Adapted with permission from *J. Am. Chem. Soc.*, 2014, **136**, 4316-4324. © Copyright 2014 American Chemical Society.

3.4.3 The value of k_{ET} in CdS-CaI complexes

The value of $\bar{k}_{ET}$ we measured for electron injection from CdS NRs to CaI ($\approx 10^7$ s^{-1}) is in contrast to much faster ET from nanocrystals to molecules or metal particles adsorbed directly on the nanocrystal surface, usually observed to be in the 10^9-10^{12} s^{-1} range.[2] To understand why the

ET rate between CdS NRs and CaI is relatively slow, we consider the charge transfer interface (Figure 3.17). Because a crystal structure of CaI has not yet been obtained, we use the structure of [FeFe]-hydrogenase I from *Clostridium pasteurianum* (CpI) (PDB ID: 3C8Y) as an analog.[143] CpI has 82% similarity with CaI and all 22 cysteine residues in CpI are conserved in CaI, suggesting similar binding and location of the iron-sulfur clusters.[151] The distal F-cluster is 4 Å away from the positive outer surface of the protein. However, due to the surface curvature of the Fd-binding pocket of the enzyme, the closest point of contact between CaI and CdS may be up to 8 Å away from the distal F-cluster. Additionally, electrons may tunnel through the ~ 5 Å long NR-surface-capping ligand (3-MPA) to reach CaI. In redox enzymes, relatively slow ET rates are common because of electron tunneling over long distances.[152,153] An ET rate constant of $\approx 10^7$ s^{-1} is consistent with the considerable tunneling distance between CdS and the distal F-cluster. The value of k_{ET} may be increased by modifying the structure and electronic properties of the nanocrystals, including the surface-capping ligands.

Considering that electron injection from CdS into the distal F-cluster of CaI is followed by electron transport via the redox chain of iron-sulfur clusters, an increase in k_{ET} is in principle only beneficial until k_{ET} matches $k_{transport}$. Any further increase would result in a kinetic bottleneck inside CaI, rather than at the CdS-CaI interface, and possibly even back-ET from iron-sulfur clusters close to the CdS-CaI interface. We can estimate the maximum value of $k_{transport}$ through the iron-sulfur clusters in CaI by applying the Moser-Dutton model of electron transfer in proteins, which estimates the electron tunneling constant (β) to be 1.4 $Å^{-1}$ for tunneling through the protein medium between redox centers.[152,154] In this Marcus-theory based model, rates of ET between cofactors in a redox transport chain depend exponentially on tunneling distances,

driving force for ET (ΔG_{ET}), and reorganization energy (λ). Without detailed knowledge of ΔG_{ET} and λ, we can determine the maximum rate of electron transport ($k_{transport, MAX}$), which occurs when $-\Delta G_{ET} = \lambda$. $k_{transport, MAX}$ depends only on internuclear cluster-to-cluster distances (R).[155] The rate for electron transport through CaI from the distal [4Fe-4S] F-cluster to the H-cluster was estimated from a series of ET steps between iron-sulfur clusters. Rate constants (k_{ET}) were calculated individually for each of the ET steps: from the distal → medial F-cluster (distance = 8.3 Å); medial → proximal F-cluster (distance = 9.5 Å); proximal F-cluster → H-subcluster $[4Fe\text{-}4S]_H$ (distance = 7.8 Å); and $[4Fe\text{-}4S]_H \rightarrow 2Fe_H$ (distance = 3.4 Å).[143] If we set $\Delta G = -\lambda$ for ET between each set of donor and acceptor redox centers, then we can calculate the maximum rate of electron tunneling for each step according to Eq 3.10:[155]

$$\log_{10} k_{ET,MAX} = 13 - 0.6(R - 3.6) \qquad \text{(Equation 3.10)}$$

The value of $k_{transport,MAX}$ was determined from the $k_{ET,MAX}$ values for each step as follows:

$$\sum_i \frac{1}{(k_{ET,MAX})_i} = \frac{1}{k_{transport,MAX}} \quad . \qquad \text{(Equation 3.11)}$$

The resulting value of $k_{transport, MAX}$ calculated using Eq 3.10 and 3.11 is 2.2 x 10^9 s^{-1}. This means that in an effort to increase the value of k_{ET} in order to increase the efficiency of H_2 production, it is not necessary to aim for values as high as those obtained in nanocrystal-molecule complexes. Increasing the k_{ET} value to 10^9 s^{-1} would lead to QE_{ET} of 99% if the value of k_{CdS} remained unchanged, and values of k_{ET} above 10^9 s^{-1} are not likely to be beneficial.

3.4.4 Comparison of CdS-CaI with CdS-Pt Nanoheterostructures

We now contrast the charge transfer behavior of CdS-CaI complexes with that of previously-reported CdS-Pt nanoheterostructures, which also photochemically produce H_2.[5,25,28] In such structures, Pt nanoparticles are grown directly on the surfaces of CdS NRs that are

synthesized by methods comparable to those used for the CdS NRs in our experiments. To produce H_2, photoexcitation of CdS is followed by ET to Pt, which catalyzes H^+ reduction, while hole scavenging is carried out by molecular electron donors.[5,25,71] ET from CdS to Pt is very fast, with $k_{ET} > 10^{11}$ s^{-1}, and essentially 100% efficient.[3,72,95] Thus, the fraction of photoexcited electrons available for reduction is higher in CdS-Pt than in CdS-CaI structures. Yet, the reported QY(H_2) values for CdS-Pt[5,25] (1-4%) are lower than the 20% we reported for CdS-CaI.[12] In Pt-based structures, QY(H_2) increased to 20% when CdSe/CdS core/shell NRs were employed. Such structures promote spatial separation of photoexcited electrons in Pt and holes localized in CdSe cores.[5]

Based on the intricate kinetics involved in H_2 generation in the CdS-CaI system, we can speculate on the reason why the CdS-CaI system exhibits a higher value of QY(H_2) than the CdS-Pt system, despite a much slower and less efficient ET. Because the rate of excitation of CdS NRs during H_2 generation is low (~10^3 s^{-1})[12] and two electrons are required for each H_2 molecule, it is important for the singly-reduced catalytic state to be stable for a relatively long period of time. In CaI, following injection at the distal F-cluster, the first electron is transported over 29 Å through a sequence of electron transfer steps to the active site (H-cluster),[143] where it is captured in a chemically-bonded hydride intermediate.[117-119] Considering the large distance over which charge separation occurs, the multi-step nature of electron transport, and the relative stability of the hydride, it is very likely that back-ET is quite slow. On the other hand, the first electron used for catalysis in the CdS-Pt structures is spatially closer to the nanocrystal-catalyst interface and is potentially more likely to recombine with a hole in the nanocrystal by back-ET.[5,23] These differences may explain why the CaI-based system produces more H_2 with fewer

transferred electrons than the Pt-based system. The comparison of ET kinetics and H_2 production CdS-Pt and CdS-CaI systems illustrates that high QE_{ET} from the nanocrystal to the catalyst does not guarantee high values of $QY(H_2)$, and that the intricacies of the catalytic mechanism need to be considered in the analysis of the photochemical activity of nanocrystal-based hybrids.

3.5 Conclusions

We have examined the kinetics of electron transfer (ET) between light-absorbing CdS nanorods (NRs) and the redox enzyme [FeFe]-hydrogenase I from *Clostridium acetobutylicum* (CaI). The ET process is essential for photochemical generation of H_2 mediated by these complexes, and its efficiency defines the upper limit for the quantum yield of H_2 production. We used transient absorption (TA) spectroscopy to measure the rates and efficiencies of ET from CdS to CaI. The ET rate constant was similar to the rate constant for the decay of photoexcited electrons in CdS NRs (both 10^7 s^{-1}), resulting in 42% efficient ET in complexes with the average CdS:CaI ratio of 1:1. The efficiency of ET could be improved in the future by a combination of increased ET rate and decreased rate of electron decay in the nanocrystal. Both goals may be achievable through structural modification of nanocrystals. Increasing the average number of CaI moieties per CdS NR resulted in competition for electrons. This ultimately leads to decreased H_2 production efficiency. The ET behavior in catalytically inactive CdS-CaI^{Im} and CdS-CaI^{CO} was similar to that in active CdS-CaI complexes, demonstrating that electron injection occurred into a distal F-cluster of CaI in a manner analogous to the natural function of CaI. These insights into the kinetics of electron injection from CdS NRs to CaI allow us to begin to assemble a picture of

the complex electron pathways involved in photochemical H_2 generation and to understand how the rates of sequential steps along the path determine the overall efficiency of the process.

Chapter 4 Relationship between surface ligand length, electron transfer, and hydrogen production in CdS nanorod- [FeFe]-hydrogenase complexes

4.1 Introduction

Coupling semiconducting materials with hydrogenases is an emerging strategy to photochemically drive H_2 production.[6,12,37,39,41,55,156] Specifically, significant progress has been made with nanocrystal-enzyme hybrid structures, which integrate the tunable electronic structure, strong light absorption, and tunable surface chemistry of nanocrystals with the catalytic selectivity of enzymes. Photochemical reactions of nanocrystal-enzyme complexes proceed through a sequence of steps: light absorption in the nanocrystals, transfer of photoexcited electrons to the enzyme where they participate in catalysis, and scavenging of photoexcited holes by sacrificial electron donors.[6,41,150] We demonstrated that complexes of CdS nanorods (NRs) and [FeFe]-hydrogenase from *Clostridium acetobutylicum* (CaI) generate H_2 under illumination, with quantum yields ($QY(H_2)$) of up to 20% at a CaI:CdS NR molar ratio of ~1:1.[12] $QY(H_2)$ is defined as (H_2 molecules produced/photons absorbed)*(2 electrons/H_2 molecule).[12]

The kinetics of electron transfer (ET) from the nanocrystal to the enzyme play a crucial role in the overall photochemical reactivity. The quantum efficiency of ET (QE_{ET}) determines the upper limit on the quantum yield of H_2 generation. QE_{ET}, in turn, depends on how the rate of ET compares to the rates of competing excited state decay processes in the nanocrystal. The results in Chapter 3 detailed the measurements of electron decay kinetics in complexes of CdS

NRs with CaI, which photochemically reduces $2H^+$ to H_2.[41] Transient absorption (TA) spectra indicated that ET occurs on a similar timescale as the excited state decay of NRs.[41]

The CdS-CaI complexes form via a biomimetic interaction in which CdS NRs, capped with negatively-charged surface ligands, bind to CaI as analogs of the electron-donating protein ferredoxin.[6,12] Since the biomimetic CdS NR-CaI interaction is mediated by the nanocrystal surface ligands, we hypothesize that the mercaptocarboxylate ligands act as a medium through which electrons are transferred. We are interested in investigating the effects of changing the length of the alkane chain in the ligand molecules. Prior studies of nanocrystal-based electron donor-acceptor systems (CdS-TiO_2) with thiol-terminated molecules forming a bridge between the donor and acceptor, have shown that bridge imposes a tunneling barrier for electron transfer.[157] The ET rate from donor to acceptor is expected to decrease exponentially with both barrier height and bridge length.[158] Previous studies have demonstrated that the nature of the molecular bridge affects the ET process between noncontact electron donors and acceptors.[139,140,159,160]

Protein film voltammetry and electrochemical scanning tunneling microscopy (EC-STM) can measure catalytic turnover rates of enzymes attached to an electrode using the biased electrode as an electron source.[51] These techniques were used to measure the turnover from CaI immobilized onto a self-assembled monolayer of mercaptocarboxylates with varying lengths of aliphatic chain on an Au electrode.[63] The electrochemical study indicated an electronic decay constant (β) of 0.82 $Å^{-1}$ for ET from the electrode to CaI through mercaptocarboxylate molecules.

This chapter outlines our efforts to monitor the photochemical efficiency and photoexcited charge transfer from colloidal CdS NR to CaI through a sequence of lengths of mercaptocarboxylate ligands. We report an exponential decrease in H_2 production as the length of the nanocrystal surface ligand is increased. To understand the factors that contribute to this trend in H_2 production, we measured the dynamics of the photoexcited electrons in CdS NRs with and without CaI using TA spectroscopy. Each sample of CdS NRs with a different length ligand exhibits unique kinetics of the excited state electron decay. Since the rate of electron-hole recombination is intrinsic to the CdS NRs, the differences in the kinetics after ligand exchange are attributed to electron trapping at the nanocrystal surfaces. The research progress to date indicates that the excited state dynamics of CdS NRs and of CdS-CaI complexes at a 1:1 molar ratio are very similar when the surface ligands contain an alkane chain with greater than three carbons because the QE_{ET} is small and therefore the ET is difficult to detect. Future experiments will measure the rate constants for ET in CdS-CaI complexes with longer nanocrystal surface ligands.

4.2 Experimental

4.2.1 Sample Preparation

4.2.1.1 CdS Nanorods

The CdS NRs synthesis was adapted from a published procedure for a seeded-growth procedure.[161] CdS seeds were synthesized from an initial mixture of 0.100 g cadmium oxide (CdO), 0.603 g octadecylphosphonic acid (ODPA), and 3.299 g trioctylphosphine oxide (TOPO),

which were degassed under vacuum for 1 hour then heated to 300 ºC under Ar for 30 minutes to dissolve the CdO, causing it to turn optically clear and colorless. The solution was cooled to 120ºC, degassed for 30 minutes, then heated to 320ºC under Ar. After the temperature stabilized, sulfur stock solution (0.179 g hexamethyldisilathiane ($(TMS)_2S$) in 3 g of tributylphosphine (TBP)) was quickly injected. The temperature controller was then set to 250ºC and the nanocrystals are allowed to grow for 7.5 minutes. The reaction was stopped by removing the heating mantle and injecting 4 mL of anhydrous toluene. The CdS seeds were precipitated out by the addition of methanol followed by centrifugation. After transfer to the glovebox and washing with toluene/methanol (2x), the final product was dissolved in trioctylphosphine (TOP). The CdS seeds have an exciton peak at 408 nm. To synthesize the rods, 0.086 g CdO, 3 g TOPO, 0.290 g ODPA, and 0.080 g hexylphosphonic acid (HPA) were degassed under vacuum at 120ºC. The solution was heated to 350ºC under Ar for 30 minutes then 1.5 mL of TOP was injected into the solution. When the temperature of the Cd-containing solution stabilized at 350 °C, the seed-containing sulfur injection solution (0.124 g of sulfur (S) in 1.5 mL of TOP mixed with 8×10^{-8} mol CdS QD seeds) was quickly injected. The solution grew for 8 min. The particles were cooled, transferred to the glovebox, and cleaned with toluene/ethanol washes.

The resulting NRs had an average diameter of 3.7 ± 0.3 nm and an average length of 22.6 ± 1.8 nm as determined by measurements of 300 particles in TEM images. The molar absorptivity (ε) of the CdS NRs was determined by correlating absorption spectra with Cd^{2+} concentrations determined by elemental analysis (ICP-OES). The estimated value of ε_{350} was 1710 $M^{-1}cm^{-1}$ per Cd^{2+}. The number of Cd^{2+} per NR was estimated from the average NR dimensions. ε_{350} was 8.6 x 10^6 $M^{-1}cm^{-1}$. The hydrophobic surface-capping ligands on the as-

synthesized CdS NRs were replaced with mercaptocarboxylate ligands following the previously reported procedure in Chapter 3 for 3-MPA, and the resulting particles were redispersed in 12.5 mM Tris buffer, pH 7.[5,12,73] Mercaptocarboxylate ligands bind to the NR surface through the deprotonated thiol group, leaving the carboxylate group in solution to enable solubility in water.[85] The ligands put onto the NRs included thioglycolic acid, 3-mercaptopropionic acid, 4-mercaptobutyric acid, 6-mercaptohexanoic acid, 8-mercaptoocanoic acid, and 11-mercaptoundecanoic acid. Particles with each of the mercapotocarboxylate ligands used (number of carbons = 3, 4, 6, 8, 11), were soluble when dispersed into buffer solution.

4.2.1.2 CaI Purification, Characterization, and Coupling to CdS NRs

The [FeFe]-hydrogenase from *Clostridium acetobutylicum* (CaI) was expressed and purified from *Escherichia coli* as previously described in Chapter 3.[120] CaI purification was carried out under anaerobic conditions. In the final Strep-Tactin purification step, CaI was eluted in 50 mM Tris-HCl pH 8.0, 200 mM NaCl, 5% glycerol, and 5 mM sodium dithionite (NaDT). The CaI concentration was determined by Bradford assay (± 10%) using Hemoglobin as the standard.[123] Mixtures of CdS NRs and CaI were prepared in buffer (12.5 mM Tris-HCl, 5mM NaCl, 5% glycerol, pH 7) under an anaerobic Ar environment.

4.2.2 Sample Characterization

4.2.2.1 Steady-state Absorption Spectroscopy

UV-visible absorption spectra were recorded with an Agilent 8453 spectrophotometer equipped with tungsten and deuterium lamps. The samples were sealed in either 0.2 cm or 1 cm quartz cuvettes and spectra were collected at room temperature.

4.2.2.2 Photoluminescence Spectroscopy

Photoluminescence spectra were obtained at room temperature using a Horiba Jobin Yvon Fluorolog-3 Spectrofluorometer with a 450W xenon arc lamp and a R928P Photomultiplier tube. Samples in 1 cm x 1 cm quartz cuvettes were excited at 350 nm and the emission from 365 nm to 685 nm was recorded at 90° relative to the excitation. Emission spectra were corrected for wavelength dependence of the instrument response using a tungsten lamp provided by the manufacturer. CdS NR concentration was 0.18 μM in 12.5 mM Tris-HCl Buffer, pH 7.

4.2.2.3 Transmission Electron Microscopy (TEM)

TEM samples of CdS NRs were prepared by drop casting from solution onto grids and imaged as detailed in Chapter 3.

4.2.2.4 Transient Absorption Spectroscopy

The TA experimental setup was previously described in detail in Chapter 2.[73] The samples were prepared and sealed under Ar in airtight 2 mm quartz cuvettes. The CdS NR sample concentration was 800 nM. The samples containing both NRs and CaI were mixed in 1:1 molar ratios in 12.5 mM Tris-HCl buffer without a sacrificial hole scavenger. The samples were pumped at 401 nm. The pump beam diameter was 240 μm and pulse energy was 10 nJ/pulse. To construct kinetics over the entire delay time window from fs-μs, the ns-timescale, TA signals were scaled to match the fs-timescale results in the overlapping time window. During data collection, the samples were stirred constantly.

4.2.2.5 Light-Driven H_2 Production

Solutions for light-driven H_2 production consisted of 40 nM CdS and 40 nM CaI (1:1 molar ratio) with 100 mM ascorbate as a hole scavenger in 12.5 mM Tris-HCl buffer with 5% glycerol and 5 mM NaCl, pH 7, in 1.5 mL vials sealed with septa. The samples were illuminated with a 405 nm diode laser (Laserglow Technologies) at 12 mW for 10 min. H_2 was detected in the headspace of the vessel using gas chromatography (Agilent Technologies 7820A, molecular sieve 5A column, Ar carrier gas, TCD detector). Turnover frequencies (TOF) for photochemical H_2 production are expressed in units of mol H_2 mol^{-1} CaI s^{-1}.

4.3 Results and Discussion

4.3.1 Characterization of Ligand Exchanged CdS NRs

CdS NRs were prepared with mercaptocarboxylate ligands ranging in lengths from 3-11 carbons in the alkyl chain, with the carboxylate oriented away from the CdS crystal. Exchanging the surface ligands from ODPA to any one of the mercaptocarboxylate ligands causes the band edge absorption to shift 2 nm to the blue but does not alter the shape of the absorption spectrum (Figure 4.1a). The blue shift is a signature of the binding of thiol ligands to the surface, which influences semiconductor electron and hole wave functions.[162] [21,163] The absorption spectra of CdS with each of the mercaptocarboxylate ligands of various lengths are blue-shifted in same manner resulting in almost identical spectra and indicating a successful exchange of the ligands for each sample. The ligand-exchanged particles are soluble in aqueous solutions, which also indicates that the ligands were exchanged.

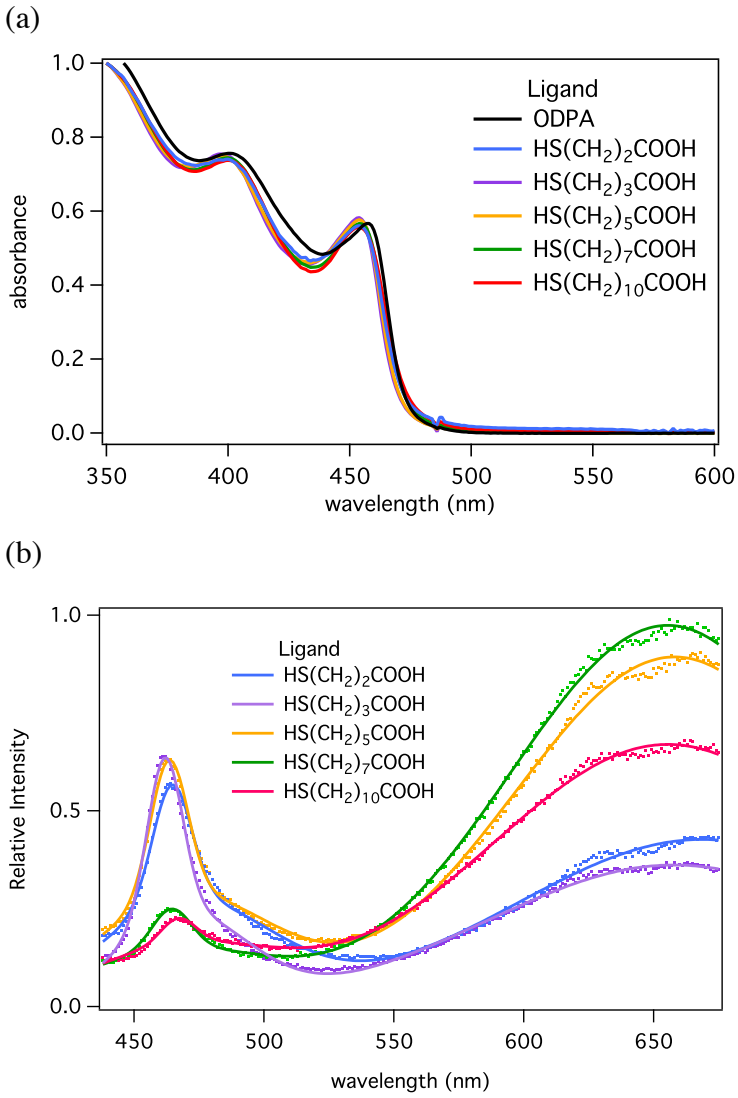

Figure 4.1 (a) Steady-state absorption spectrum of CdS NRs with various surface ligands in buffer and (b) Steady state emission from CdS NRs with various ligands after excitation with 350 nm light. The spectra are fit with three Gaussian peaks, represented by the solid lines.

The steady-state photoluminescence (PL) from photoexcited CdS NRs consists of two distinct emission features, a higher energy peak from band gap emission and a broad, lower energy peak from trap emission.[164] The trap emission has been assigned primarily to the recombination of conduction band (CB) electrons with surface-trapped holes. This assignment is

based on the fact that the CB electron in CdS NRs are long-lived and valence band (VB) holes are trapped at electron-rich centers on the nanocrystal surface.[165] Each of the PL spectra can be fit with three Gaussians (Figure 4.1b). Two Gaussians are necessary to fit the band gap PL and the third, broad Gaussian fits to the trap emission feature.

The CdS NRs used for the experiments in this chapter were synthesized through a different procedure than the NRs used in Chapters 2 and 3. To synthesize the particles used here, first small CdS dots were grown then rods was grown around these dots, whereas the previous rods were grown without being seeded with dots. The synthetic method was changed because a larger yield of CdS NRs was required to assemble samples with every ligand from a single synthesis. Due to the seeded synthetic method for the CdS NRs, some of the NRs have a nonuniform diameter along the rod, with a slightly larger diameter at the location of the seed (Figure 4.2).[166] At a portion of a rod with a larger diameter, quantum confinement is relaxed resulting in a lower energy band gap (X2) than the remainder of the rod (X1), as shown in Figure 4.2. Upon photoexcitation of a CdS NR with a nonuniform diameter, the exciton localizes in the larger diameter portion of the rod. In a heterogeneous CdS NR sample emission is observed over both the X1 and X2 transitions, which results in two emission peaks in the band edge region of the emission spectrum (Figure 4.1b).[166] From the CdS NR PL spectra, we observe that changing the nanocrystal surface ligands causes the PL peaks to change height but the positions and widths are similar from sample to sample (Figure 4.1b). Although the intensity of both band gap and trap emission does vary from sample to sample, there is not a correlation of PL intensity with the length of the surface ligands.

(a)

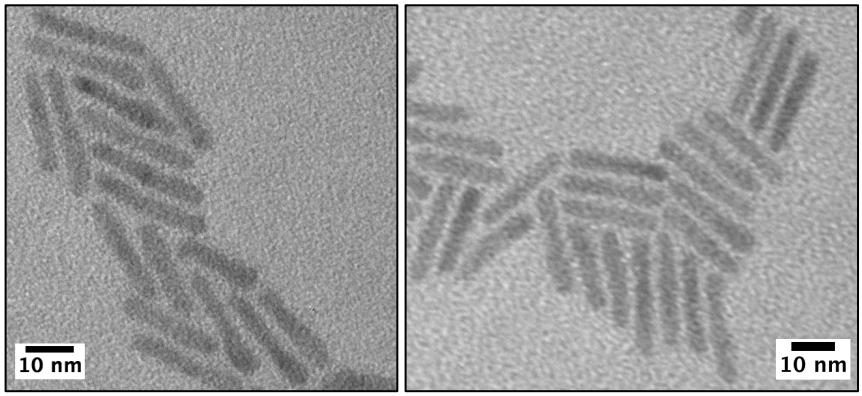

(b)

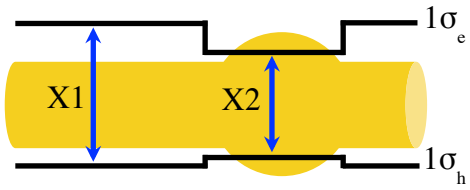

Figure 4.2 (a) TEM image of the seeded CdS NRs used for all experiments in this chapter. (b) A schematic representing a NR of nonuniform diameter and the resulting energy level diagram showing the quantum confined energy levels. X1 and X2 indicate the lowest energy exciton transitions.

4.3.2 H_2 Production using CdS with varied ligand lengths

The negatively-charged functionalized surface of CdS NRs is designed to interact with the large positively-charged region of the protein surface near the distal [4Fe4S] cluster, which receives external electrons.[6] This design of nanocrystal-protein interaction serves to orient the enzyme moieties so that the same face is nearest the nanocrystal in each of the CdS-CaI complexes. Here, we employ nanocrystal ligand molecules having 3-11 carbons in order to alter the distance between the CdS surface and the protein. Upon illumination, hydrogen production from the CdS-CaI complexes was measured by GC (Figure 4.3) and is reported as a turnover

frequency (TOF = moles of H_2/ moles of CaI*s). In Figure 4.3, the error bars indicate the standard deviation from three independent measurements. Using equivalent photoexcitation conditions for each sample, photodriven H_2 production decreases exponentially with increasing ligand length. In Figure 4.3 the TOF is plotted as a function of ligand length and fit to an exponential decay function according to:

$$TOF_d = TOF_{(d=0)} * e^{(-\beta * d)} \qquad \text{(Equation 4.1)}$$

where d is the ligand length and β is the electronic decay constant. The values of TOF are likely underestimated because the calculation uses the number of moles of CaI added to the solution rather than the number adsorbed to CdS NRs. This number also includes inactive protein or enzymes in an orientation unfavorable for ET.

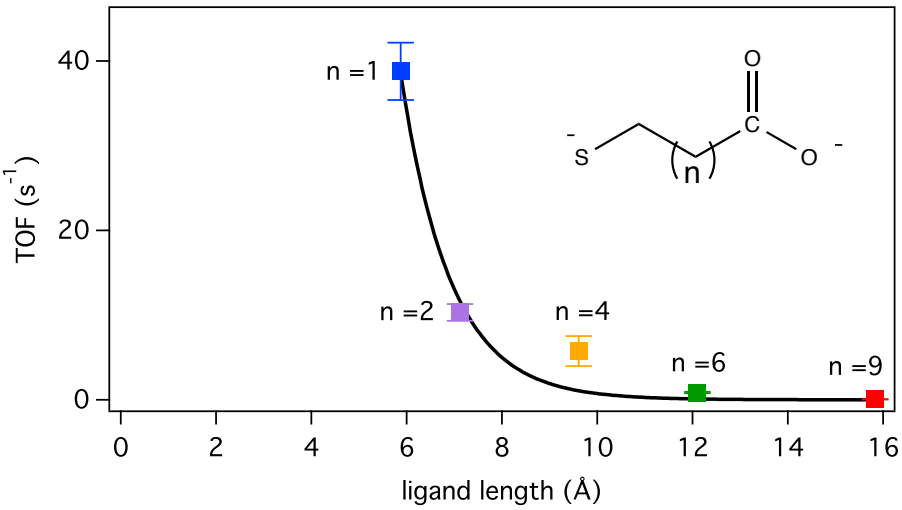

Figure 4.3 Photodriven hydrogen production as a function of ligand length. The solid line is an exponential decay according to Eq 4.1 where β=0.96 $Å^{-1}$.

The trend in photodriven H_2 generation observed through ligands of various lengths suggests that ET from CdS to CaI occurs via tunneling though the nanocrystal-ligand surface-capping ligands. Based on C-C bond lengths of 1.524 Å, C-O^- bond lengths of 1.520 Å, C-S^- bond lengths of 1.817 Å, C-C-C bond angles of 109.5º, C-C-S^- bond angles of 108.3º, and C-C-O^- bond angles of 110.6º, we estimate the distance per carbon in the ligand to be 1.245Å. From this distance, we can calculate the lengths of the ligands and the apparent tunneling distance through which ET may occur. The experimental β constant is 0.96 ± 0.19 $Å^{-1}$, which agrees with literature reports for the characteristic tunneling decay rate for alkanethiols used as molecular bridges between quantum dots and within self-assembled monolayers.[63,159,167-172] The exponential decay behavior of the TOF suggests that the rate of ET has kinetic control over the photocatalytic activity of CdS-CaI complexes. We have previously estimated that electron transport through the CaI moiety from electron injection to the active site is faster than the ET through the ligand layer.[41] Since the electron transport within CaI should be the same for all CdS NR-CaI complexes, independent of the ligand length, we conclude that it does not control the rate of catalysis.

Upon extrapolation of the plot in Figure 4.3 to a distance of zero, the TOF would continue to increase exponentially until the CaI moiety is in direct contact with the nanocrystal surface, where $TOF_{(d=0)}$ ~10,000 s^{-1}. The scenario without ligands is not possible for CdS NR-CaI complexes because they rely on negatively charged surface ligands for solubility, stability, and the electrostatic interaction. The correct choice of shorter ligand is also imperative because small sulfide-containing molecules destroy the active site of hydrogenases.[12,173] When a shorter, 2-carbon (n=0) ligand was used, the photodriven H_2 generation had a TOF that was 6 times lower

than the 3-carbon (n=1) ligand, rather than following the exponential trend shown in Figure 4.3. We attributed this result to poisoning of the CaI active site from ligands in solution that have been dissociated from the NR surface.[12]

4.3.3 TA Spectroscopy of CdS NRs

Photodriven H_2 production is not a direct measure of ET, but is rather a result of many factors involved in catalysis. The fact that the H_2 production trend shown in Figure 4.3 follows an exponential decay indicates that the rate and efficiency of ET may determine the overall rate and yield of photodriven H_2 production in the CdS-CaI system. The electron tunneling distance, determined by the ligand layer, will affect the rate of the ET step. However, since the rate of ET is in direct competition with the photoexcited electron-hole recombination intrinsic to the nanocrystals, as established in Chapter 3, the efficiency of ET is determined by comparing the rates for both the recombination and ET processes in each sample. To begin this comparison, we use TA spectroscopy to monitor the relaxation kinetics of photoexcited CdS NRs with each of the various ligands used for H_2 production.

Upon photoexcitation of the CdS NRs, the excited state decay is intrinsic to the nanocrystals, including the nanocrystal surfaces. As the nanocrystal surface ligands are changed, the surface coverage and numbers of electron and hole trapping sites also change. Therefore, by changing the surface ligand, the intrinsic decay rate of the electron in the excited state is also altered. We used ultrafast TA spectroscopy over a temporal window of 10^{-13} – 10^{-6} s to directly probe the kinetics of electron relaxation in CdS NRs. Upon excitation with a 400 nm pump pulse, TA spectra of CdS NRs (Figure 4.4) exhibit a transient bleach feature at the 457 nm corresponding to the band gap transition (B1). The intensity of this feature is directly

proportional to the photoexcited $1\sigma_e$ electron population. The kinetics of the band gap bleach feature are a signature of the photoexcited electrons decaying from the CB edge through recombination with VB holes, electron trapping, and recombination with trapped holes. The feature at 473 nm is initially (< 1ps) a positive feature (A1) caused by the presence of hot excitons. After 1 ps, a broad bleach feature grows in around 479 nm (B2). The B1 and B2 bleach features at 457 nm and 479 nm are both associated with the CdS band gap transition in CdS NRs. The presence of larger diameter portions on a subpopulation of NRs, as described above, results in a bleach feature, corresponding to the X2 exciton, which is lower in energy (479 nm) than the original X1 exciton in the CdS rod (457 nm).[166] Therefore the kinetics of both B1 and B2 bleach features are a result of the population of photoexcited electrons at the CB edge, only in different parts of a NR.

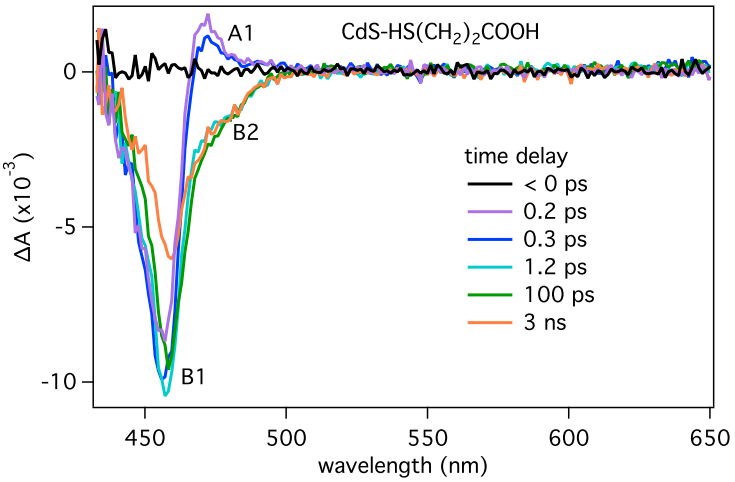

Figure 4.4 Transient absorption spectra of CdS NRs with a 3-carbon ligand at different time delays following 400 nm excitation. The CdS NRs exhibit a strong transient bleach feature, B1, at the band gap (457 nm) transition, a weaker red-shifted bleach feature, B2, at 479 nm, and a short-lived A1 feature at 473 nm.

The kinetics of the CdS NR B1 and B2 bleach features are shown in Figure 4.5. To facilitate the visualization of the complicated dynamics over many orders of magnitude in time, we use a linear time axis up to 10 ps, and a logarithmic scale thereafter. In each plot in Figure 4.5, the B1 kinetics are normalized to -1 at the bleach minimum. As observed from the TA spectra at a time delay of 500 ps, the B2 peak ranges in relative intensity from 11% to 22% of the B1 peak. Since the B1 kinetic traces are normalized to -1, the B2 kinetic traces are scaled proportionally (Figure 4.5). To observe the differences in the kinetics between samples with different ligands, the direct comparison of the B1 (Figure 4.6) and B2 (Figure 4.7) kinetics is plotted using both a (a) linear and (b) split axis. Following 400 nm excitation, we observe rapid (~ 1 ps) electron cooling to the CB edge as the A1 signal disappears and the B1 and B2 bleach features grow to their maximum intensity. The subsequent decay of the B1 and B2 kinetics are multi-exponential, consistent with previous reports.[95,98] For all of the CdS NR samples, the bleach kinetics decay to baseline in 1-10 μs. The relatively slow overall electron decay dynamics of CdS NRs have been attributed to the slow recombination of the delocalized CB electron with the localized, surface-trapped holes.[95]

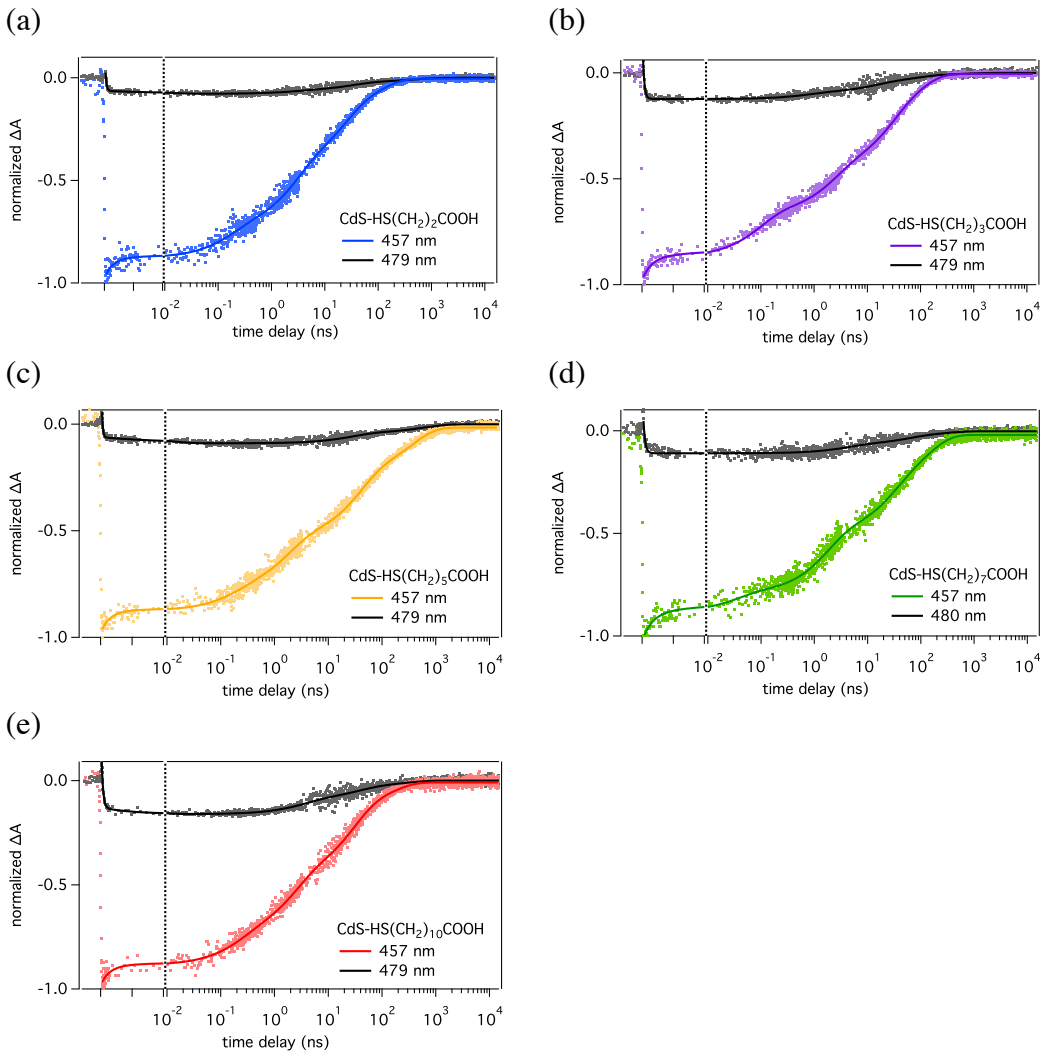

Figure 4.5 TA kinetics of the B1 (457 nm, color points) and B2 (479 nm, black points) features for CdS NRs with various ligands. The B1 kinetics are normalized to -1 at the bleach minimum and the B2 kinetics are normalized to the relative intensity. The kinetics are plotted with a split time axis that is linear for the first 10 ps and logarithmic thereafter. The solid lines correspond to a fit model using Eq 4.2 for the B1 kinetics and Eq 4.3 for the B2 kinetics.

(a)

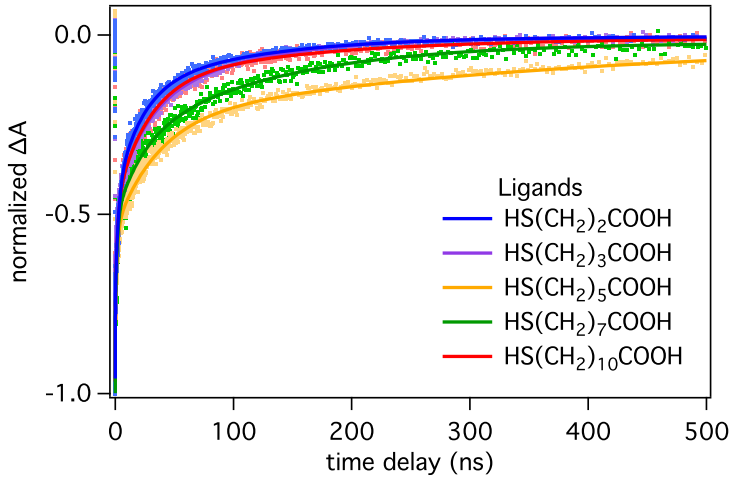

(b)

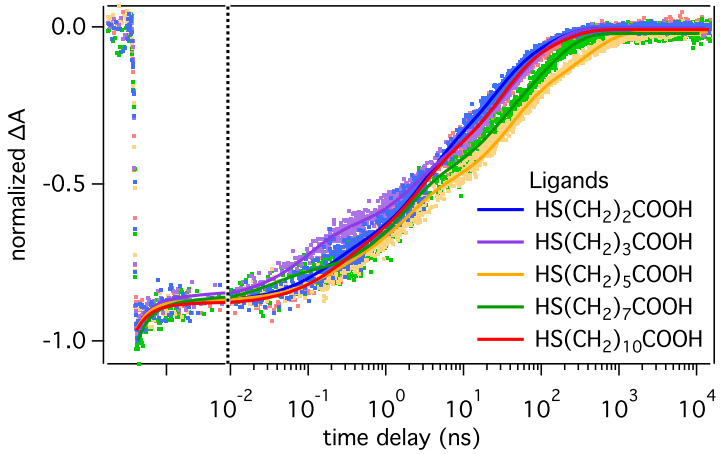

Figure 4.6 TA kinetics of the B1 band gap feature (457 nm) for CdS NRs with various ligands. The kinetics are normalized at the bleach minimum and plotted (a) with a linear time axis or (b) with a split time axis that is linear for the first 10 ps and logarithmic thereafter. The solid lines correspond to fits from Eq 4.2. The linear time axis demonstrates the differences in the overall lifetimes for each trace and the logarithmic time axis accentuates the differences in the shapes of the kinetic decays.

(a)

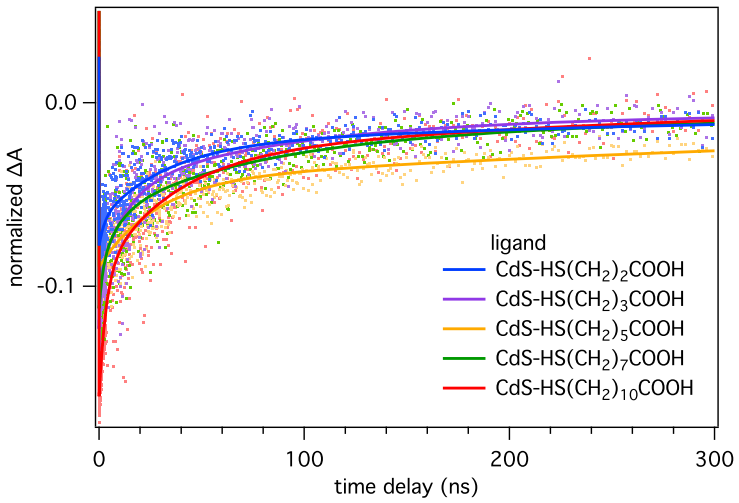

(b)

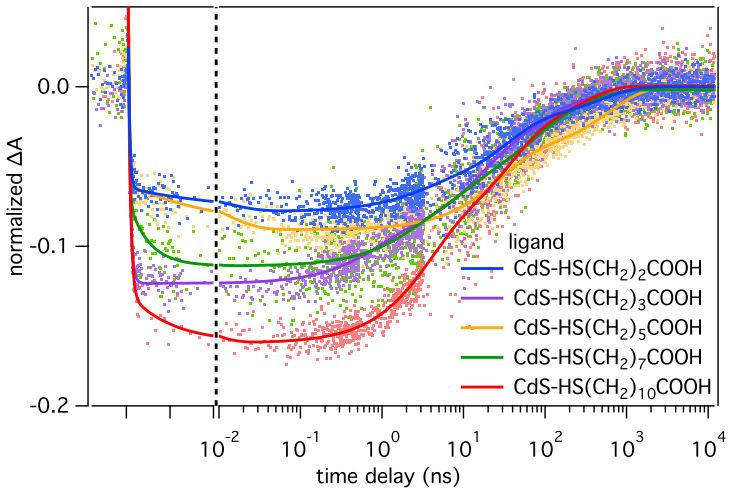

Figure 4.7 TA kinetics of the B2 feature (479 nm) for CdS NRs with various ligands. The kinetics are normalized relative to the B1 feature and plotted with a (a) linear axis and a (b) split time axis that is linear for the first 10 ps and logarithmic thereafter. The solid lines correspond to fits from Eq 4.3. The linear time axis demonstrates the differences in the overall lifetimes and the logarithmic time axis allows for visualization of the differences in the shapes of both the rise and decay of the kinetics.

4.3.4 Electron Decay Kinetics in CdS NRs

Quantifying the kinetic processes of the excited electron states in CdS NRs is particularly challenging because of the long-lived, multi-exponential character the TA kinetics. The complicated dynamics reflect the sample heterogeneity including size (i.e. rod diameter) and the quality of the surface ligand monolayer, which results in a variation in the number of carrier trapping sites at the nanocrystal surface, as observed for hole traps in trap PL (Figure 4.1b). Herein, we present two methods for analyzing and quantifying the CdS TA kinetics: (1) A multiple exponential fitting function to model the sample intensity for calculating average lifetimes and rates and (2) A kinetic model that determines an intrinsic decay rate constant for CdS by accounting for a distribution of electron trapping sites. Both of these fitting strategies detail characteristics of the CdS excited state dynamics, but neither fully account for the intricate electron kinetics over the full timescale. For this reason, we are continuing to develop a rigorous fitting model for the TA data presented in this chapter.

The first technique for quantifying the TA kinetics in Figure 4.5 involves identifying a fit equation that models the ΔA intensity of the kinetic data. At short time delays, a fast (~ 2 ps) exponential decay component constitutes about 13% decay of the B1. In the same time frame, the B2 bleach feature grows in. The remainder of the B2 and B2 kinetics, as the features slowly decay to baseline, can be fit with either a series of exponential functions or a stretched exponential, as shown in Chapter 3. As a demonstration of this method, the B1 kinetic data is fit to Eq 4.2.

$$f(t) = a_0 e^{-(t-t0)*k_0} + a_1 e^{-(t-t0)*k_1} + a_2 e^{-(t-t0)*k_2} + a_3 e^{-(t-t0)*k_3} + a_4 e^{-(t-t0)*k_4} + y_0$$

(Equation 4.2)

To adequately fit the B2 kinetics, it is necessary to include an additional exponential component at early delay times to account for the decay of the A1 feature. Therefore, the B2 kinetic data are fit with Eq 4.3.

$$f(t) = a_0 e^{-(t-t0)*k_0} + a_1 e^{-(t-t0)*k_1} + a_2 e^{-(t-t0)*k_2} + a_3 e^{-(t-t0)*k_3} + a_4 e^{-(t-t0)*k_4} + a_5 e^{-(t-t0)*k_5} + y_0 \quad \text{(Equation 4.3)}$$

After fitting the kinetics to the equations above and obtaining fit parameters, we quantify the kinetics through the average lifetime,

$$\bar{\tau} = \frac{\int_0^\infty t*\Delta A(t)dt}{\int_0^\infty \Delta A(t)dt} \quad \text{(Equation 4.4)}$$

and the time-averaged decay rate constant,

$$\bar{k} = \frac{1}{\int_0^\infty \Delta A(t)dt} \ . \quad \text{(Equation 4.5)}$$

The fit parameter results and calculations of $\bar{\tau}$ and $\bar{k}$ are detailed in Table 4.1 for B1 kinetics and Table 4.2 for B2 kinetics.

Table 4.1 The fitting parameters from fits of the normalized B1 bleach kinetics, as shown in Figure 4.6, to Eq 4.2.

Ligand		$\bar{\tau}$ (ns)	$\bar{k}$ (s^{-1})	Fit parameters	
$HS(CH_2)_2COOH$	n = 1	80	4.3×10^7	$a_0 = -0.13$ $a_1 = -0.14$ $a_2 = -0.29$ $a_3 = -0.28$ $a_4 = -0.16$	$k_0 = 6.7 \times 10^{11}\ s^{-1}$ $k_1 = 6.0 \times 10^{9}\ s^{-1}$ $k_2 = 3.9 \times 10^{8}\ s^{-1}$ $k_3 = 4.8 \times 10^{7}\ s^{-1}$ $k_4 = 9.6 \times 10^{6}\ s^{-1}$
$HS(CH_2)_3COOH$	n = 2	75	3.8×10^7	$a_0 = -0.13$ $a_1 = -0.20$ $a_2 = -0.21$ $a_3 = -0.24$ $a_4 = -0.22$	$k_0 = 6.7 \times 10^{11}\ s^{-1}$ $k_1 = 1.1 \times 10^{10}\ s^{-1}$ $k_2 = 4.6 \times 10^{8}\ s^{-1}$ $k_3 = 4.1 \times 10^{7}\ s^{-1}$ $k_4 = 1.1 \times 10^{7}\ s^{-1}$
$HS(CH_2)_5COOH$	n = 4	322	1.1×10^7	$a_0 = -0.13$ $a_1 = -0.09$ $a_2 = -0.24$ $a_3 = -0.30$ $a_4 = -0.22$	$k_0 = 6.7 \times 10^{11}\ s^{-1}$ $k_1 = 5.8 \times 10^{9}\ s^{-1}$ $k_2 = 5.7 \times 10^{8}\ s^{-1}$ $k_3 = 2.8 \times 10^{7}\ s^{-1}$ $k_4 = 2.8 \times 10^{6}\ s^{-1}$
$HS(CH_2)_7COOH$	n = 6	117	2.4×10^7	$a_0 = -0.13$ $a_1 = -0.10$ $a_2 = -0.28$ $a_3 = -0.22$ $a_4 = -0.26$	$k_0 = 6.7 \times 10^{11}\ s^{-1}$ $k_1 = 3.0 \times 10^{10}\ s^{-1}$ $k_2 = 6.0 \times 10^{8}\ s^{-1}$ $k_3 = 3.9 \times 10^{7}\ s^{-1}$ $k_4 = 7.5 \times 10^{6}\ s^{-1}$
$HS(CH_2)_{10}COOH$	n = 9	106	3.5×10^7	$a_0 = -0.13$ $a_1 = -0.14$ $a_2 = -0.28$ $a_3 = -0.33$ $a_4 = -0.13$	$k_0 = 6.7 \times 10^{11}\ s^{-1}$ $k_1 = 4.7 \times 10^{9}\ s^{-1}$ $k_2 = 4.6 \times 10^{8}\ s^{-1}$ $k_3 = 3.7 \times 10^{7}\ s^{-1}$ $k_4 = 6.9 \times 10^{6}\ s^{-1}$

Table 4.2 The fitting parameters and values resulting from fitting the B2 bleach kinetics, as shown in Figure 4.7 to Eq 4.3.

Ligand		$\bar{\tau}$ (ns)	$\bar{k}$ (s^{-1})	Fit parameters	
$HS(CH_2)_2COOH$	n = 1	607	6.9×10^6	$a_0 = 0.51$ $a_1 = 0.26$ $a_2 = -0.24$ $a_3 = -0.014$ $a_4 = -0.042$ $a_5 = -0.022$	$k_0 = 5.5 \times 10^{12}\ s^{-1}$ $k_1 = 8.7 \times 10^{10}\ s^{-1}$ $k_2 = 8.7 \times 10^{10}\ s^{-1}$ $k_3 = 3.9 \times 10^{8}\ s^{-1}$ $k_4 = 3.0 \times 10^{7}\ s^{-1}$ $k_5 = 2.1 \times 10^{6}\ s^{-1}$
$HS(CH_2)_3COOH$	n = 2	298	1.5×10^7	$a_0 = 0.036$ $a_1 = 0.036$ $a_2 = -0.029$ $a_3 = -0.046$ $a_4 = -0.037$ $a_5 = -0.012$	$k_0 = 5.2 \times 10^{12}\ s^{-1}$ $k_1 = 3.4 \times 10^{12}\ s^{-1}$ $k_2 = 1.3 \times 10^{9}\ s^{-1}$ $k_3 = 7.6 \times 10^{7}\ s^{-1}$ $k_4 = 1.2 \times 10^{7}\ s^{-1}$ $k_5 = 1.4 \times 10^{6}\ s^{-1}$
$HS(CH_2)_5COOH$	n = 4	1203	2.8×10^6	$a_0 = 0.74$ $a_1 = 0.26$ $a_2 = -0.23$ $a_3 = -0.015$ $a_4 = -0.047$ $a_5 = -0.042$	$k_0 = 6.8 \times 10^{12}\ s^{-1}$ $k_1 = 9.9 \times 10^{10}\ s^{-1}$ $k_2 = 8.0 \times 10^{12}\ s^{-1}$ $k_3 = 9.9 \times 10^{10}\ s^{-1}$ $k_4 = 3.6 \times 10^{7}\ s^{-1}$ $k_5 = 1.6 \times 10^{6}\ s^{-1}$
$HS(CH_2)_7COOH$	n = 6	198	1.5×10^7	$a_0 = 0.028$ $a_1 = 0.038$ $a_2 = -0.021$ $a_3 = -0.028$ $a_4 = -0.037$ $a_5 = -0.023$	$k_0 = 9.3 \times 10^{12}\ s^{-1}$ $k_1 = 4.3 \times 10^{11}\ s^{-1}$ $k_2 = 5.3 \times 10^{8}\ s^{-1}$ $k_3 = 1.1 \times 10^{8}\ s^{-1}$ $k_4 = 1.5 \times 10^{7}\ s^{-1}$ $k_5 = 3.3 \times 10^{6}\ s^{-1}$
$HS(CH_2)_{10}COOH$	n = 9	166	2.3×10^7	$a_0 = 0.030$ $a_1 = 0.029$ $a_2 = -0.046$ $a_3 = -0.020$ $a_4 = -0.063$ $a_5 = -0.032$	$k_0 = 4.2 \times 10^{12}\ s^{-1}$ $k_1 = 2.0 \times 10^{11}\ s^{-1}$ $k_2 = 3.1 \times 10^{8}\ s^{-1}$ $k_3 = 2.6 \times 10^{8}\ s^{-1}$ $k_4 = 2.9 \times 10^{7}\ s^{-1}$ $k_5 = 3.8 \times 10^{6}\ s^{-1}$

From the multi-exponential fitting results, we observed that the value of $\bar{k}$, the average rate of photoexcited electron-hole recombination, for each of the samples is on the order of 10^7 s^{-1} for the B1 bleach and 10^6 -10^7 s^{-1} for the B2 bleach. The CdS NR bleach kinetics exhibit average lifetimes of 80 ns to 1.2 μs. Photoexcited electrons are consistently longer lived in the localized (B2) state than in the delocalized B1 electron state. We observed that the excited

electron decay rates depend on the identity of the NR surface ligands, but do not trend with the number of carbons in each ligand.

The multi-exponential fits suggest that the CdS NR excited state kinetics contain a distribution of electron decay rates. By characterizing kinetics using averaging quantities, $\bar{\tau}$ and $\bar{k}$, we do not account for differences in underlying sample heterogeneity between the nanocrystal samples. Different surface ligand identities are prone to creating a different ligand monolayer, introducing a different number of electron trap sites.[140] TA dynamics reflect the heterogeneities present in nanocrystal samples, some of which arise from variations in the number of electron trapping sites on the nanocrystal surface.[129,174] To account for the sample heterogeneity reflected in the TA signal, we can employ a kinetic model that explicitly includes the number distribution of electron trap sites per CdS NR in the ensemble sample, which my coworkers and I have recently applied to CdS TA kinetics (Eq 4.6).[40]

$$P_{\mathrm{CdS}}(t) = a_0 \exp\{-k_0 t\} + a_1 \exp\{-k_1 t + \langle N_{\mathrm{tr1}}\rangle(e^{-k_{\mathrm{tr1}}t} - 1) + \langle N_{\mathrm{tr2}}\rangle(e^{-k_{\mathrm{tr2}}t} - 1)\}$$

(Equation 4.6)

Here k_0 is the rate constant for exciton localization, k_1 is the sum of the rate constants for radiative and nonradiative recombination of the electron with the hole, and k_{tr1} & k_{tr2} are the rate constants for the electron trapping processes. In this model, the values of these rate constants are equal in all particles in the ensemble. $<N_{trl}>$ & $<N_{trl}>$ are the average number of each type of electron trap in the ensemble, which are a result of averaging over a Poisson distribution for each type of trap state. A merit of this model is that it reveals the intrinsic rate constant for electron relaxation, k_1. A similar model was developed for the study of quenching kinetics of luminescent probes in micellar systems,[175,176] and has more recently been employed to study the kinetics of

carrier trapping in nanocrystals,[98,131] as well as energy,[177,178] hole[99] and electron transfer[179] in nanocrystal–acceptor complexes.

The results from fitting the kinetics of the B1 feature to this model (Eq 4.6) are shown in Table 4.3. Since ligand exchange to mercaptocarboxylates proceeds from the same stock of CdS NRs, the rate constants intrinsic to the nanocrystals are expected to be the same for each of the CdS NR samples. Therefore, the rate constants, k_1, k_{tr1}, and k_{tr2} were held constant at the values optimized for the set of kinetics while $<N_{tr1}>$, $<N_{tr2}>$, and the preexponential constants, a_0 and a_1, were allowed to vary. k_0 was allowed to vary because the kinetics revealed that the rates of exciton localization, while always on the ps time scale, are not equivalent in each sample.

Table 4.3 The parameters resulting from fitting the TA data for the B1 feature in CdS NRs, shown in Figure 4.6, to the kinetic model (Eq 4.6).

Ligand		k_0	k_1	$\langle N_{tr1} \rangle$	k_{tr1}	$\langle N_{tr2} \rangle$	k_{tr2}
$HS(CH_2)_2COOH$	n = 1	1.7 x 10^{10} s^{-1}	1.5 x 10^6 s^{-1}	3.50	1.0 x 10^7 s^{-1}	0.44	6.8 x 10^8 s^{-1}
$HS(CH_2)_3COOH$	n = 2	1.9 x 10^{10} s^{-1}	1.5 x 10^6 s^{-1}	2.75	1.0 x 10^7 s^{-1}	0.35	6.8 x 10^8 s^{-1}
$HS(CH_2)_5COOH$	n = 4	1.2 x 10^{11} s^{-1}	1.5 x 10^6 s^{-1}	1.32	1.0 x 10^7 s^{-1}	0.44	6.8 x 10^8 s^{-1}
$HS(CH_2)_7COOH$	n = 6	1.8 x 10^{11} s^{-1}	1.5 x 10^6 s^{-1}	1.86	1.0 x 10^7 s^{-1}	0.44	6.8 x 10^8 s^{-1}
$HS(CH_2)_{10}COOH$	n = 9	2.0 x 10^{10} s^{-1}	1.5 x 10^6 s^{-1}	2.86	1.0 x 10^7 s^{-1}	0.48	6.8 x 10^8 s^{-1}

To fit the B2 kinetics to the electron kinetic model described above, we used Eq 4.6 with the addition of another exponential during the short time-delays to account for the decay of the A1 feature (k_A). We expect the number of each type of trap to be equivalent from fitting the B1 and B2 since both types of traps are mid-gap energy levels and are also accessible to the lower-energy B2 electron. However, because B2 corresponds to a lower-energy, localized electron

state, we expect that the trapping rates could be slower than the B1 trapping rates. Therefore, to fit the B2 kinetics, only the rate constant k_1 was held constant while k_{tr1}, and k_{tr2} were allowed to vary. The values for $\langle N_{tr1} \rangle$, $\langle N_{tr2} \rangle$ were also held constant at the values calculated for the B1 kinetics. The results of these fits are tabulated in Table 4.4.

Table 4.4 The parameters resulting from fitting the TA data from the B2 bleach in CdS NRs, as shown in Figure 4.7 to the electron kinetic model.

Ligand		k_A	k_0	k_1	$\langle N_{tr1} \rangle$	k_{tr1}	$\langle N_{tr2} \rangle$	k_{tr2}
$HS(CH_2)_2COOH$	n = 1	6.0 x 10^{12} s^{-1}	1.4 x 10^{11} s^{-1}	1.0 x 10^{6} s^{-1}	3.50	2.2 x 10^{6} s^{-1}	0.44	1.2 x 10^{8} s^{-1}
$HS(CH_2)_3COOH$	n = 2	5.0 x 10^{12} s^{-1}	1.6 x 10^{12} s^{-1}	1.0 x 10^{6} s^{-1}	2.75	8.5 x 10^{6} s^{-1}	0.35	6.3 x 10^{8} s^{-1}
$HS(CH_2)_5COOH$	n = 4	4.7 x 10^{12} s^{-1}	4.7 x 10^{10} s^{-1}	1.0 x 10^{6} s^{-1}	1.32	1.9 x 10^{6} s^{-1}	0.44	6.5 x 10^{7} s^{-1}
$HS(CH_2)_7COOH$	n = 6	9.9 x 10^{12} s^{-1}	4.5 x 10^{11} s^{-1}	1.0 x 10^{6} s^{-1}	1.86	6.8 x 10^{6} s^{-1}	0.44	2.5 x 10^{8} s^{-1}
$HS(CH_2)_{10}COOH$	n = 9	4.4 x 10^{12} s^{-1}	2.3 x 10^{11} s^{-1}	1.0 x 10^{6} s^{-1}	2.86	6.9 x 10^{6} s^{-1}	0.48	2.6 x 10^{8} s^{-1}

The results from fitting the CdS excited state dynamics indicate that electron-hole recombination is competing with two types of faster electron trapping processes. The first type of trap (N_{tr1}) has a slower trapping rate and the average number of traps, $\langle N_{tr1} \rangle$, changes as the nanocrystal surface ligand is varied. The second type of trap is an order of magnitude faster and the average number, $\langle N_{tr2} \rangle$, is not influenced by the length of the surface ligands. The fit results show electron trapping of the delocalized electrons associated with the B1 state is faster than trapping of the localized electrons in the B2 state. The slower trapping of localized electrons occurs on timescales close to recombination.

4.3.5 Predicted ET Kinetics for CdS-CaI Complexes

In order to understand the kinetics that would be expected for ET through the ligand interface in CdS-CaI complexes, we calculated predicted values for k_{ET} and QE_{ET} at each ligand length. Predicted k_{ET} values for each ligand length were calculated using Eq 4.7 with a β value of 0.82 $Å^{-1}$, which was determined for ET from an Au electrode to CaI,[63] and using the ligand lengths (d) from Section 4.3.1.1. The value for $k_{ET\,(d=0)}$, 2.5 x 10^9 s^{-1}, was calculated using the value of k_{ET} reported in Chapter 3 for CaI:CdS complexes with the 3-carbon ligand (5.88 Å) by extrapolating to d=0. The predicted k_{ET} values are plotted as a function of ligand length in Figure 4.8 with the exponential decay with β = 0.82 $Å^{-1}$ shown in black. The predicted rate constants for ET through the ligands with > 4 carbons are smaller than the intrinsic rate constant for recombination (k_1) calculated for CdS NRs using Eq 4.6, as indicated by the dashed green line.

$$k_{ET_d} = k_{ET_{(d=0)}} * e^{(-\beta * d)} \qquad \text{(Equation 4.7)}$$

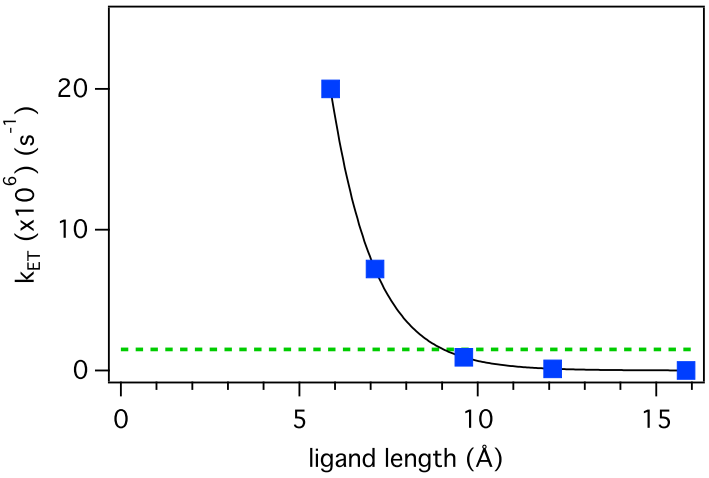

Figure 4.8 Predicted values for k_{ET} in CdS-CaI complexes for varied lengths of CdS surface ligands. The black trace is an exponential decay (Eq 4.7) with β = 0.82 $Å^{-1}$. The green dashed line indicates 1.5 x 10^6 s^{-1}, which corresponds to k_1.

The quantum efficiency of ET, QE_{ET}, is determined by both the intrinsic excited state decay rate of the CdS NRs, $\bar{k}_{CdS}$, and the rate of ET, $\bar{k}_{ET}$ (Eq 4.8). We calculated hypothetical values for QE_{ET} using the experimentally determined average values (average of the electron recombination and trapping rates) for $\bar{k}_{CdS}$ calculated from the multi-exponential fits (Eq 4.2) for the B1 bleach decay and the predicted values for k_{ET} from Figure 4.8. The results are plotted versus ligand length in Figure 4.9 for ET out of the B1 state.

$$QE_{ET} = \frac{k_{ET}}{k_{CdS}+k_{ET}} \qquad \text{(Equation 4.8)}$$

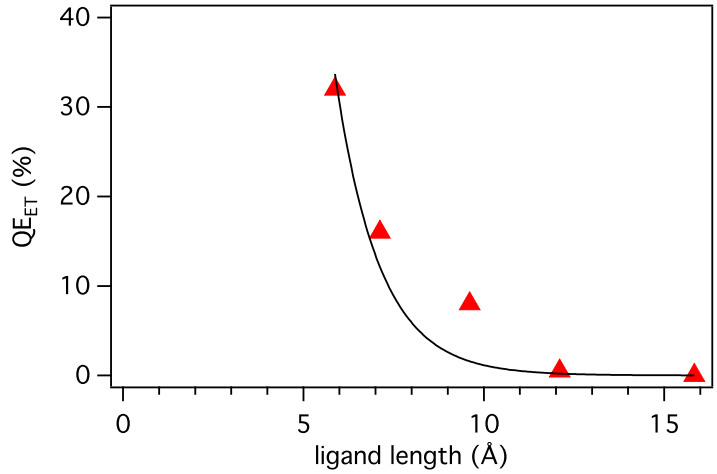

Figure 4.9 Predicted values for QE_{ET} for electrons from the B1 state of photoexcited CdS. The black trace is an exponential decay (Eq 4.7) with $\beta = 0.82$ Å^{-1}.

In Figure 4.9, the black exponential curve is the same as in Figure 4.8 where $\beta = 0.82$ Å^{-1}. The calculated QE_{ET} results do not fall exactly on this exponential curve because the CdS excited state lifetime was altered by the ligand exchange. The CdS NRs with 6-carbon (9.6 Å;

n=4) ligands on the surface have particularly long-lived excited states, which would allow more time for the photoexcited electron to be extracted from the nanocrystal. Thus, with a higher efficiency for ET (Figure 4.9), we would expect a greater yield of photodriven H_2 production since the QE_{ET} dictates the upper limit for the QY of H_2 generation. This is precisely what we observed, as shown in Figure 4.3, that the H_2 from the 6-carbon ligand (yellow point, n = 4) exceeded the amount predicted by the exponential (black trace) fit of the other data points.

4.3.6 TA Kinetics of CdS-CaI Complexes

As outlined in Chapter 3, the presence of CaI introduces ET as an additional pathway by which photoexcited electrons in CdS NRs can decay. In TA spectra this causes the bleach kinetics to decay to baseline more quickly. For the CdS NRs with nonuniform diameters, intraparticle exciton localization is fast (ps) and is expected to be complete before ET processes. Therefore, we expect ET to occur from both the B1 and B2 electron states, as previously shown for ET from CdS NRs to Pt.[29] Figure 4.10 and Figure 4.11 show normalized kinetic traces of CdS-CaI complexes with various ligands for the B1 and B2 transitions, respectively. The solutions of CdS-CaI complexes with 11-carbon ligand were not stable in a 12 mM Tris buffer solution for extended periods of time, unlike the complexes with the other ligands, and TA spectra could not be collected.

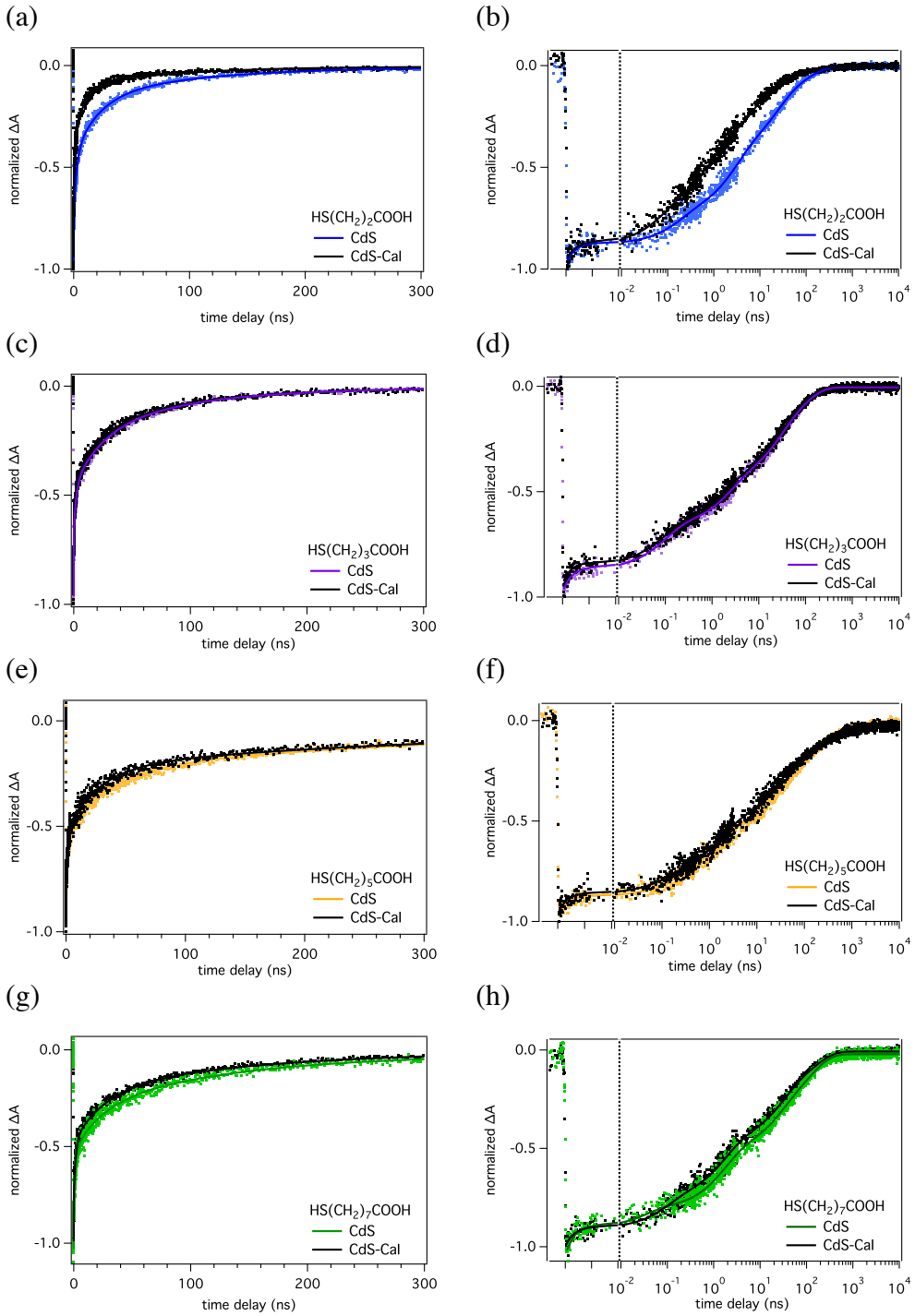

Figure 4.10 TA kinetics of the B1 feature (457 nm) for CdS NRs with various ligands both without (color) and with CaI (black) mixed in a 1:1 ratio. The kinetics are plotted with a linear time axis (left) or with a split time axis that is linear for the first 10 ps and logarithmic thereafter (right). The kinetics are normalized at the bleach maximum.

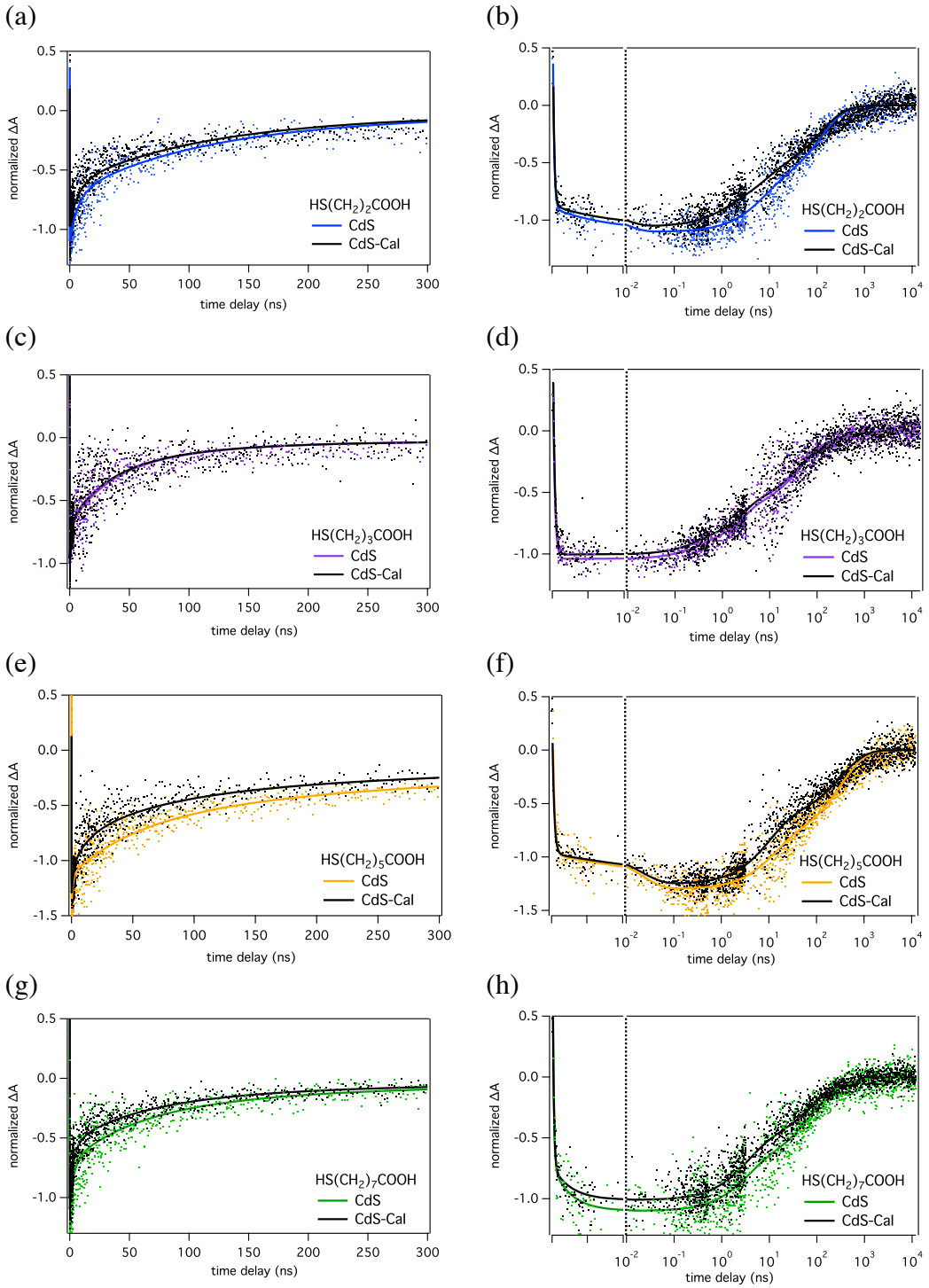

Figure 4.11 TA kinetics of the B2 feature (479 nm) for CdS NRs with various ligands both without (color) and with CaI (black) mixed in a 1:1 ratio. The kinetics are plotted with a linear time axis or with a split time axis (left) that is linear for the first 10 ps and logarithmic thereafter (after). The kinetics are normalized to -1 at the bleach maximum.

The experimental TA kinetics of the CdS NR band gap transition (B1) in samples of CdS-CaI complexes mediated by various length surface ligands show a notably faster decay of the electron population compared to CdS NRs alone only for the sample containing the n=1 ligand (Figure 4.10). The samples containing a longer-length surface ligand demonstrate kinetics that are very similar to the original CdS NR sample kinetics with the corresponding ligand (Figure 4.10). The predicted values of QE_{ET} from the B1 state hypothesize that the efficiency will drop below 10% for ET through ligands with > 4 carbons (Figure 4.9). When the probability of transferring an electron is < 10%, we would expect to observe only a small contribution to the TA kinetics from ET within CdS-CaI complexes. Therefore, the B1 kinetics of CdS-CaI complexes that were not distinguishable from those of the CdS NRs alone with the same surface ligand can be explained by the predicted slow ET and a small QE_{ET} values.

The B1 kinetics for the CdS-CaI complexes were fit to the multi-exponential equation (Eq 4.2) and from the fits, we calculated average lifetimes and rate constants for the excited state of the complexes. By modeling the ΔA intensity for the kinetics of both CdS and CdS-CaI complexes, we attempted to quantify the extent of ET by calculating k_{ET} (Eq 4.7) and QE_{ET} (Eq 4.8). The resulting values representing ET for CdS NRs with the 3-carbon ligand are similar to those reported in Chapter 3, with a QE_{ET} ~40%. The values for QE_{ET} for photoexcited CdS NRs to CaI coupled with longer ligands are small or negligible.

The TA kinetics at the wavelength corresponding to the CdS B2 feature in samples of CdS-CaI complexes do not follow the same trend as the B1 kinetics. Instead, the longer-lived, localized electron of the B2 state exhibits more potential for ET in samples with ligands of longer lengths. The TA kinetics for CdS-CaI complexes containing the 4-carbon ligand does not

have a distinguishable ET signal. However, the kinetics for CdS-CaI complexes with 6-carbon and 8-carbon ligands exhibit a clear shortening of the excited state lifetime. The ET measured from the B2 state may be a result of the slow electron trapping rates associated with these samples. Although the initial electron population of the B2 state is small (12-14%), and the overall QE_{ET} is dominated by the B1 kinetics, the transfer of these localized electrons to CaI may have an important contribution to overall photocatalysis in nanocrystals with few electron traps.

At this time, we are able to only qualitatively describe the extent of ET exhibited by the CdS-CaI complexes with ligands > 4 carbons. By fitting the signal intensity of the TA kinetics to a series of exponential fits and comparing the resulting average quantities, we can visualize small changes in the kinetics but the errors associated with the ET rates and efficiencies that we can calculate are large. In order to more accurately extract a rate constant for ET, we will need to fit the electron decay from CdS-CaI complexes to a more sophisticated electron kinetic model. One method may be treating the number of CaI adsorbed onto each NR as an additional Poisson distribution, as we have done for CdS NRs capped with 3-MPA.[40] Even in this case, it would be ideal to increase the signal from ET to minimize errors in determining ET rate constants.[40] To achieve this, we can increase the CaI:CdS molar ratios in solution. Adding more electron-accepting CaI moieties to the surface of a CdS NR increases the probability for ET, which increases the overall ET rate as demonstrated in Chapter 3. By varying the number of CaI:CdS complexes in a solution, we could then extract rate constants for ET using our recently reported kinetic model.[40]

4.4 Conclusions

We have studied the effect of changing the length of the CdS NR surface ligand on nanocrystal excited state dynamics as well as photodriven H_2 production and charge transfer in CdS-CaI complexes. We observed an exponential decrease in H_2 production with increasing lengths of the nanocrystal surface ligands. From this observation, we propose that the transfer of photoexcited electrons in the CdS to CaI occurs through the ligand layer, which acts as a tunneling barrier. If the ligand were to act as a tunneling barrier, ET rates would exponentially decrease with ligand length, causing the exponentially decreasing H_2 production with ligand length, which we observed experimentally. The quantum efficiency of ET depends on both the rate of ET and the rate of electron-hole recombination within the photoexcited nanocrystal. To understand the interplay of these rates, we measured both the dynamics of the photoexcited electron in CdS NRs with and without CaI using transient absorption spectroscopy. Due to the effects of using rods with nonuniform diameters, it was necessary to monitor the electron dynamics of both the delocalized B1 state and the more localized B2 state. Each sample of CdS NRs with a different length ligand exhibited unique kinetics of the excited state electron population. Since the rate of electron-hole recombination is intrinsic to the CdS NRs, we attributed the differences in the kinetics after ligand exchange to electron trapping at the nanocrystal surface. The excited state dynamics of CdS-CaI complexes exhibited significant ET signal for only the shortest ligands because, under the conditions used for TA, the efficiency for ET through the longer ligands is predicted to be < 10%. Further efforts to measure and quantify ET rates as a function of ligand length will allow us to better understand the electron pathways

involved in photochemical H_2 generation and will guide the design of improved hybrid nanostructures.

Chapter 5 Conclusions and Outlook

Chapter 2 demonstrated a charge transfer mechanism that involves hole transfer from photoexcited CdS nanorods to the HOMO of the water oxidation catalyst, [Ru(deeb)(tpy)Cl]. Unfortunately, under the conditions of our current experiment, this was followed by electron transfer from the conduction band of CdS to the same orbital on [Ru(deeb)(tpy)Cl], recombining with the previously-transferred hole. The second, substantially slower step could be averted through the introduction of additional electron harvesting pathways. Quickly diverting the photoexcited electrons away from the oxidation catalyst would allow for the accumulation of multiple holes on the catalyst, thereby facilitating O-O bond formation. It has been previously established that CdS nanorods readily transfer electrons to both molecular acceptors (ie: methyl viologen)[11] and catalysts for H^+ reduction (ie: Pt)[95]. Consequently, an extension of this study would be to combine the existing CdS NR-Ru^{2+} catalyst complex with electron-accepting molecules and/or nanoparticles. If the electron transfer were sufficient, we would expect the Ru metal centers would continue to be oxidized with continuous photoexcitation events. Successful water oxidation could be measured by detecting molecular oxygen using gas chromatography.

Chapter 3 examines the kinetics of electron transfer from light-absorbing CdS nanorods to biomimetically-coupled hydrogenases, enzymes that catalyze the reduction of $2H^+$ to H_2. The electron transfer process is essential for photochemical generation of H_2 mediated by these complexes, and its efficiency defines the upper limit for the quantum yield of H_2 production. From the results presented in Chapter 3, it was determined that the electron transfer rate constant was similar to the rate constant for the decay of photoexcited electrons in CdS NRs, resulting in

42% efficient electron transfer in a sample with the average CdS:hydrogenase ratio of 1:1. The efficiency of electron transfer could be improved in the future by a combination of increasing the electron transfer rate and decreasing the rate of excited state electron decay in the nanocrystal. This could be achieved through synthetic modifications of nanocrystal surface chemistry and band structure.

Our observations presented in Chapter 4 lead us to propose that the transfer of photoexcited electrons from CdS to hydrogenase occurs through the ligand layer, which acts as a tunneling barrier. Therefore, the choice of surface-capping ligands could strongly influence electron transfer rates in nanocrystal-hydrogenase complexes. By choosing a nanocrystal surface ligand with a smaller electron-tunneling barrier (decreasing barrier height or length), the rate of electron transfer could be decreased. However, as discussed in Chapter 4, the process of exchanging the surface ligands introduces a different number of carrier trap sites on the nanocrystal surfaces, which also affects the rate of photoexcited electron-hole recombination. An extension of this project is to manipulate the nanocrystal ligands using shorter, more conductive ligand choices.

These insights into the kinetics of charge transfer from CdS nanorods to redox catalysts allow us to begin to assemble a picture of the complex electron and hole pathways involved in performing photochemical reactions on the surface of the nanorods. Further efforts to measure and quantify charge transfer rates using time-resolved spectroscopy will allow us to better understand the charge carrier pathways involved in the photocatalysis of H_2 or O_2 generation. This work can be extended by synthetically modifying or adding structural complexity to the

systems discussed in this dissertation and could ultimately guide the design of hybrid nanostructures used to efficiently generate solar fuels.

Chapter 6 References

(1) Lewis, N. S.; Nocera, D. G. *Proc Nat Acad Sci USA* **2006**, *103*, 15729.

(2) Wilker, M. B.; Schnitzenbaumer, K. J.; Dukovic, G. *Isr J Chem* **2012**, *52*, 1002.

(3) Berr, M. J.; Vaneski, A.; Mauser, C.; Fischbach, S.; Susha, A. S.; Rogach, A. L.; Jackel, F.; Feldmann, J. *Small* **2012**, *8*, 291.

(4) Acharya, K. P.; Khnayzer, R. S.; O'Connor, T.; Diederich, G.; Kirsanova, M.; Klinkova, A.; Roth, D.; Kinder, E.; Imboden, M.; Zamkov, M. *Nano Lett* **2011**, *11*, 2919.

(5) Amirav, L.; Alivisatos, A. P. *J Phys Chem Lett* **2010**, *1*, 1051.

(6) Brown, K. A.; Dayal, S.; Ai, X.; Rumbles, G.; King, P. W. *J Am Chem Soc* **2010**, *132*, 9672.

(7) Wang, F.; Wang, W. G.; Wang, X. J.; Wang, H. Y.; Tung, C. H.; Wu, L. Z. *Angew Chem Int Edit* **2011**, *50*, 3193.

(8) Shemesh, Y.; Macdonald, J. E.; Menagen, G.; Banin, U. *Angew Chem Int Edit* **2011**, *50*, 1185.

(9) Greene, B. L.; Joseph, C. A.; Maroney, M. J.; Dyer, R. B. *J Am Chem Soc* **2012**, *134*, 11108.

(10) Tang, M. L.; Grauer, D. C.; Lassalle-Kaiser, B.; Yachandra, V. K.; Amirav, L.; Long, J. R.; Yano, J.; Alivisatos, A. P. *Angew Chem Int Edit* **2011**, *50*, 10203.

(11) Zhu, H.; Song, N.; Lv, H.; Hill, C. L.; Lian, T. *J Am Chem Soc* **2012**, *134*, 11701.

(12) Brown, K. A.; Wilker, M. B.; Boehm, M.; Dukovic, G.; King, P. W. *J Am Chem Soc* **2012**, *134*, 5627.

(13) Han, Z. J.; Qiu, F.; Eisenberg, R.; Holland, P. L.; Krauss, T. D. *Science* **2012**, *338*, 1321.

(14) Li, C. B.; Li, Z. J.; Yu, S.; Wang, G. X.; Wang, F.; Meng, Q. Y.; Chen, B.; Feng, K.; Tung, C. H.; Wu, L. Z. *Energ Environ Sci* **2013**, *6*, 2597.

(15) Kudo, A.; Miseki, Y. *Chem Soc Rev* **2009**, *38*, 253.

(16) Donega, C. D.; Koole, R. *J Phys Chem C* **2009**, *113*, 6511.

(17) Yu, W. W.; Qu, L. H.; Guo, W. Z.; Peng, X. G. *Chem Mater* **2003**, *15*, 2854.

(18) Brus, L. *J Phys Chem* **1986**, *90*, 2555.

(19) Donega, C. D. *Chem Soc Rev* **2011**, *40*, 1512.

(20) Van de Walle, C. G.; Neugebauer, J. *Nature* **2003**, *423*, 626.

(21) Hines, D. A.; Kamat, P. V. *ACS Appl Mater Inter* **2014**, *6*, 3041.

(22) Talapin, D. V.; Lee, J. S.; Kovalenko, M. V.; Shevchenko, E. V. *Chem Rev* **2010**, *110*, 389.

(23) Amirav, L.; Alivisatos, A. P. *J Am Chem Soc* **2013**, *135*, 13049.

(24) Bang, J. U.; Lee, S. J.; Jang, J. S.; Choi, W.; Song, H. *J Phys Chem Lett* **2012**, *3*, 3781.

(25) Berr, M.; Vaneski, A.; Susha, A. S.; Rodriguez-Fernandez, J.; Doblinger, M.; Jackel, F.; Rogach, A. L.; Feldmann, J. *Appl Phys Lett* **2010**, *97*, 093108.

(26) Berr, M. J.; Schweinberger, F. F.; Doblinger, M.; Sanwald, K. E.; Wolff, C.; Breimeier, J.; Crampton, A. S.; Ridge, C. J.; Tschurl, M.; Heiz, U.; Jackel, F.; Feldmann, J. *Nano Lett* **2012**, *12*, 5903.

(27) Schneider, J.; Vaneski, A.; Pesch, G. R.; Susha, A. S.; Teoh, W. Y.; Rogach, A. L. *Apl Mater* **2014**, *2*, 126102.

(28) Vaneski, A.; Susha, A. S.; Rodriguez-Fernandez, J.; Berr, M.; Jackel, F.; Feldmann, J.; Rogach, A. L. *Adv Funct Mater* **2011**, *21*, 1547.

(29) Wu, K. F.; Chen, Z. Y.; Lv, H. J.; Zhu, H. M.; Hill, C. L.; Lian, T. Q. *J Am Chem Soc* **2014**, *136*, 7708.

(30) Simon, T.; Bouchonville, N.; Berr, M. J.; Vaneski, A.; Adrovic, A.; Volbers, D.; Wyrwich, R.; Doblinger, M.; Susha, A. S.; Rogach, A. L.; Jackel, F.; Stolarczyk, J. K.; Feldmann, J. *Nat Mater* **2014**, *13*, 1013.

(31) Wang, P.; Zhang, J.; He, H. L.; Xua, X. T.; Jin, Y. D. *Nanoscale* **2014**, *6*, 13470.

(32) Cao, S.; Wang, C. J.; Lv, X. J.; Chen, Y.; Fu, W. F. *Appl Catal B-Environ* **2015**, *162*, 381.

(33) Das, A.; Han, Z. J.; Haghighi, M. G.; Eisenberg, R. *P Natl Acad Sci USA* **2013**, *110*, 16716.

(34) Gimbert-Surinach, C.; Albero, J.; Stoll, T.; Fortage, J.; Collomb, M. N.; Deronzier, A.; Palomares, E.; Llobet, A. *J Am Chem Soc* **2014**, *136*, 7655.

(35) Huang, J.; Mulfort, K. L.; Du, P.; Chen, L. X. *J Am Chem Soc* **2012**, *134*, 16472.

(36) Wen, F. Y.; Yang, J. H.; Zong, X.; Ma, B. J.; Wang, D. G.; Li, C. *J Catal* **2011**, *281*, 318.

(37) Brown, K. A.; Song, Q.; Mulder, D. W.; King, P. W. *ACS Nano* **2014**, *8*, 10790.

(38) Reisner, E.; Fontecilla-Camps, J. C.; Armstrong, F. A. *Chem Commun* **2009**, 550.

(39) Reisner, E.; Powell, D. J.; Cavazza, C.; Fontecilla-Camps, J. C.; Armstrong, F. A. *J Am Chem Soc* **2009**, *131*, 18457.

(40) Utterback, J. K.; Wilker, M. B.; Brown, K. A.; King, P. W.; Eaves, J. D.; Dukovic, G. *Phys Chem Chem Phys* **2015**, *17*, 5538.

(41) Wilker, M. B.; Shinopoulos, K. E.; Brown, K. A.; Mulder, D. W.; King, P. W.; Dukovic, G. *J Am Chem Soc* **2014**, *136*, 4316.

(42) Kambhampati, P. *J Phys Chem C* **2011**, *115*, 22089.

(43) Klimov, V. I. *Annu Rev Phys Chem* **2007**, *58*, 635.

(44) Blankenship, R. E.; Tiede, D. M.; Barber, J.; Brudvig, G. W.; Fleming, G.; Ghirardi, M.; Gunner, M. R.; Junge, W.; Kramer, D. M.; Melis, A.; Moore, T. A.; Moser, C. C.; Nocera, D. G.; Nozik, A. J.; Ort, D. R.; Parson, W. W.; Prince, R. C.; Sayre, R. T. *Science* **2011**, *332*, 805.

(45) Reisner, E. *Eur J Inorg Chem* **2011**, 1005.

(46) Woolerton, T. W.; Sheard, S.; Chaudhary, Y. S.; Armstrong, F. A. *Energ Environ Sci* **2012**, *5*, 7470.

(47) Noy, D.; Moser, C. C.; Dutton, P. L. *Bba-Bioenergetics* **2006**, *1757*, 90.

(48) Adams, M. W. W. *Biochim Biophys Acta* **1990**, *1020*, 115.

(49) Albery, W. J.; Knowles, J. R. *Biochemistry-US* **1976**, *15*, 5631.

(50) Armstrong, F. A.; Belsey, N. A.; Cracknell, J. A.; Goldet, G.; Parkin, A.; Reisner, E.; Vincent, K. A.; Wait, A. F. *Chem Soc Rev* **2009**, *38*, 36.

(51) Armstrong, F. A.; Hirst, J. *P Natl Acad Sci USA* **2011**, *108*, 14049.

(52) Dewar, M. J. S.; Storch, D. M. *P Natl Acad Sci USA* **1985**, *82*, 2225.

(53) Fauque, G.; Peck, H. D.; Moura, J. J. G.; Huynh, B. H.; Berlier, Y.; Dervartanian, D. V.; Teixeira, M.; Przybyla, A. E.; Lespinat, P. A.; Moura, I.; Legall, J. *FEMS Microbiol Rev* **1988**, *54*, 299.

(54) Fontecilla-Camps, J. C.; Amara, P.; Cavazza, C.; Nicolet, Y.; Volbeda, A. *Nature* **2009**, *460*, 814.

(55) Lubitz, W.; Reijerse, E.; van Gastel, M. *Chem Rev* **2007**, *107*, 4331.

(56) Siegbahn, P. E. M.; Tye, J. W.; Hall, M. B. *Chem Rev* **2007**, *107*, 4414.

(57) Vignais, P. M.; Billoud, B. *Chem Rev* **2007**, *107*, 4206.

(58) Vincent, K. A.; Parkin, A.; Armstrong, F. A. *Chem Rev* **2007**, *107*, 4366.

(59) Warshel, A. *J Biol Chem* **1998**, *273*, 27035.

(60) Warshel, A.; Sharma, P. K.; Kato, M.; Xiang, Y.; Liu, H. B.; Olsson, M. H. M. *Chem Rev* **2006**, *106*, 3210.

(61) Mulder, D. W.; Shepard, E. M.; Meuser, J. E.; Joshi, N.; King, P. W.; Posewitz, M. C.; Broderick, J. B.; Peters, J. W. *Structure* **2011**, *19*, 1038.

(62) Hamon, C.; Ciaccafava, A.; Infossi, P.; Puppo, R.; Even-Hernandez, P.; Lojou, E.; Marchi, V. *Chem Commun* **2014**, *50*, 4989.

(63) Madden, C.; Vaughn, M. D.; Díez-Pérez, I.; Brown, K. A.; King, P. W.; Gust, D.; Moore, A. L.; Moore, T. A. *J Am Chem Soc* **2012**, *134*, 1577.

(64) Demuez, M.; Cournac, L.; Guerrini, O.; Soucaille, P.; Girbal, L. *FEMS Microbiol Lett* **2007**, *275*, 113.

(65) Moulis, J.-M.; Davasse, V. *Biochemistry-US* **2002**, *34*, 16781.

(66) Peters, J. W. *Curr Opin Struc Biol* **1999**, *9*, 670.

(67) Fontecilla-Camps, J. C.; Volbeda, A.; Cavazza, C.; Nicolet, Y. *Chem Rev* **2007**, *107*, 5411.

(68) Artero, V.; Fontecave, M. *Chem Soc Rev* **2013**, *42*, 2338.

(69) Tran, P. D.; Wong, L. H.; Barber, J.; Loo, J. S. C. *Energ Environ Sci* **2012**, *5*, 5902.

(70) Ran, J. R.; Zhang, J.; Yu, J. G.; Jaroniec, M.; Qiao, S. Z. *Chem Soc Rev* **2014**, *43*, 7787.

(71) Berr, M. J.; Wagner, P.; Fischbach, S.; Vaneski, A.; Schneider, J.; Susha, A. S.; Rogach, A. L.; Jackel, F.; Feldmann, J. *Appl Phys Lett* **2012**, *100*, 223903.

(72) O'Connor, T.; Panov, M. S.; Mereshchenko, A.; Tarnovsky, A. N.; Lorek, R.; Perera, D.; Diederich, G.; Lambright, S.; Moroz, P.; Zamkov, M. *ACS Nano* **2012**, *6*, 8156.

(73) Tseng, H. W.; Wilker, M. B.; Damrauer, N. H.; Dukovic, G. *J Am Chem Soc* **2013**, *135*, 3383.

(74) Chen, X. B.; Shen, S. H.; Guo, L. J.; Mao, S. S. *Chem Rev* **2010**, *110*, 6503.

(75) Weinberg, D. R.; Gagliardi, C. J.; Hull, J. F.; Murphy, C. F.; Kent, C. A.; Westlake, B. C.; Paul, A.; Ess, D. H.; McCafferty, D. G.; Meyer, T. J. *Chem Rev* **2012**, *112*, 4016.

(76) Concepcion, J. J.; Jurss, J. W.; Brennaman, M. K.; Hoertz, P. G.; Patrocinio, A. O. T.; Iha, N. Y. M.; Templeton, J. L.; Meyer, T. J. *Accounts Chem Res* **2009**, *42*, 1954.

(77) Wada, T.; Tsuge, K.; Tanaka, K. *Angew Chem Int Edit* **2000**, *39*, 1479.

(78) Sens, C.; Romero, I.; Rodriguez, M.; Llobet, A.; Parella, T.; Benet-Buchholz, J. *J Am Chem Soc* **2004**, *126*, 7798.

(79) Zong, R.; Thummel, R. P. *J Am Chem Soc* **2005**, *127*, 12802.

(80) Tseng, H. W.; Zong, R.; Muckerman, J. T.; Thummel, R. *Inorg Chem* **2008**, *47*, 11763.

(81) Duan, L. L.; Fischer, A.; Xu, Y. H.; Sun, L. C. *J Am Chem Soc* **2009**, *131*, 10397.

(82) Wasylenko, D. J.; Ganesamoorthy, C.; Koivisto, B. D.; Henderson, M. A.; Berlinguette, C. P. *Inorg Chem* **2010**, *49*, 2202.

(83) Peng, P.; Sadtler, B.; Alivisatos, A. P.; Saykally, R. J. *J Phys Chem C* **2010**, *114*, 5879.

(84) Robinson, R. D.; Sadtler, B.; Demchenko, D. O.; Erdonmez, C. K.; Wang, L. W.; Alivisatos, A. P. *Science* **2007**, *317*, 355.

(85) Aldana, J.; Lavelle, N.; Wang, Y.; Peng, X. *J Am Chem Soc* **2005**, *127*, 2496.

(86) Sykora, M.; Petruska, M. A.; Alstrum-Acevedo, J.; Bezel, I.; Meyer, T. J.; Klimov, V. I. *J Am Chem Soc* **2006**, *128*, 9984.

(87) Koposov, A. Y.; Szymanski, P.; Cardolaccia, T.; Meyer, T. J.; Klimov, V. I.; Sykora, M. *Adv Funct Mater* **2011**, *21*, 3159.

(88) Kelly, C. A.; Farzad, F.; Thompson, D. W.; Meyer, G. J. *Langmuir* **1999**, *15*, 731.

(89) Nozik, A. J. *Annu Rev Phys Chem* **1978**, *29*, 189.

(90) Christopoulos, K.; Karidi, K.; Tsipis, A.; Garoufis, A. *Inorg Chem Commun* **2008**, *11*, 1341.

(91) *Semiconductors-Basic Data*; 2nd ed.; Madelung, O., Ed.; Springer: Berlin, 1996.

(92) Pavlishchuk, V. V.; Addison, A. W. *Inorg Chim Acta* **2000**, *298*, 97.

(93) Connelly, N. G.; Geiger, W. E. *Chem Rev* **1996**, *96*, 877.

(94) Jakubikova, E.; Chen, W. Z.; Dattelbaum, D. M.; Rein, F. N.; Rocha, R. C.; Martin, R. L.; Batista, E. R. *Inorg Chem* **2009**, *48*, 10720.

(95) Wu, K. F.; Zhu, H. M.; Liu, Z.; Rodriguez-Cordoba, W.; Lian, T. Q. *J Am Chem Soc* **2012**, *134*, 10337.

(96) Munro, A. M.; Jen-La Plante, I.; Ng, M. S.; Ginger, D. S. *J Phys Chem C* **2007**, *111*, 6220.

(97) Klimov, V. I.; Schwarz, C. J.; McBranch, D. W.; Leatherdale, C. A.; Bawendi, M. G. *Phys Rev B* **1999**, *60*, R2177.

(98) Knowles, K. E.; McArthur, E. A.; Weiss, E. A. *ACS Nano* **2011**, *5*, 2026.

(99) Huang, J. E.; Huang, Z. Q.; Jin, S. Y.; Lian, T. Q. *J Phys Chem C* **2008**, *112*, 19734.

(100) Huang, J.; Huang, Z. Q.; Yang, Y.; Zhu, H. M.; Lian, T. Q. *J Am Chem Soc* **2010**, *132*, 4858.

(101) Warren, J. J.; Mayer, J. M. *J Am Chem Soc* **2010**, *132*, 7784.

(102) Lakowicz, J. R. *Principles of Fluorescence Spectroscopy*; Springer: New York, 2006.

(103) Yin, Y.; Alivisatos, A. P. *Nature* **2005**, *437*, 664.

(104) Burda, C.; Chen, X. B.; Narayanan, R.; El-Sayed, M. A. *Chem Rev* **2005**, *105*, 1025.

(105) Bawendi, M. G.; Steigerwald, M. L.; Brus, L. E. *Annu Rev Phys Chem* **1990**, *41*, 477.

(106) Cozzoli, P. D.; Pellegrino, T.; Manna, L. *Chem Soc Rev* **2006**, *35*, 1195.

(107) Wang, F.; Wang, W. G.; Wang, H. Y.; Si, G.; Tung, C. H.; Wu, L. Z. *Acs Catal* **2012**, *2*, 407.

(108) Wen, F.; Li, C. *Acc Chem Res* **2013**, *46*, 2355.

(109) De Lacey, A. L.; Fernandez, V. M.; Rousset, M.; Cammack, R. *Chem Rev* **2007**, *107*, 4304.

(110) Tard, C.; Pickett, C. J. *Chem Rev* **2009**, *109*, 2245.

(111) English, C. M.; Eckert, C.; Brown, K.; Seibert, M.; King, P. W. *Dalton T* **2009**, 9970.

(112) Adams, M. W. W. *BBA - Bioenergetics* **1990**, *1020*, 115.

(113) Baffert, C.; Sybirna, K.; Ezanno, P.; Lautier, T.; Hajj, V.; Meynial-Salles, I.; Soucaille, P.; Bottin, H.; Leger, C. *Anal Chem* **2012**, *84*, 7999.

(114) Benemann, J. R.; Berenson, J. A.; Kaplan, N. O.; Kamen, M. D. *P Natl Acad Sci USA* **1973**, *70*, 2317.

(115) Peters, J. W.; Lanzilotta, W. N.; Lemon, B. J.; Seefeldt, L. C. *Science* **1998**, *282*, 1853.

(116) Hexter, S. V.; Grey, F.; Happe, T.; Climent, V.; Armstrong, F. A. *P Natl Acad Sci USA* **2012**, *109*, 11516.

(117) Capon, J. F.; Gloaguen, F.; Petillon, F. Y.; Schollhammer, P.; Talarmin, J. *Coordin Chem Rev* **2009**, *253*, 1476.

(118) Mulder, D. W.; Ratzloff, M. W.; Shepard, E. M.; Byer, A. S.; Noone, S. M.; Peters, J. W.; Broderick, J. B.; King, P. W. *J Am Chem Soc* **2013**, *135*, 6921.

(119) Barton, B. E.; Rauchfuss, T. B. *Inorg Chem* **2008**, *47*, 2261.

(120) King, P. W.; Posewitz, M. C.; Ghirardi, M. L.; Seibert, M. *J Bacteriol* **2006**, *188*, 2163.

(121) Mulder, D. W.; Boyd, E. S.; Sarma, R.; Lange, R. K.; Endrizzi, J. A.; Broderick, J. B.; Peters, J. W. *Nature* **2010**, *465*, 248.

(122) Mulder, D. W.; Ortillo, D. O.; Gardenghi, D. J.; Naumov, A. V.; Ruebush, S. S.; Szilagyi, R. K.; Huynh, B. H.; Broderick, J. B.; Peters, J. W. *Biochemistry* **2009**, *48*, 6240.

(123) Bradford, M. M. *Anal Biochem* **1976**, *72*, 248.

(124) Fish, W. W. *Method Enzymol* **1988**, *158*, 357.

(125) Duonghong, D.; Ramsden, J.; Gratzel, M. *J Am Chem Soc* **1982**, *104*, 2977.

(126) Dimitrijevic, N. M.; Savic, D.; Micic, O. I.; Nozik, A. J. *J Phys Chem-Us* **1984**, *88*, 4278.

(127) Zhu, H. M.; Song, N. H.; Lian, T. Q. *J Am Chem Soc* **2011**, *133*, 8762.

(128) van Driel, A. F.; Nikolaev, I. S.; Vergeer, P.; Lodahl, P.; Vanmaekelbergh, D.; Vos, W. L. *Phys Rev B* **2007**, *75*, 035329.

(129) Jones, M.; Scholes, G. D. *J Mater Chem* **2010**, *20*, 3533.

(130) Wu, K.; Rodríguez-Córdoba, W. E.; Yang, Y.; Lian, T. *Nano Lett* **2013**, *13*, 5255.

(131) Sadhu, S.; Patra, A. *J Phys Chem C* **2011**, *115*, 16867.

(132) Berberan-Santos, M. N.; Bodunov, E. N.; Valeur, B. *Chem Phys* **2005**, *315*, 171.

(133) Adams, M. W.; Mortenson, L. E. *J Biol Chem* **1984**, *259*, 7045.

(134) Thauer, R. K.; Kaufer, B.; Zahringe.M; Jungerma.K *Eur J Biochem* **1974**, *42*, 447.

(135) Goldet, G.; Brandmayr, C.; Stripp, S. T.; Happe, T.; Cavazza, C.; Fontecilla-Camps, J. C.; Armstrong, F. A. *J Am Chem Soc* **2009**, *131*, 14979.

(136) Bennett, B.; Lemon, B. J.; Peters, J. W. *Biochemistry* **2000**, *39*, 7455.

(137) Lemon, B. J.; Peters, J. W. *Biochemistry* **1999**, *38*, 12969.

(138) Pershad, H. R.; Duff, J. L. C.; Heering, H. A.; Duin, E. C.; Albracht, S. P. J.; Armstrong, F. A. *Biochemistry* **1999**, *38*, 8992.

(139) Dibbell, R. S.; Watson, D. F. *J Phys Chem C* **2009**, *113*, 3139.

(140) Tagliazucchi, M.; Tice, D. B.; Sweeney, C. M.; Morris-Cohen, A. J.; Weiss, E. A. *ACS Nano* **2011**, *5*, 9907.

(141) Lo, S. S.; Mirkovic, T.; Chuang, C. H.; Burda, C.; Scholes, G. D. *Adv Mater* **2011**, *23*, 180.

(142) Zhu, H. M.; Lian, T. Q. *Energ Environ Sci* **2012**, *5*, 9406.

(143) Pandey, A. S.; Harris, T. V.; Giles, L. J.; Peters, J. W.; Szilagyi, R. K. *J Am Chem Soc* **2008**, *130*, 4533.

(144) Adams, M. W. W. *J Biol Chem* **1987**, *262*, 15054.

(145) Parkin, A.; Cavazza, C.; Fontecilla-Camps, J. C.; Armstrong, F. A. *J Am Chem Soc* **2006**, *128*, 16808.

(146) Cornish, A. J.; Gärtner, K.; Yang, H.; Peters, J. W.; Hegg, E. L. *J Biol Chem* **2011**, *286*, 38341.

(147) Bertrand, P.; Dole, F.; Asso, M.; Guigliarelli, B. *J Biol Inorg Chem* **2000**, *5*, 682.

(148) Abou Hamdan, A.; Dementin, S.; Liebgott, P. P.; Gutierrez-Sanz, O.; Richaud, P.; De Lacey, A. L.; Rousset, M.; Bertrand, P.; Cournac, L.; Leger, C. *J Am Chem Soc* **2012**, *134*, 9828.

(149) Cheah, M. H.; Tard, C.; Borg, S. J.; Liu, X.; Ibrahim, S. K.; Pickett, C. J.; Best, S. P. *J Am Chem Soc* **2007**, *129*, 11085.

(150) Chaudhary, Y. S.; Woolerton, T. W.; Allen, C. S.; Warner, J. H.; Pierce, E.; Ragsdale, S. W.; Armstrong, F. A. *Chem Commun* **2012**, *48*, 58.

(151) Santangelo, J. D.; Dürre, P.; Woods, D. R. *Microbiology* **1995**, *141*, 171.

(152) Moser, C. C.; Keske, J. M.; Warncke, K.; Farid, R. S.; Dutton, P. L. *Nature* **1992**, *355*, 796.

(153) Gray, H. B.; Winkler, J. R. *P Natl Acad Sci USA* **2005**, *102*, 3534.

(154) Page, C. C.; Moser, C. C.; Chen, X. X.; Dutton, P. L. *Nature* **1999**, *402*, 47.

(155) Moser, C. C.; Page, C. C.; Dutton, P. L. *Photoch Photobio Sci* **2005**, *4*, 933.

(156) King, P. W. *Bba-Bioenergetics* **2013**, *1827*, 949.

(157) Watson, D. F. *J Phys Chem Lett* **2010**, *1*, 2299.

(158) Anderson, N. A.; Lian, T. Q. *Annu Rev Phys Chem* **2005**, *56*, 491.

(159) Wang, H.; McNellis, E. R.; Kinge, S.; Bonn, M.; Canovas, E. *Nano Lett* **2013**, *13*, 5311.

(160) Hyun, B. R.; Bartnik, A. C.; Sun, L. F.; Hanrath, T.; Wise, F. W. *Nano Lett* **2011**, *11*, 2126.

(161) Carbone, L.; Nobile, C.; De Giorgi, M.; Sala, F. D.; Morello, G.; Pompa, P.; Hytch, M.; Snoeck, E.; Fiore, A.; Franchini, I. R.; Nadasan, M.; Silvestre, A. F.; Chiodo, L.; Kudera, S.; Cingolani, R.; Krahne, R.; Manna, L. *Nano Lett* **2007**, *7*, 2942.

(162) Brown, P. R.; Kim, D.; Lunt, R. R.; Zhao, N.; Bawendi, M. G.; Grossman, J. C.; Bulovic, V. *ACS Nano* **2014**, *8*, 5863.

(163) Frederick, M. T.; Amin, V. A.; Swenson, N. K.; Ho, A. Y.; Weiss, E. A. *Nano Lett* **2013**, *13*, 287.

(164) Saunders, A. E.; Ghezelbash, A.; Sood, P.; Korgel, B. A. *Langmuir* **2008**, *24*, 9043.

(165) Kambhampati, P. *Chem Phys* **2015**, *446*, 92.

(166) Wu, K.; Rodríguez-Córdoba, W.; Lian, T. *J Phys Chem B* **2014**, *118*, 14062.

(167) Cui, X. D.; Zarate, X.; Tomfohr, J.; Sankey, O. F.; Primak, A.; Moore, A. L.; Moore, T. A.; Gust, D.; Harris, G.; Lindsay, S. M. *Nanotechnology* **2002**, *13*, 5.

(168) Bumm, L. A.; Arnold, J. J.; Dunbar, T. D.; Allara, D. L.; Weiss, P. S. *J Phys Chem B* **1999**, *103*, 8122.

(169) Holmlin, R. E.; Haag, R.; Chabinyc, M. L.; Ismagilov, R. F.; Cohen, A. E.; Terfort, A.; Rampi, M. A.; Whitesides, G. M. *J Am Chem Soc* **2001**, *123*, 5075.

(170) Weber, K.; Hockett, L.; Creager, S. *J Phys Chem B* **1997**, *101*, 8286.

(171) Wold, D. J.; Haag, R.; Rampi, M. A.; Frisbie, C. D. *J Phys Chem B* **2002**, *106*, 2813.

(172) Adams, D. M.; Brus, L.; Chidsey, C. E. D.; Creager, S.; Creutz, C.; Kagan, C. R.; Kamat, P. V.; Lieberman, M.; Lindsay, S.; Marcus, R. A.; Metzger, R. M.; Michel-Beyerle, M. E.; Miller, J. R.; Newton, M. D.; Rolison, D. R.; Sankey, O.; Schanze, K. S.; Yardley, J.; Zhu, X. Y. *J Phys Chem B* **2003**, *107*, 6668.

(173) Vincent, K. A.; Belsey, N. A.; Lubitz, W.; Armstrong, F. A. *J Am Chem Soc* **2006**, *128*, 7448.

(174) Jones, M.; Lo, S. S.; Scholes, G. D. *J Phys Chem C* **2009**, *113*, 18632.

(175) Infelta, P. P.; Gratzel, M.; Thomas, J. K. *J Phys Chem* **1974**, *78*, 190.

(176) Tachiya, M. *Chem Phys Lett* **1975**, *33*, 289.

(177) Beane, G. A.; Morfa, A. J.; Funston, A. M.; Mulvaney, P. *J Phys Chem C* **2012**, *116*, 3305.

(178) Sadhu, S.; Patra, A. *Chemphyschem* **2013**, *14*, 2641.

(179) Morris-Cohen, A. J.; Frederick, M. T.; Cass, L. C.; Weiss, E. A. *J Am Chem Soc* **2011**, *133*, 10146.